QUANTITATIVE ELASTICITY IMAGING AND SOFT TISSUE CHARACTERIZATION USING TAGGED MAGNETIC RESONANCE IMAGING

FU YABO
(B.Eng. Beijing Institute of Technology, China)

A THESIS SUBMITTED
FOR THE DEGREE OF DOCTOR OF PHILOSOPHY
DEPARTMENT OF MECHANICAL ENGINEERING
NATIONAL UNIVERSITY OF SINGAPORE
2012

DECLARATION

I hereby declare that the thesis is my original work and it has been written by me in its entirety.

I have duly acknowledged all the sources of information which have been used in the thesis.

This thesis has also not been submitted for any degree in any university previously.

Fu Yabo
23 July, 2012

ACKNOWLEDGEMENT

I would like to show my deepest gratitude to my supervisors, Dr. Chui Chee Kong and Prof. Teo Chee Leong, for their great guidance and dedicated support, which helped me immensely in the completion of this research work. Dr. Chui Chee Kong is not only a great mentor in my academic research study but also a friend who helped me overcome many difficulties in my life in Singapore. Thanks very much!

I am grateful to Prof. Kobayashi Etsuko for her generous support during my attachment to the University of Tokyo (UT). I wish to thank Dr. Chang K.Y. Stephen from the Department of Surgery, National University Hospital (NUH) for his constructive suggestions. I appreciate very much the kind help from Mr. Christopher Au C.C. (Radiology, NUH) with our MRE experiments at NUH. Without their guidance and mentorship, I would not have managed to accomplish such interdisciplinary work.

I enjoyed the cooperation with my group members, including Dr. Li Bingnan, Mr. Takei Yoshiyuki and Mr. Shen Zhonghuan. They provided many good ideas and advices which had inspired me during my research study. We have built great friendship through exchanging ideas and performing MRE experiments together. It is a pleasure to thank Mr. Yang Liangjing, Mr. Yang Tao and many other colleagues for their kind help and encouraging words.

It is my honor to study under the Department of Mechanical Engineering, National University of Singapore (NUS). I appreciate the financial support and scholarship from NUS to carry out this research.

Last but not least, I would like to thank my parents and sister for their support and encouragement. Without their support and consideration, I would not have been able to fully devote myself to this doctoral programme.

FU YABO

06 June 2012

TABLE OF CONTENTS

SUMMARY

Elasticity is an important property for soft tissue characterization. Local changes in mechanical properties of soft tissues may indicate the presence of tumors and other diseases. Palpation is traditionally used by physicians to detect the presence of tumors. However, palpation greatly depends on the experiences of physician, and is a subjective method for determining the tissue properties. Moreover, many parts of human body such as the brain and deep abdominal organs cannot be assessed simply by human hands. In order to quantitatively study the soft tissue mechanical properties, various elasticity imaging methods, including ultrasonic elastography (UE) and magnetic resonance elastography (MRE), have been proposed in the last two decades. MRE is a promising non-invasive method to quantitatively determine the properties of biological tissue. MRE can be divided into two categories: dynamic MRE and quasi-static MRE, according to its external mechanical actuation method. Biological tissue is perturbed at high frequencies of 60-1000Hz in dynamic MRE while biological tissue is deformed at much lower frequencies of 0-1HZ in quasi-static MRE.

Currently, quasi-static MRE has no established standards for actuation system. A *new image acquisition system* which uses a MR compatible actuator to produce an indentation sequence according to simulated electrocardiography (ECG) signal was developed for quasi-static MRE. This actuation system extends the application of tagged MR image sequence from heart to normal soft tissues. Experiments were conducted on both agar gel phantoms and human soft tissue. Conventional harmonic phase (HARP) image processing technique is also extended for *large motion tracking* during indentation. From tagged MR images, internal displacement field and strain of the imaged soft tissues are computed for quantitative elasticity reconstruction. In

order to accurately calculate the internal displacement field and strain, a novel image processing technique called *adaptive windowed harmonic phase (AWHARP)* was proposed for tagged MR images.

Nonlinear optimization method and finite element (FE) method were investigated for solving inverse elasticity problem. A *novel elasticity reconstruction method* was proposed for hyperelastic material models. This method combines the advantages of FE-based direct inverse method and nonlinear optimization algorithm. An estimation of the true material stiffness distribution was first determined using FE-based direct inverse method. This estimation was then input to Levenberg-Marquardt (LM) optimization algorithm as the initial guess. Final solution was obtained after the optimization process. Experimental results showed that soft tissue properties can be determined efficiently and accurately using this elasticity reconstruction method.

Soft tissue indentation is affected by both compressive and tensile characteristics of the soft tissue. A new material characterization method using inverse FE method was proposed for accurate soft tissue indentation simulation. Instead of determining the material parameters from uniaxial stress-strain data of compressions or elongations, the stress-strain data from a cycle of compression and then elongation of porcine liver samples was used. The *material parameters determined using combined compressive and tensile stress-strain data* can simulate soft tissue indentation with good accuracies. However, the liver tissue is highly heterogeneous with diverting stress-strain curves. We proposed *a probabilistic approach* to model the diverting stress-strain curves of liver tissue samples.

The work presented in this thesis advances the research of quantitative elasticity imaging and soft tissue characterization. Potential of quasi-static MRE as a clinical diagnostic tool has been demonstrated.

LIST OF TABLES

LIST OF FIGURES

LIST OF SYMBOLS

$\sqrt{\ }$	Square root
$\| \|$	Vector norm
∇	Gradient
$\int$	Integration
π	Mathematical constant pi
$\sum$	Summation
$div(\cdot)$	Divergence
$\exp(\cdot)$	Exponential function
$\max(\cdot)$	Maximum
$\min(\cdot)$	Minimum
$\delta(\cdot)$	Dirac function
$wrap(\cdot)$	Phase wrapping function
$\mathrm{mod}(\cdot)$	Modulus (signed remainder after division)
$In(\cdot)$	Natural logarithm

LIST OF ABBREVIATIONS:

AWFT	adaptive windowed Fourier transform
AWHARP	adaptive windowed harmonic phase
CAD	computer aided design
CDF	cumulative distribution function
CNR	contrast to noise ratio
CSPAMM	complementary spatial modulation of magnetization
CT	computed tomography
DOF	degree of freedom
DVT	deep venous thrombosis
ECG	electrocardiography
FE	finite element
FOV	field of view
GWT	Gabor wavelet transforms
HARP	harmonic phase
HCM	hypertrophic cardiomyopathy
IMVFOSM	inverse mean-value first-order second-moment
LM	Levenberg-Marquardt
LV	left ventricle
MC	Monte Carlo
MR	magnetic resonance
MRE	magnetic resonance elastography
MRI	magnetic resonance imaging
MSG	motion sensitive gradient
NMR	nuclear magnetic resonance

PDF	probability density function
RF	radiofrequency
RMSE	root mean square error
SNR	signal to noise ratio
SPAMM	spatial modulation of magnetization
TBI	traumatic brain injuries
TE	echo time
TR	repetition time
UE	ultrasonic elastography
US	ultrasonography

CHAPTER 1 INTRODUCTION

1.1 Background and Motivations

Characterization of biological tissue properties is important. Local changes in mechanical properties of biological tissue may indicate the presence of tumors and other diseases (Srinivasan et al., 2004). Pathologies often induce histological changes (such as inflammation, edema, fibrosis, increase in oncotic pressure, variation of extracellular space, etc.) and then cause bio-mechanical properties of soft tissue to change locally. In the case of deep venous thrombosis (DVT), stiffness of the thrombus is closely related to thrombus maturity, which in turn determines the appropriate course of treatment (Xie et al., 2005). In the case of liver fibrosis, the mechanical properties of liver tissue are strongly correlated with the extent of fibrosis (Yin et al., 2007; Castera et al., 2005; Ziol et al., 2005). Knowledge of brain material properties also helps to understand the mechanism of concussion and other types of traumatic brain injuries (TBI) (Atay et al., 2008). However, common imaging modalities such as ultrasonography (US), X-ray computed tomography (CT) and magnetic resonance imaging (MRI) only provide spatial discrimination of soft tissue. Mechanical properties of soft tissue remain unknown for clinicians.

For centuries, clinicians have been using manual palpation to detect pathological tissue changes. However, palpation greatly depends on the experiences of clinicians and is a subjective method to justify soft tissue properties. Limited by hand accessibility and tangible sensitivity, manual palpation is usually only used to detect hepatic cirrhosis and breast tumors. In order to quantitatively study the soft tissue

mechanical properties, various elasticity imaging methods, including ultrasonic elastography (UE) and magnetic resonance elastography (MRE), have been proposed in the last two decades.

A typical elasticity imaging system composes of three components: an actuator to perturb soft tissue in a specific manner, modalities for deformation or wave imaging, and inverse algorithms for elasticity reconstruction. Though both US and MRI can be used for motion imaging, MRI is used throughout our study since MRI has advantage in overall resolution and accuracy of motion and strain measurement. MRE can be divided into two categories: dynamic MRE and quasi-static MRE according to its external mechanical actuation method. In dynamic MRE, biological tissue is perturbed at high frequencies of 60-1000Hz for wave imaging. Elastography is determined from the wavelength of the propagating wave inside the imaged objects. In quasi-static MRE, biological tissue is deformed at much lower frequencies of 0-1HZ for deformation imaging. Given known boundary conditions, elastography is determined from the measured displacement/strain images of the deformed soft tissue.

MRE has been used to discriminate pathological or ablated tissues from normal ones of liver (Venkatesh et al., 2008; Vizzutti et al., 2009) and breast (Manduca et al., 2001, Sinkus *et al.*, 2005). Knowledge of brain tissue mechanical properties determined using MRE has been used to help understand the natural development of brain growth (Sack et al., 2009). Another application of MRE is intraoperative image-guided surgery. The quality of diagnostic imaging, such as MRI and CT, has improved significantly over the last several decades. Detailed 3D images of anatomy, which reveal the location, shape and size of pathology, are available to surgeons prior to

operation. In image-guided surgery, these 3D images are registered to the patient during the operation in order to provide spatial navigation and guidance. This is usually achieved using a rigid body transformation (Carter et al., 2005). However, soft tissue will deform when interacting with surgical tools during surgery. Hence, the registered preoperative images using the rigid body transformation will no longer match with the actual surgical presentation. The accuracy of the spatial guidance is degraded. This severely limits the current application of image-guided surgery technology to many soft tissue organs. A potential solution to the misalignment between the preoperative images and surgical presentation is to use a computational model which can simulate deformations, and thus can warp the preoperative images to reflect the surgical scene. Elastography of soft tissue should facilitate the establishment of an accurate model to reflect the actual surgical scene during tool-tissue interaction.

1.2 Quantitative Elasticity Imaging

Quantitative elasticity imaging usually refers to an imaging method which aims at soft tissue discrimination by accessing its mechanical properties. Quantitative elasticity imaging is also referred to as soft tissue elastography. At first, elastography did not directly display elasticity information, but rather tissue strain. One pioneering work was published by Ophir and co-workers who used ultrasound tracking of quasi-static breast compression to generate strain images (Ophir et al., 1991). The resulting strain images could improve the accuracy of diagnosis over ultrasound alone (Zhi et al., 2007). One step beyond strain imaging is elasticity imaging which involves solving an inverse problem with the measured strain to determine the elasticity distribution of

soft tissue. The very first works of elasticity imaging were by Sumi et al. (1995), Skovoroda et al. (1995), Kallel and Bertrand, (1996), Sumi et al. (1998), Skovoroda et al. (1999). More recent publications can be found in Barbone and Gokhale (2004), Sumi and Matsuzawa (2007), Barbone and Oberai (2007), Guo et al. (2008), Richards et al. (2009).

While the concept of elastography was first proposed in ultrasound literature, a large number of works on elastography has been published in MRI literature. MRI is increasingly used for elastography due to its overall better performance than ultrasound. Elasticity imaging using MRI is conventionally called Magnetic Resonance Elastography (MRE). MRE can be divided into two categories: dynamic MRE and quasi-static MRE according to its external mechanical actuation method. Dynamic MRE determines soft tissue elastography from propagating waves inside the soft tissue while quasi-static MRE utilizes displacement/strain image to determine the soft tissue elastography. Dynamic MRE has currently been clinically used for assessment of hepatic fibrosis. Contrarily, quasi-static MRE is still in its developing stage. Generally speaking, MRE remains an active research topic since there is still plenty of room for improvement of both dynamic and quasi-static MRE.

1.3 Dissertation Objectives and Organization

MRE has gone through over twenty years of research and development. Chapter 2 describes the current status of MRE by reviewing the literature of quantitative elasticity imaging, including dynamic MRE, quasi-static MRE. Different actuation devices and imaging sequences were introduced. In the second part of Chapter 2,

various tagged MR image processing techniques, including feature tracking based approaches and Fourier domain based approaches, were studied and discussed. Chapter 2 also introduces several popular inverse elasticity algorithms for soft tissue reconstruction.

The following questions may be raised in quantitative elasticity imaging. These questions are addressed in this thesis.

1. How to effectively and efficiently acquire images for elasticity measurement?

For MRE, many papers have been published on dynamic MRE while only a few publications are available for quasi-static MRE. It is important to develop a new image acquisition system for quasi-static MRE. Dynamic MRE has been utilizing pneumatic actuator with phase contrast MR image sequences for wave imaging. On the other hand, quasi-static MRE requires a MR compatible motor of high torque to deform soft tissue in MR scanner and a MR compatible force sensor to record perturbation force during tool-tissue interaction. Most MR imaging sequences that are widely used for MRE require extensive programming of imaging sequence which is challenging and enhances the difficulty of MRE research. In this thesis, we developed an image acquisition system using tagged MRI, an imaging sequence widely equipped in almost every clinical MRI scanner. The new acquisition system should facilitate the development of quasi-static MRE research.

Chapter 3 details the development of our new image acquisition system. We first introduced the principle of tagged MR imaging sequence. The design of an MR

compatible actuator and force sensor was described subsequently. MR compatibility of the actuator and force sensor was tested and signal to noise ratios (SNR) of the MR images were reported. The actuator was synchronized with tagged MR imaging sequence using simulated ECG signal and motor controlling software.

2. How to process tagged MR images for fast and accurate motion tracking and strain calculation?

Tagged MR images are not directly interpretable, sophisticated image processing methods are needed to produce meaningful displacement field and strain images. Since tagged MR image sequence is originally designed for cardiac imaging, various tagged MR image processing techniques have been proposed for myocardial function evaluation. However, accuracy and computational efficiency of the processing algorithms remain an active research topic. In Chapter 4, we developed an accurate and fast method, adaptive windowed harmonic phase (AWHARP), for strain calculation from tagged MR images. Improved strain calculation should contribute to a better reconstruction of soft tissue elasticity. Tagged MR images of hearts with hypertrophic cardiomyopathy were processed and compared with that of normal hearts. We demonstrated that AWHARP can help clinicians to detect left ventricle (LV) dysfunctions and myocardial diseases by producing accurate strain images.

3. How to effectively reconstruct elastography from strain images?

Inverse elasticity algorithms are required to determine elastography from the displacement field and strain images. To date, there is a lack of effective algorithms to

solve inverse elasticity problems. In Chapter 5, nonlinear optimization method and finite element (FE) method were investigated for solving inverse elasticity problem. A novel elasticity reconstruction method was proposed for hyperelastic material models. This method combines the advantages of FE-based direct inverse method and nonlinear optimization method. An estimation of the true material stiffness distribution was first determined using the FE-based direct inverse method. This estimation was then input to the Levenberg-Marquardt (LM) optimization algorithm as the initial guess. Final solution was obtained after the optimization process. We showed that soft tissue properties can be determined efficiently and accurately using this material stiffness reconstruction method.

4. How to accurately model and simulate soft tissue deformation?

Forward elasticity problem needs to be performed in order to solve the inverse elasticity problem. Finite element models are required to realistically simulate the deformation of soft tissue under indentation. Soft tissue indentation is affected by both compressive and tensile characteristics of the soft tissue. In Chapter 6, a new material characterization method using inverse FE method was proposed for soft tissue indentation simulation. Instead of determining the material parameters from uniaxial stress-strain data of compressions or elongations, the stress-strain data from a cycle of compression and then elongation of porcine liver samples was used. The material parameters determined using combined compressive and tensile stress-strain data can simulate soft tissue indentation with good accuracies. However, the liver tissue is highly heterogeneous with diverting stress-strain curves. To represent the diverting

stress-strain relationship of liver tissue samples, we proposed a nondeterministic approach to determine the liver tissue property in Chapter 7.

CHAPTER 2 RELATED WORKS

After over twenty years of research and development, a large number of works has been published on MRE. To determine the current state of development, we reviewed the literatures of MRE by studying its components, including image acquisition system, image processing techniques and inverse elasticity algorithms. Different kinds of actuation devices and imaging sequences were first introduced. Various tagged MR image processing techniques, including feature tracking based approaches and Fourier domain based approaches, were then studied and discussed. Finally, we introduced several popular inverse elasticity algorithms for soft tissue elasticity reconstruction.

2.1 MRE Image Acquisition

2.1.1 Actuation Devices

High-quality MR imaging requires a very stable homogeneous main magnetic field and linear gradient fields. Magnetic susceptible material, typically known as ferromagnetic metal, can cause serious distortion on images. Normal electric motors cannot be driven close to MR scanner due to their strong magnetic interference. It is a tricky task to generate required actuation without affecting the image quality. Due to these limitations, different non-magnetic actuation systems have been developed, including ultrasonic motors (Chinzei and Miller, 2001; Fu et al., 2011), hydraulic actuators (Gassert et al., 2006), pneumatic actuators (Yin et al., 2007, Takei et al., 2010), electromagnetic actuators (Manduca et al., 2001; Hamhaber et al., 2003), electrostrictive polymer actuators (Vogan et al., 2004) and electrostatic film motors

(Rajendra et al., 2008). In this section, we introduced three different most often used actuation devices.

2.1.1.1 Pneumatic Actuator

Pneumatic actuator was used to vibrate liver organ by Yin et al. (2007). A speaker was synchronized with imaging gradient for phase contrast wave imaging. Through a plastic tube, the speaker applied excitation of certain frequency on liver organ percutaneously. The pneumatic actuator is illustrated in Figure 2-1.

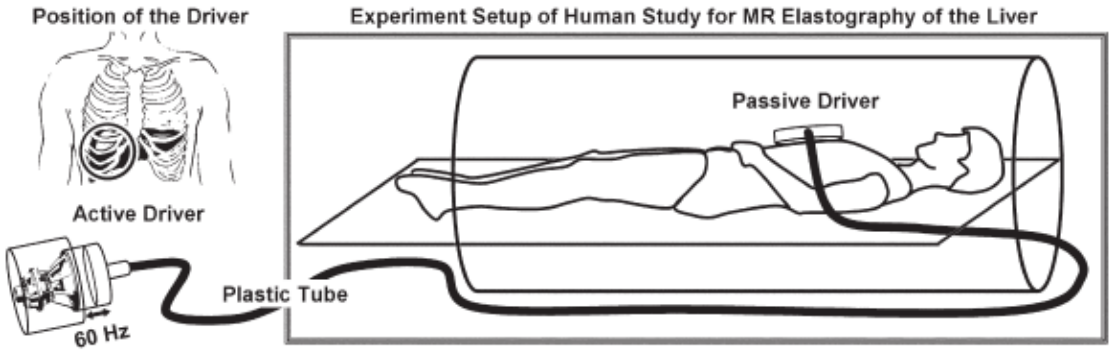

Figure 2-1. Pneumatic actuator (Adapted from Yin et al., 2007)

2.1.1.2 Electromagnetic Actuator

An alternative method is to utilize main magnetic field and coil to introduce vibration to soft tissue. Typically, this kind of device uses an "excitation" coil fixed to a beam with the opposite end attached to the patient surface or phantom surface over an "actuator surface". With the application of an alternating current to this coil, the resulting interaction with the static magnet field will create an alternating torque on the coil parallel to B_0. The induced vibrations of the induction coil are carried forward via beam and transducer plate to the phantom surface. The type of connection

between the actuator and the object determines the shape of the induced shear waves (Manduca et al., 2001). As shown in Figure 2-2, a conventional MR imaging sequence is used with an additional motion-sensitizing gradient imposed along a specific direction, switched in polarity at some adjustable frequency. Trigger pulses synchronize an oscillator amplifier unit that drives an electromechanical actuator coupled to the surface of the object to be imaged, inducing shear waves in the object at the same frequency as the motion-sensitizing gradient.

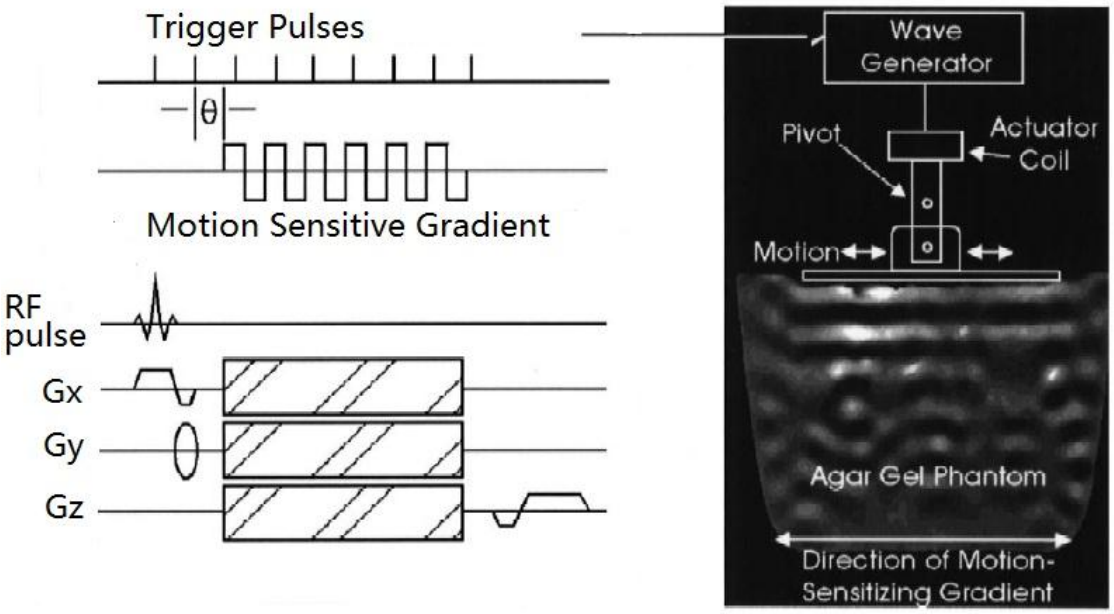

Figure 2-2. Configuration of electromechanical driver. θ is the phase offset between motion sensitive gradient and trigger pulses, Gx, Gy and Gz are imaging gradients in the x, y and z direction respectively (Manduca et al., 2001)

2.1.1.3 Electrostatic Film Actuator

Rajendra et al. (Rajendra et al., 2008) used a high-power electrostatic linear motor called dual excitation multiphase electrostatic drive. This motor was composed of a pair of thin plastic films which were manufactured using flexible printed circuit technology. The motor was driven by a high three-phase AC voltage. The maximum force of the motor depends on the amplitude of the applied voltage. In order to obtain

a practically large force, amplitude of higher than $1kV_{0\text{-}P}$ is necessary. The actuation system is illustrated in Figure 2-3.

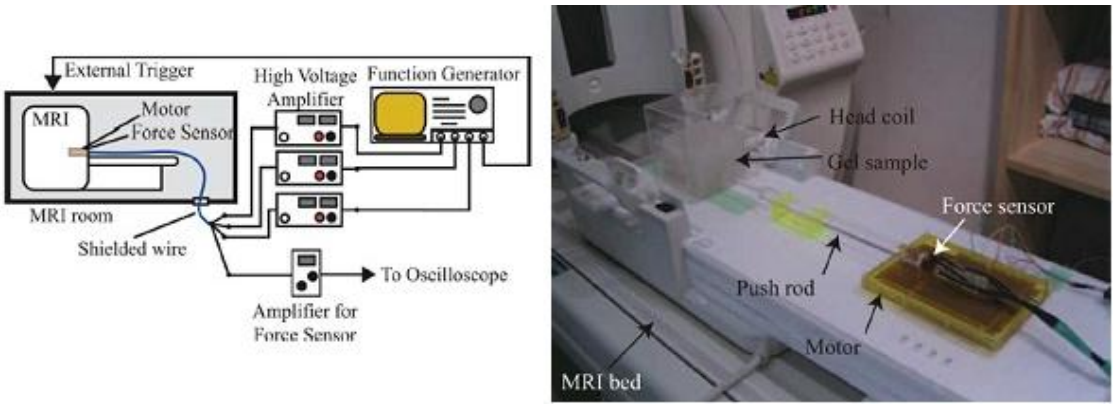

Figure 2-3. Electrostatic film actuator (Adapted from Rajendra et al., 2008)

2.1.2 Imaging Sequences

A MRI pulse sequence is a series of events comprising RF pulses, gradient waveforms, and data acquisition. The purpose of the sequence is to manipulate the magnetization in order to produce the desired signal. Pulse sequences play a central role in MR imaging. Many important concepts of MR are realized through pulse sequence design and implementation. Phase contrast method is commonly used in MRE to capture deformation of the imaged soft tissue. The phase accumulation theory can be explained as follows. For dynamic MRE, oscillating shear displacements caused by vibration are measured from phase images obtained by modulating the gradient field of the MR scanner at the vibration frequency (Muthupillai et al., 1995). Let us consider a magnetic field gradient with constant amplitude and frequency:

$$\vec{G}(t) = \vec{G}_0 \cos(wt) \tag{2.1}$$

where $\vec{G}(t)$ is temporal functions of the magnetic gradient superimposed on the static magnetic field and t is time. w is the angular frequency, $\vec{G}_0$ represents the amplitude of the magnetic field gradient. If this oscillating gradient is applied in three orthogonal

directions for a constant duration τ, a vector of motion-induced phase ϕ in an nuclear magnetic resonance (NMR) signal is given by (Suga et al., 2007)

$$\phi = \gamma \int_0^{\tau} \vec{G}(t) \cdot \vec{r}(t) dt \tag{2.2}$$

where γ is the gyro-magnetic ratio, τ is the time duration of the gradient after excitation, $\vec{r}(t)$ is the nuclear spin position. If $\vec{r}(t)$ represents complex motion, then

$$\vec{r}(t) = \vec{r}_0 + \vec{\xi}(r,t) \tag{2.3}$$

where $\vec{r}_0$ is the position of the nuclear spin at time t=0, and $\vec{\xi}(r,t)$ is the displacement of the spin about its mean position $\vec{r}_0$. The magnetic gradient $\vec{G}(t)$ may be viewed as a basis function for estimating the harmonic components of the nuclear spin position $\vec{r}(t)$.

If $\vec{r}(t)$ represents simple harmonic motion, then

$$\vec{\xi}(r,t,\theta) = \vec{\xi}_0 \cos(k \cdot r - wt + \theta) \tag{2.4}$$

where $\vec{\xi}_0$ is the displacement amplitude of the spin from the mean position, k is the wave vector, θ is an initial phase offset between the external vibration and the gradient $\vec{G}(t)$. If the gradient is switched in polarity at the same frequency as the spin motion, and time duration τ is chosen so that

$$\int_0^{\tau} \vec{G}(t) dt = 0 \tag{2.5}$$

then the observed phase shift in the NMR signal is given by

$$\phi = \gamma \int_0^{\tau=NT} \vec{G}(T) \cdot \vec{\xi}_0 \cos(k \cdot r - wt + \theta) dt = \frac{2\gamma NT(\vec{G} \cdot \vec{\xi})}{\pi} \sin(k \cdot r + \theta) \tag{2.6}$$

where N is the number of gradient cycles and T is the period of the mechanical excitation. Equation 2.6 indicates that the observed phase shift is the NMR signal

obtained under these conditions and is proportional to the scalar product of the displacement amplitude vector and the gradient vector (Muthupillai et al., 1995; Othman et al., 2005).

Three different MR pulse sequences are usually used to perform MRE imaging. For each one of these pulse sequences, two acquisitions were recorded by toggling the motion sensitizing gradients, and complex division was performed to obtain the phase-difference map (Othman et al., 2007). Below are the details of these imaging sequences.

2.1.2.1 Spin-echo Phase-contrast Pulse Sequence

A standard spin-echo pulse sequence was modified by introducing the motion-sensitizing gradient in addition to the slice-selection, phase-encoding and readout gradients. Three schemes were used to apply the motion-sensitizing gradient to any single axis in which one motion sensitizing gradient waveform was added after the 90° excitation pulse but before the 180° refocusing pulse. A generic spin-echo phase-contrast sequence is shown in Figure 2-4.

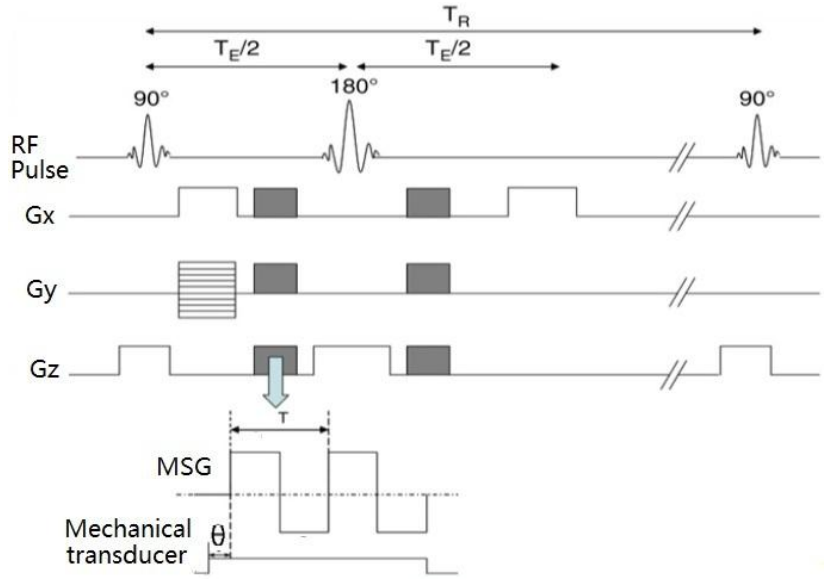

Figure 2-4. Spin-echo phase-contrast pulse sequence. θ is the phase offset between MSG and mechanical transducer, Gx, Gy and Gz are imaging gradients in the x, y and z direction respectively (Othman et al., 2007)

2.1.2.2 Gradient-echo Phase-contrast Pulse Sequence

A standard gradient-echo sequence was modified by introducing the bipolar gradient pulses (motion-sensitizing gradient) in addition to the slice-selection, phase-encoding and readout gradients. The motion-sensitizing gradient was synchronized with the oscillatory motion of the mechanical actuator. A variable phase offset θ between the motion sensitizing gradient and the mechanical actuator was used to study shear-wave temporal movement by changing the timing between the motion-sensitizing gradient and the mechanical actuator. A general gradient-echo phase-contrast sequence is shown in Figure 2-5.

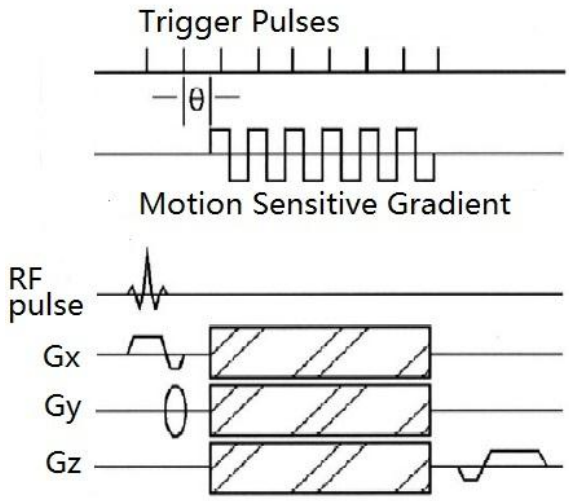

Figure 2-5. Gradient-echo phase-contrast pulse sequence. θ is the phase offset between motion sensitive gradient and trigger pulses, Gx, Gy and Gz are imaging gradients in the x, y and z direction respectively (Manduca et al., 2001)

2.1.2.3 Displacement Encoded Spin Echo Pulse Sequence

Chenevert et al. (1998) proposed to use a stimulated echo sequence with displacement-encoding gradient pulses to image quasi-static deformation. Mechanical transition from state "A" to state "B" occurs during the stimulated echo mixing time, TM. A relatively long mixing time allows long-lived elastic vibrations to dampen before spatial encoding. Since the relevant magnetization during TM is longitudinal, it is unaffected by potentially ill-defined motions during the mechanical transition period. As a result, a more accurate static deformation measurement is achieved. Precise synchronization of mechanical and pulsed gradient events is not critical as long as the mechanical transition begins after the second RF pulse and completes before the third RF pulse. Local displacement is encoded by means of phase shift governed by pulsed-field gradient factors. The imaging sequence is shown in Figure 2-6.

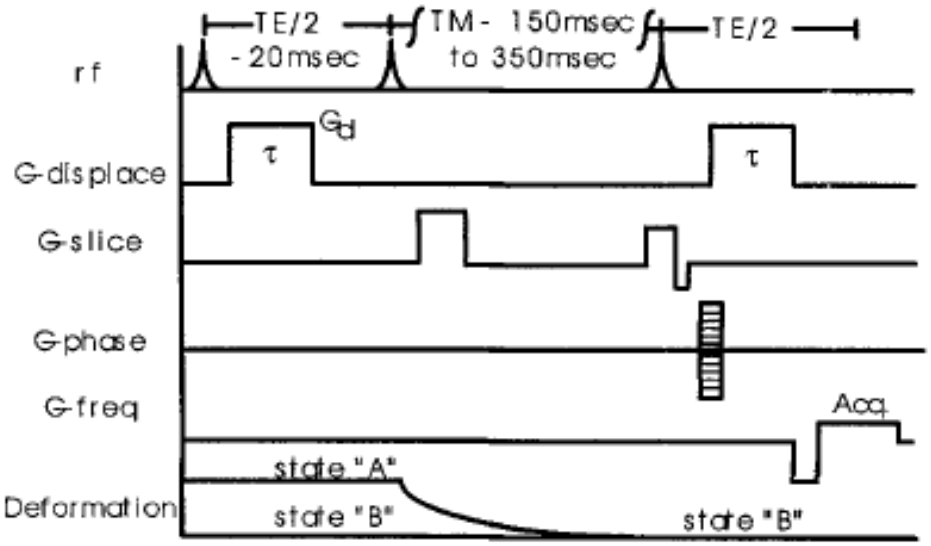

Figure 2-6. Displacement Encoded Spin Echo Pulse Sequence Deformation occurs during the mixing time (TM) such that static displacement equilibrium is achieved. Local displacement between deformation states 'A' and 'B' is encoded by phase shift proportional to 'G-displacement' G_d and its duration τ (Adapted from Chenevert et al., 1998)

2.2 Tagged MR Image Processing

Since the introductory of tagged MR imaging over a decade ago (Zerhouni et al., 1988; Axel et al., 1989), many works have been published for in vivo assessment of heart performance. Tagged MRI has been extensively used to measure myocardial strain in many recent medical research and scientific investigations (Moore et al., 1992; Denney et al., 1997; McVeigh et al., 1998). The use of tagged MRI has helped researchers to develop normal and abnormal myocardial models (McVeigh, 1996; Park et al., 1996; Edvardsen et al., 2002), to analyze cardiac activation patterns using pacemakers (McVeigh et al., 1998) and to understand the effects of treatment after myocardial infarction (Croisille et al., 1999, Gotte et al., 2001). Analysis of the motion of tag features in a series of images can be used to track myocardial material points in 3D (McVeigh and Ozturk, 2001). In this section, several popular tagged MR image-processing techniques are briefly reviewed. These techniques can be divided

into two basic approaches: feature tracking of tag lines and direct encoding of motion using phase information from tag lines.

2.2.1 Feature Tracking

2.2.1.1 Template Matching

In template matching, a tag line point was found by comparing the image brightness along a stripe of pixels to an expected tag pattern template. A tag line point was defined to be the location where the measured brightness best matches the expected template. The principle of this method is illustrated in Figure 2-7. In theory, the measurement error of the tag line point has a standard deviation of 0.9/CNR pixels, where CNR is the contrast to noise ratio of the tag pattern. In other words, the measurement error can be as low as 0.1 pixels, which has been experimentally proven (Atalar et al., 1994). To achieve such a low level of error, the template must accurately reflect the true profile of the tag patterns. An accurate template can be obtained by simulating the physics of MR tagging and imaging (Guttman et al., 1994).

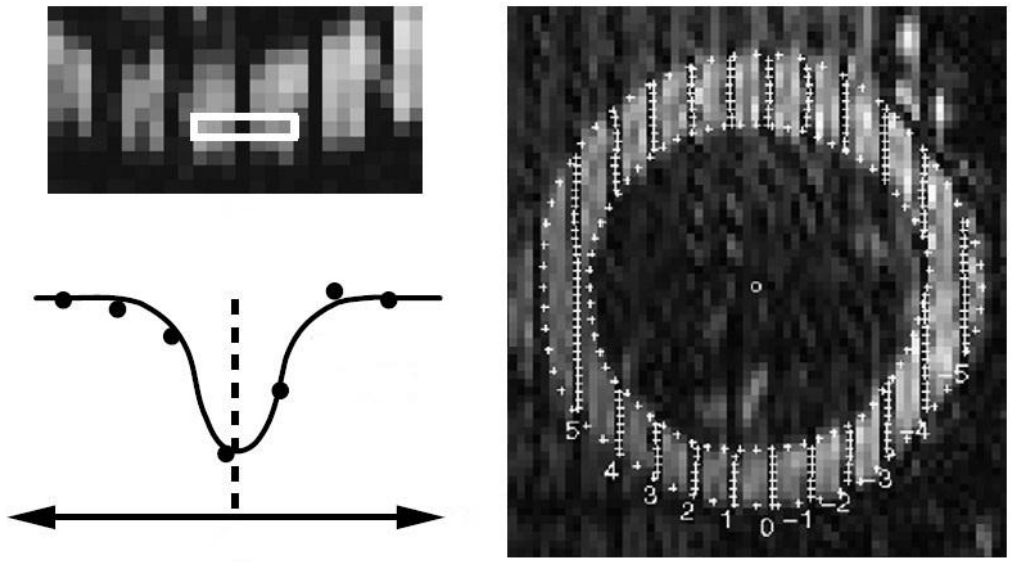

Figure 2-7. Template matching: tag lines are determined by fitting image intensities of pixels within the search region to a template (Kerwin et al.,2009)

One disadvantage of template matching is that image features other than tags, such as boundaries, are often mistaken for tags. To avoid this problem, search regions must be restricted to the myocardium. Another disadvantage is that template matching could only provide accurate motion tracking at the tag patterns. Motion within the space of the tag patterns must be obtained using interpolation, impairing the measurement resolution.

2.1.1.2 Active Geometry

In active geometry method, tag line points are identified using a curve segment that fits itself to a tag line in the image. The curve segment is assigned an energy function which has two components: E_{image}, determined in a way such that the curve segment has low energy along the tag line and $E_{internal}$, determined by the derivatives of the curve to impose continuity and smoothness of the curve. E_{image} is usually related to brightness of the image. By minimizing E_{image}, the curve will be forced towards brightness minima, tag lines.

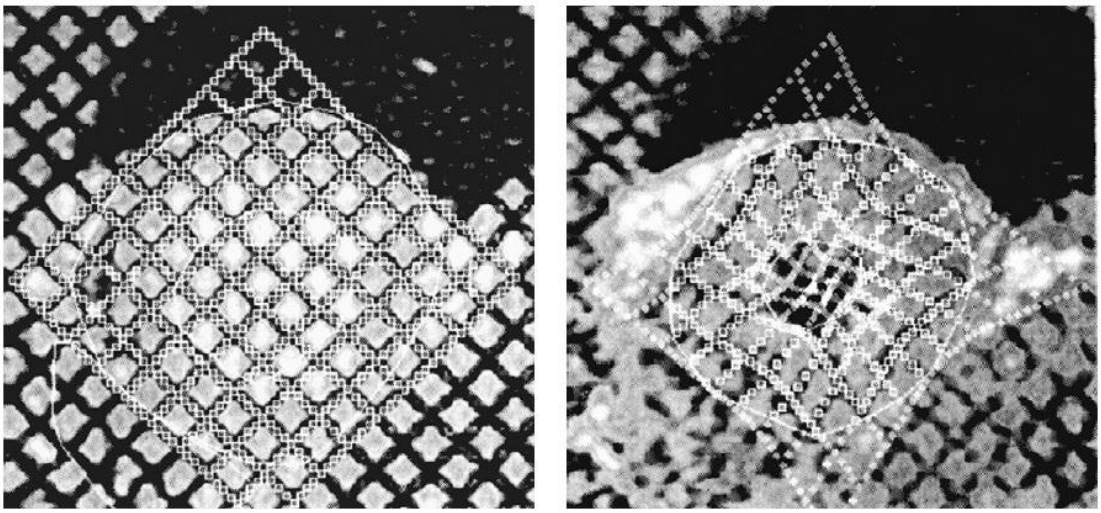

Figure 2-8. Active Geometry: a 10×10 grid of coupled snakes is superimposed on the left image, the snakes move to a deformed position after energy minimization (Adapted from Young et al., 1995)

An example of the active geometry method is shown in Figure 2-8. Young et al. (1995) used 20 curve segments with two orientations to track a grid of tag lines. An interactive, user-defined energy was added to avoid incorrect local energy minima. Another work on the active geometry is the method of Amini et al. (1998). Instead of using $E_{internal,}$ they used a set of B-spline control points to enforce the smoothness of the curve segment.

2.2.1.3 Optical Flow

Unlike tag line tracking method which can only provide accurate measurement along the tag lines, optical flow (Hildreth, 1984) can produce denser measurement by estimating the velocity of every point in an image. In the case of 2D tagged MR images, optical flow processing yields an estimate of the 2D apparent velocity field (Prince JL and McVeigh, 1992; Denney and Prince, 1994; Gupta and Prince, 1995). Gradient-based optical flow method is based on a brightness constraint equation derived by the material time derivatives of the brightness function. Constant brightness is often assumed in computer vision literature (Horn and Schunck, 1981). This assumption has been applied to tagged MRI for velocity field estimation. In the case of tagged MRI, however, the brightness of a material point changes due to tag fading. To account for this effect, Gennert and Neghadirapour (1987) proposed to model the brightness variation as a linear relationship. Prince and McVeigh estimated the brightness variation according to the imaging protocol and physical tissue property (Prince JL and McVeigh, 1992). An example application of optical flow method is shown in Figure 2-9.

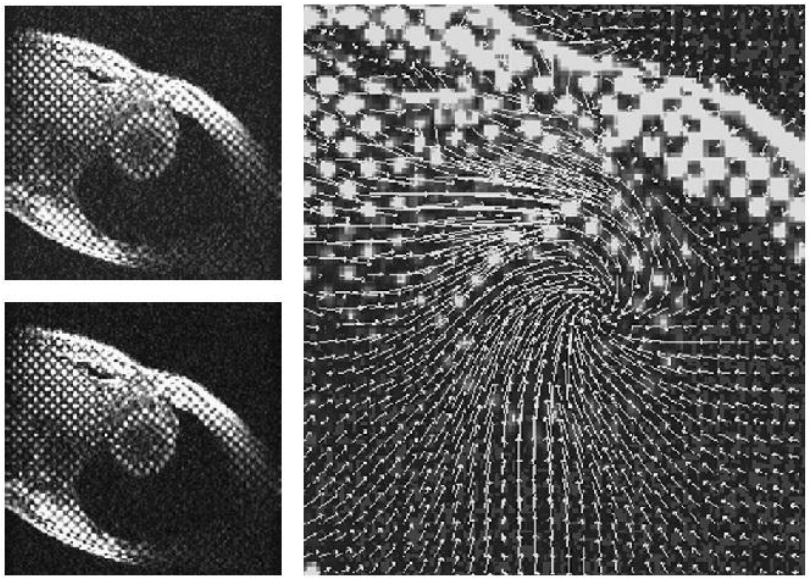

Figure 2-9. Optical flow: the left two images depict tag deformation caused by LV contraction, The right image shows the velocity field calculated by optical flow method (Adapted from Kerwin et al., 2009)

2.2.2 Direct Encoding of Motion

Although feature tracking has been the most used methods for tagged MR image analysis, the accuracies and reliability of these methods can be poor. More recent research has shown that motion can be directly encoded by phase information of the tagging method. Harmonic phase (HARP) (Osman et al., 1999; 2000) is typical among the direct encoding methods. HARP provides fast and automatic myocardial motion tracking and strain calculation from tagged MR images. The modulation of underlying magnetization produces symmetric spectral peaks in Fourier space. A bandpass filter is used to extract the harmonic peaks and the rest spectrum is zero padded. Harmonic image is obtained by performing the inverse Fourier transform of the filtered harmonic peaks. It can be expressed as

$$I(y,t) = D(y,t)\exp^{-j(w^T u(y,t)+w^T y)} \tag{2.7}$$

where $y = [y_1, y_2]^T$ is the position of tissue point within an image, $u(y,t)$ is the displacement field, w is the location of harmonic spectral peak and $D(y,t)$ is the

harmonic magnitude image which represents the blurred anatomy of the images object. Strain map is calculated from the harmonic phase image using

$$\mathrm{E(y)} = 1/2(\mathrm{H^{T}w}(\partial\emptyset/\,\partial \mathrm{y})^{-\mathrm{T}} \cdot (\partial\emptyset/\,\partial \mathrm{y})^{-1}\mathrm{w^{T}H} - \mathrm{I}) \qquad (2.8)$$

where $\mathrm{E(y)}$ is the 2D Lagrangian strain tensor, H matrices related with the tagged and imaging plane, $\emptyset(\mathrm{y}, \mathrm{t})$ is the harmonic phase image (Liu et al., 2004).

Strain maps obtained using HARP often suffer from artifacts due to image noise and spectral interference from neighboring spectral peaks. The spectral interference from DC peak is a primary source of artifacts that degrade the performance of HARP. Different image acquisition protocols and post processing techniques have been proposed to reduce the interference. Bandpass filters with different shapes and sizes were designed to optimize the extraction of the harmonic images (Osman and Prince, 2000). Automatic determination of elliptical filter parameters was proposed to minimize strain errors by studying simulated MR tagged images (Marinelli et al., 2008). Calculation of harmonic angle images was improved using a Gabor filter bank (Barajas et al., 2005; Qian et al., 2005). A composite Gabor filter designed by modeling the spectral changes of cardiac tag deformation has been proven to be superior than that of a standard Gabor filter (Davis et al., 2006). A peak-combination HARP method reduces phase errors from inhomogeneity and other magnetic field non-idealities (Ryf et al., 2004).

Complementary spatial modulation of magnetization (CSPAMM) was introduced to completely remove the DC peak (Fischer et al., 1993; Kuijer et al., 2001). In CSPAMM, a complementary acquisition is performed and subtracted with the original acquisition to cancel the DC peak. However, the longer acquisition time often results

in image misregistration and consequently affects the image quality. Although DC peak is absent, the harmonic peaks will still interfere with each other. To overcome these problems, TruHARP was proposed to totally remove unwanted harmonic peaks and can be implemented in a single breath-hold (Agarwal et al., 2010). Since five acquisitions are required, the short acquisition time of a single breath-hold often results in low SNR and constrained tag spacing.

2.3 Soft Tissue Elasticity Reconstruction

Dynamic MRE employs harmonic actuator to generate waves propagating inside soft tissue. The propagating waves are used as virtual probe to assess soft tissue elasticity. In the case of quasi-static MRE, soft tissue is perturbed at much lower frequencies and elasticity is determined from measured displacement/strain images of the deformed soft tissue. Due to the above differences, different inverse algorithms are required for dynamic MRE and quasi-static MRE.

2.3.1 Inverse Algorithms for Dynamic MRE

Two commonly used methods for dynamic MRE are local frequency estimation (Manduca *et al.,* 1996, 2001, 2003; Braun *et al.,* 2001) and direct inversion of wave equation (Manduca *et al.,* 1998; Bishop *et al.,* 2000; Oliphant *et al.,* 2001; Papazoglou *et al*., 2008; Kwon *et al.,* 2009). Most reconstructive algorithms for dynamic MRE assume the imaged object to be a homogenous, isotropic, linearly elastic material undergoing small strain. Only one wave propagating is considered and reflected

waves are ignored to simply the problem. Thus, for a propagating harmonic shear wave, shear modulus μ can be estimated by (Atay et al., 2008)

$$\mu = \frac{\rho w^2}{k^2} = \rho f^2 \lambda^2 \tag{2.9}$$

where ρ is the density of imaged object, f is the external vibration frequency, λ is the local wavelength.

2.3.2 Inverse Algorithms for Quasi-static MRE

Various elasticity reconstruction methods have been proposed to calculate soft tissue elastography from measured internal displacement field and strains. These methods can be categorized into two groups. The first group is called direct approach (Sumi et al., 1995). Soft tissue is treated as linear elastic, incompressible material in this method. Constant shear modulus is assumed on the boundary of region of interest (ROI). Relative shear modulus of soft tissue is obtained by solving a partial differential equation. The second group is iterative approach (Oberai et al., 2003). Given known boundary conditions, forward problem is solved to obtain the calculated numerical displacement/strain within ROI. Final elasticity distribution is then obtained by minimizing the error between measured and calculated displacement/strain. Each group has its own advantages and disadvantages. For iterative approach, no continuity assumptions are placed on the unknown shear modulus. It is also less sensitive to noise than a direct approach. In contrast, the direct approach is much faster than that of the iterative approach.

2.3.2.1 Direct Approach

Soft tissue and tissue-like material is usually assumed to behave as linear elastic, and isotropic material under small strains. For static deformation, the governing equilibrium is

$$\frac{\partial \sigma_{ij}}{x_j} + f_i = 0 \qquad \{i, j = 1,2,3\} \tag{2.10}$$

where σ_{ij} is the second ranked symmetric stress tensor and f_i is the body force per unit volume acting on the body in the x_i direction (Skovoroda et al., 1995).

Incompressibility is often assumed and a pseudo-constitutive equation is obtained as

$$\sigma_{ij} = p\delta_{ij} + 2\mu\varepsilon_{ij} \tag{2.11}$$

where δ_{ij} is the Kronecker delta, p is the mean normal stress, μ is the shear modulus, and ε_{ij} is the second ranked symmetric strain tensor.

In the case of 2D inverse problem, Equation 2.10 and Equation 2.11 can be rearranged to yield a linear partial differential equation for μ:

$$\frac{\partial \mu}{\partial x_3} = 0 \tag{2.12}$$

and

$$\mathrm{A}\left(\frac{\partial \mu}{\partial x_1}\frac{1}{\mu}, \frac{\partial \mu}{\partial x_2}\frac{1}{\mu}\right)^{\mathrm{T}} = -\mathrm{B}. \tag{2.13}$$

A and B are matrices depending on the strain and strain derivatives in x_1 and $x_2$directions:

$$\mathrm{A} = \begin{pmatrix} 2\varepsilon_{11}+\varepsilon_{22} & \varepsilon_{12} \\ \varepsilon_{21} & \varepsilon_{11}+2\varepsilon_{22} \end{pmatrix} \tag{2.14}$$

and

$$\mathrm{B} = \begin{pmatrix} \frac{\partial(2\varepsilon_{11}+\varepsilon_{22})}{\partial x_1} & \frac{\partial \varepsilon_{12}}{\partial x_2} \\ \frac{\partial \varepsilon_{21}}{\partial x_1} & \frac{\partial(\varepsilon_{11}+2\varepsilon_{22})}{\partial x_2} \end{pmatrix}. \tag{2.15}$$

At points where the determinant of A is not zero, the derivative of the relative shear modulus can be obtained as:

$$\mathrm{div}(\mathrm{In}\mu) = -\mathrm{A}^{-1}\mathrm{B}. \tag{2.16}$$

Using line integration, the shear modulus at any point (x_1, x_2) along the surface s relative to a starting point (a_1, a_2) can be determined by:

$$\frac{\mu(x_1,x_2)}{\mu(a_1,a_2)} = \exp\left(-\int_s (-\mathrm{A}^{-1}\mathrm{B})\right) \tag{2.17}$$

The advantage of the direct method is that it is fast compared to the iterative method. However, it assumes that all components of strain tensor are known and that $\mu(x_1, x_2)$ is first order differentiable. Moreover, noisy data has to be differentiated to estimate the strain field, which further impairs the accuracy of the elasticity calculation.

2.3.2.2 Iterative Approach

Iterative approaches generally use the weak form of the equilibrium equations. The iterative approach can be summarized as follows (Barbone and Bambe, 2002):

(i) Given $u_{measured}(\mathrm{x}_1, \mathrm{x}_2)$.

(ii) Guess a distribution for $\mu(\mathrm{x}_1, \mathrm{x}_2)$.

(iii) Evaluate $u_{predicted}(\mathrm{x}_1, \mathrm{x}_2)$ by solving the forward elasticity problem.

(iv) Find $\mu(\mathrm{x}_1, \mathrm{x}_2)$ that minimizes $\left|u_{measured}(\mathrm{x}_1, \mathrm{x}_2) - u_{predicted}(\mathrm{x}_1, \mathrm{x}_2)\right|$.

The $u_{measured}(x_1, x_2)$ and $u_{predicted}(x_1, x_2)$ are the measured and predicted soft tissue displacement field respectively. $\mu(x_1, x_2)$ is the shear modulus distribution of soft tissue. The iterative approach has some advantages over the direct approach. Firstly, the forward problem can be efficiently solved using commercialized FE packages. Secondly, no continuity assumptions are placed on $\mu(x_1, x_2)$, so arbitrary jumps in modulus can be captured. Thirdly, the iterative approach is relatively less sensitive to the noise of data than the direct approach. One obvious drawback in comparison to the direct approach is computational speed. Step (iii) requires the solution of forward problem to be determined many times.

CHAPTER 3 TAGGED MR IMAGE ACQUISITION

Most image acquisition methods for MRE have been focused on utilizing motion sensitive gradient (MSG) integrated phase contrast imaging sequences with harmonic actuation system (Hamhaber et al., 2007; Yin et al., 2007; Kruse et al., 2008). These image acquisition methods are designed only to capture propagating waves inside soft tissue and are not suitable for quasi-static MRE which requires imaging the quasi-static deformation of soft tissue. Moreover, these image acquisition methods require extensive programming of imaging sequence which can be challenging. To date, there is a lack of effective image acquisition methods available for quasi-static MRE. In this chapter, we present a new image acquisition system for quasi-static MRE using tagged MR imaging sequence.

Tagged MR utilizes spatial modulation of magnetization (SPAMM) imaging sequence to encode soft tissue deformation. We described the basic principle of SPAMM imaging sequence and introduced the ultrasonic motor controller developed using LabView. ECG signal was simulated using function generator and outputted to both the MR scanner and controller for synchronization. Design and fabrication of the actuator was introduced, and MR compatibility was tested. Tagged MR images of agar gel phantom and human lower leg were acquired using this image acquisition system. Experimental results showed that this image acquisition system is an effective method to track soft tissue deformation.

3.1 Imaging System Development

3.1.1 Spatial Modulation of Magnetization

The concept of spin tagging was first used for measurement of blood velocity (Morse and Singer, 1970). This concept was applied by Zerhouni et al. (1988) using selective radio frequency (RF) excitation to generate saturated parallel planes within the heart wall to visualize myocardial motion. Axel and Dougherty (1989) subsequently developed a more efficient method, SPAMM, which uses non-selective excitation to produce saturated parallel planes throughout the entire imaging volume within a few milliseconds. Generally, tagged MR imaging can be divided into two stages: (1) producing a spatially modulated pattern of saturated magnetization in using a combination of RF and gradient pulses, and (2) imaging the deformation of the tag using ECG-gated pulse sequence (Axel et al., 2005). The saturated tags fade due to T1 relaxation and repeated RF excitations during imaging (Reeder and McVeigh, 1994).

RF tagging pulses are used to spatially label an image with a specified physical or physiological property. A series of parallel stripes or orthogonal grids can be placed on an image using tagging pulse. These stripes or grids are usually referred to as tags. The deformation of tags indicates the displacement within an imaged object. Tags are typically applied as a magnetization preparation pulse prior to the actual imaging pulse sequence. Virtually, any imaging pulse sequence can be combined with a tagging pulse sequence or a train of tagging pulses. A tagging gradient is generally required to generate the desired spatial pattern. Many forms of tags can be placed using tagging pulse. We focus on the tagging pulse that produces a grid on the imaged object.

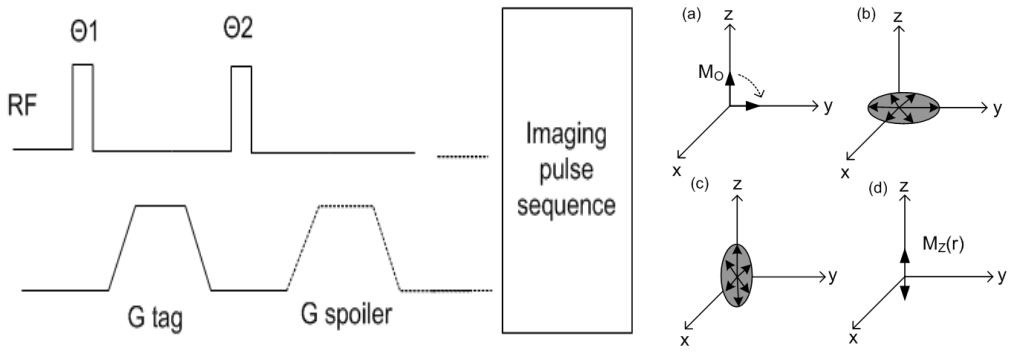

(a) (b)

Figure 3-1. Imaging principle. (a) A SPAMM sequence with two RF pulses, (b) evolution of magnetization

A simplest form of SPAMM consisting two RF pulses with a tagging gradient inserted in between is shown in Figure 3-1(a). A spoiler gradient pulse (dotted line in Figure 3-1(a)) is often applied after the second RF pulse. For the ease of description, we assume that both the RF pulses are applied along x axis and have the same flip angle of 90°. Magnetization is shifted to the transverse plane by the first RF pulse. The tagging gradient then produces phase dispersion in the excited transverse magnetization. The phase dispersion means the magnetization vector eventually has a degree depending on its spatial location. The second RF pulse rotates the magnetization from xy plane to xz plane. After the transverse magnetization is dephased by a spoiler gradient, only the longitudinal magnetization remains. The amplitude of the longitudinal magnetization $M_z(r)$ is spatially modulated resulting in a stripe-tagging image. The magnetization evolution diagram is shown in Figure 3-1(b). Multiple sets of tags can be created along different directions on an image. Grid-tagging image can be generated by placing two orthogonal sets of tags (Axel and Dougherty, 1989). After tags are placed on images, deformation of imaged object will cause the tags to deform accordingly. The saturated tags fade due to T1 relaxation and repeated RF excitations during imaging (Axel et al., 2005). ECG-gated imaging

sequence is used in our method to acquire tag-deformed image. Standard ECG signal and waveform names are shown in Figure 3-2(a).

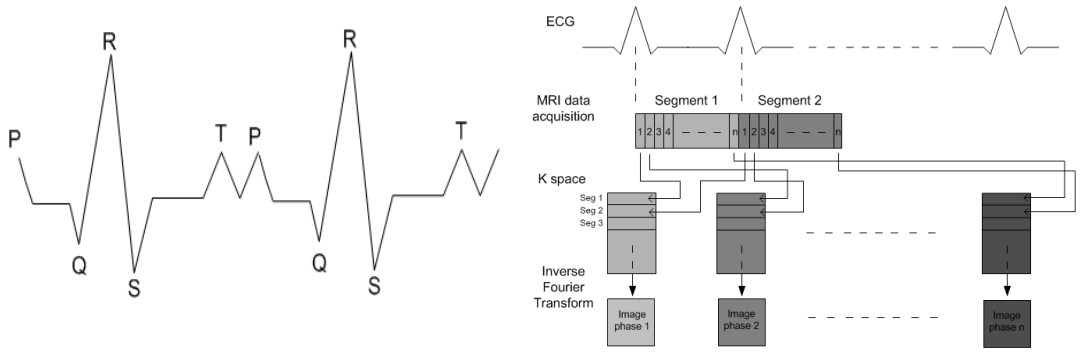

(a) (b)

Figure 3-2. K-space fill up of SPAMM. (a) Simulated ECG signal, (b) k-space data acquisition principle

3.1.2 Actuation System Design

ECG signal of 1Hz was simulated using Function generator with BENCH software which enables hand drawing of output waveform. ECG signal was outputted to both the motor controller and MR scanner. MRI k-space data acquisition was synchronized with the simulated ECG signal. Specific k-space segment data was acquired and filled into corresponding images repeatedly after each ECG period. Twenty images were acquired over multiple ECG periods within time duration of 10-20s with GE SIGNA 1.5T MRI Scanner. MRI k-space data acquisition diagram is shown in Figure 3-2(b). Ultrasonic motor was controlled by microprocessor based controller interfaced with USB-6221 DAQ device. The control software and signal processing was implemented using LabView version 8.6. Actuator was driven at the same frequency as that of the ECG signal to couple with the ECG-triggered SPAMM imaging sequence. The overview of this actuation system is shown in Figure 3-3.

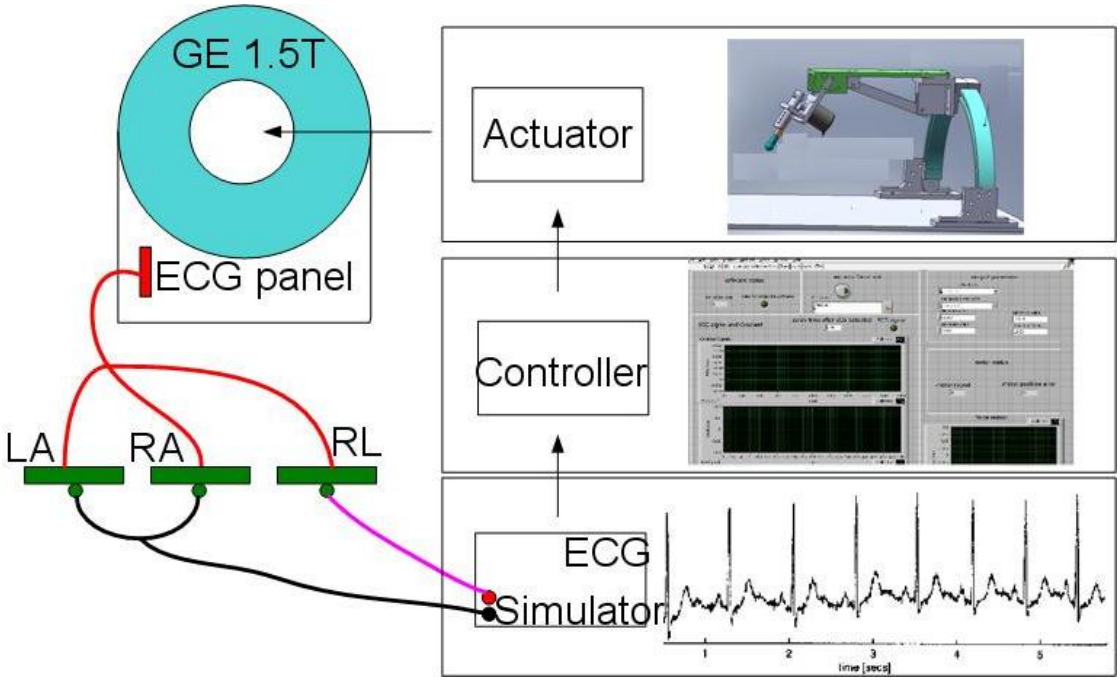

Figure 3-3. Overview of the actuation system

The actuator was made of an ultrasonic motor, a force sensor and motion-transmission mechanism. Indenter tips with different shape and area can be chosen according to different experiment conditions. Transmission shaft was deviated from the motor shaft by 5mm to acquire a maximum indentation depth of 10mm. The complete computer aided design (CAD) model and fabricated prototype are shown in Figure 3-4(a) and Figure 3-4(b) respectively.

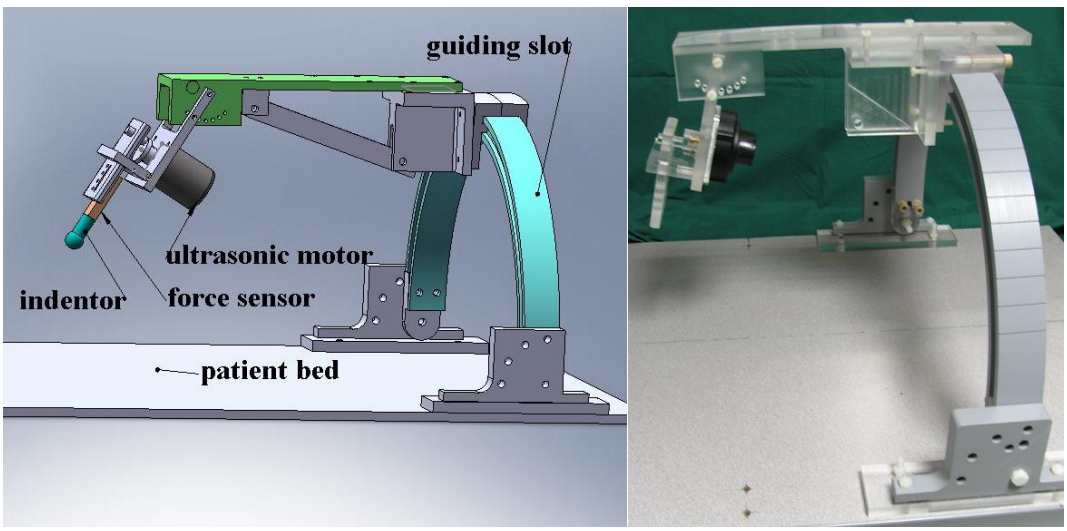

(a) (b)

Figure 3-4. MR compatible actuation device. (a) CAD design of actuation device, (b) fabricated actuator device

High torque ultrasonic motor, USR60-E3 by Shinsei Corporation, Japan, was selected considering both its MR compatibility and the requirement of sufficient deformation of the nearly incompressible soft tissue. A MR compatible force sensor was made of strain gauges and shield material. All the motion-transmission parts were fabricated using plastic. To test the influence of the MRI magnetic field, force measurement was carried out both inside and outside of the MR scanner. Circuits of the strain gauge were well shielded to isolate the magnetic field from that of the MR scanner. This can prevent them from interfering with each other and reduce the noise level (Rajendra et al., 2008). Force sensor with and without shield is shown in Figure 3-5.

Figure 3-5. MR compatible force sensor made of stain gauge without and with shield

3.1.3 MR Compatibility Test

High-quality MR imaging requires a very stable homogeneous main magnetic field and linear gradient fields. Magnetic susceptibility material, typically known as ferromagnetic metal, can cause serious distortion on images. It is crucial to test the MR compatibility of the actuator.

Both MR images and force sensor signal were analyzed to investigate the MR compatibility. Images with the actuator power on were acquired and compared with normal images. The images are shown in Figure 3-6. Neither severe artifacts nor

image distortion can be observed in MR images taken by T1 weighted imaging sequence.

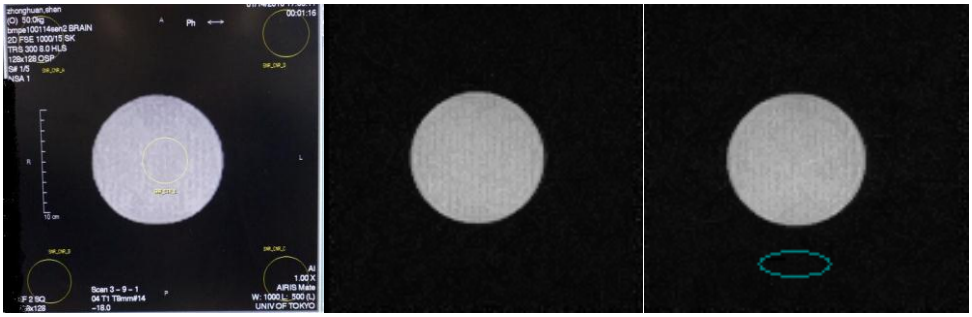

(a) (b) (c)

Figure 3-6. T1 weighted MR images, (a) without actuator, (b) with actuator power on. (c) The ellipsoid represents location of the actuator

Signal to noise ratio (SNR) was calculated and provided by MR scanner. The SNR was the ratio of the average intensity at the center of a MR image and the average value of the standard deviation at each corner of the image. The SNRs of image (a) and image (b) of Figure 3-6 are 57.03 and 52.05 respectively. Meanwhile, force sensor signal was also recorded to study the influence of MR gradient field. Force sensor signal was plotted together with the imaging gradient in Figure 3-7. We can observe that the force sensor signal has no obvious fluctuation during imaging. This illustrated the capability of the shielded force sensor to function well in magnetic field environment.

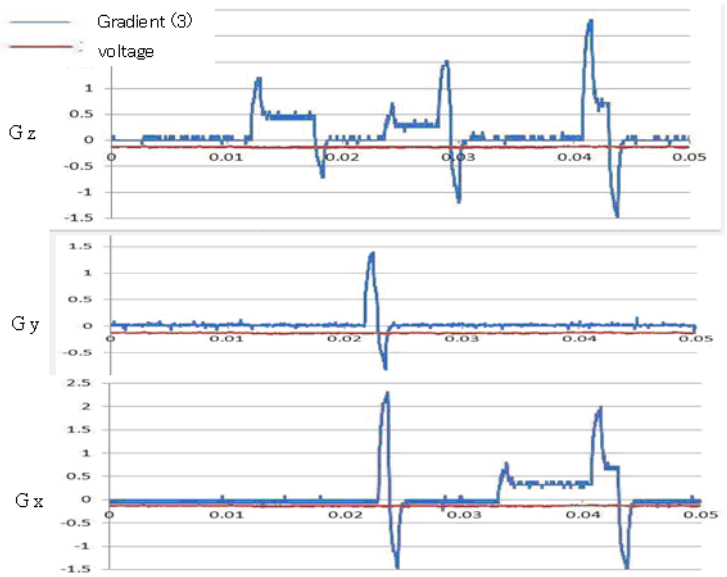

Figure 3-7. Investigation of the interference of the imaging gradient on the force sensor signal (red line)

3.2 Experiments

3.2.1 Phantom Compression

Cylindrical agar gel phantom was made with one cylindrical soft inclusion. T1-weigthed MR image was acquired to reveal the anatomy of the phantom (Figure 3-8). The concentration of the phantom was 1% for the outer layer and 0.5% for the soft inclusion. The soft inclusion was made for the purpose of elasticity reconstruction. Sixteen tagged images were acquired for both axial and sagittal directions using our MR-compatible actuation system with 60 heart beats per minute and a simulated ECG. The phantom was compressed from the top using a plate. The maximum compression distance was 10mm. The imaging parameters were as follows: flip angle, 10°; tag orientation, 45°; tagging space, 8mm, echo time (TE), 3.96msec; repetition time (TR), 41msec; slice thickness, 6mm; field of view (FOV), 27×34 cm. The first and ninth frame of the tagged image sequence in both directions is shown in Figure 3-9.

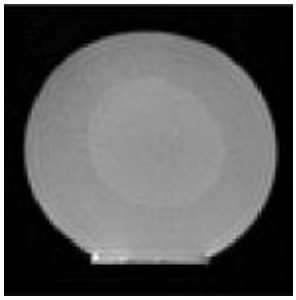

Figure 3-8. T1-MR image of agar gel phantom

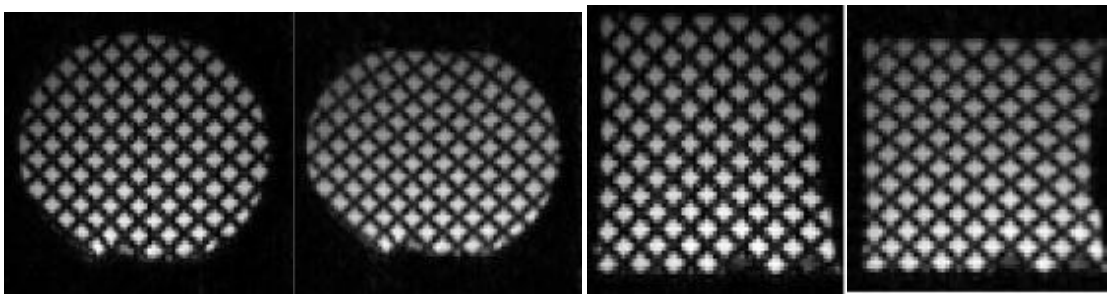

(a) (b) (c) (d)

Figure 3-9. Tagged MR images of agar gel phantom. (a)-(b) The first and ninth frame of axial tagged images, (c)-(d) the first and ninth frame of sagittal tagged images

3.2.2 Soft Tissue Indentation

Indentation experiment was conducted on a volunteer's lower leg. Indentation force was recorded by a force sensor. The lower leg was indented at the top middle region of the leg using a sphere-shaped indenter with a diameter of 15mm (Figure 3-10). MR tags were generated by applying the tagging sequence immediately after the detection of the R-wave. Gradient-echo images were acquired during the entire imaging cycle to capture the displacement of the tags. Tagging period of 5mm was used. Other imaging parameters were as follows: flip angle, 15°; tag orientation, 45°; TE, 1.704msec; TR, 6.032msec; slice thickness, 15mm; spacing between slices, 15mm; FOV, 20×20 cm. Different frames of the tagged images are shown in Figure 3-11.

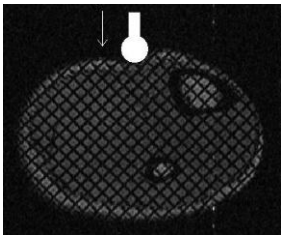

Figure 3-10. Human lower leg indentation diagram

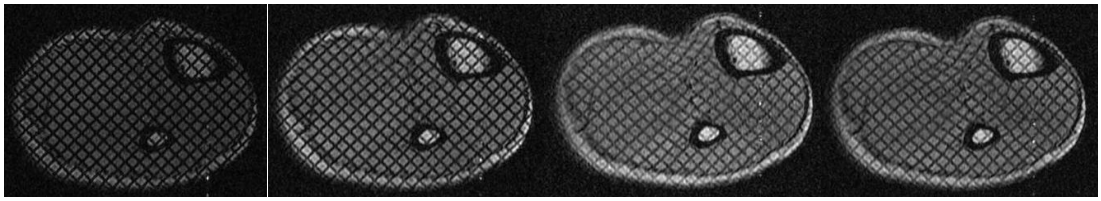

(a) (b) (c) (d)

Figure 3-11. Tagged MR images of human lower leg. (a)-(d) Frame 1,3,5,7

3.3 Discussions and Conclusion

In this chapter, a new image acquisition system was presented and tested to track internal deformation of soft tissue. Using this method, we extend the use of tagged MRI sequence from myocardial tissue to other soft tissue. Since SPAMM is available in almost every clinical MR scanner and there is no need to detect imaging gradient from MR gradient cabinet, this imaging method is easy to implement. Experimental results demonstrated the feasibility of the proposed image acquisition system for soft tissue deformation tracking.

During imaging, blood flow can cause induced voltage to impose on ECG signal. This is because of the main magnetic field and the switching of imaging gradient. The T waveform of ECG will rise once the patient enters the MRI gantry. The affected T waveform may cover the R waveform, which is a big challenge for ECG detection. Since the proposed imaging method use simulated ECG signal, there is no such problem for ECG detection. During abdominal imaging, patients are usually required to hold their breath for 15-20s to avoid image artifacts due to breathing motion. 3D

abdominal tag imaging is usually difficult due to their long imaging time (breath-hold time). This may be avoided using a coupled breath gate. The application of 3D tagged MRI can be extended to other organs using the proposed imaging method.

In MRE, indentation is performed percutaneously through the abdominal skin and fat layer to the targeted organs within the human body. It is hard to acquire deep deformation of abdominal organs. However, for organs that are in contact with heart, for example, liver will vibrate accordingly with the heartbeat. Liver tissue deformation can therefore be tracked by using human ECG signal directly. An alternative way to acquire deep deformation would be to use a needle inserted into the targeted region. A needle within the organ will transmit the actuation to deep region of the imaged organ despite of its invasive attribute.

CHAPTER 4 TAGGED MR IMAGES ANALYSIS

Tagged MR images are not directly interpretable, sophisticated image processing methods are needed to produce meaningful displacement field and strain images. Since tagged MR image sequence is originally designed for cardiac imaging, various tagged MR image processing techniques have been proposed for myocardial function evaluation. However, accuracy and computational efficiency of the processing algorithms needs to be improved for accurate diagnosis of myocardial diseases and for our purpose, elasticity reconstruction of soft tissue.

Template matching (Atalar and McVeigh, 1994; Guttman et al., 1994; Kerwin and Prince, 1999; Deng and Thomas, 2005), active geometry (Kumar and Goldgof, 1993; Amini et al., 1998; Clarysse et al., 2000; Rougon et al., 2005; Qian et al., 2005), optical flow (Prince and McVeigh, 1992; Denney and Prince, 1994; Gupta and Prince, 1995; Haber et al., 2001) and harmonic phase (HARP) (Osman et al., 1999) are the main methods for tagged MR images processing. Template matching methods calculate the displacement by tracking the tag lines. Optical flow is advantageous over template matching in providing a dense estimation of the motion field instead of a sparse set of data located at the tag lines. However, the optical flow methods require a material point with constant brightness which is not available for tagged MR images due to tag fading. The HARP method proposed by Osman et al. (2000) is widely used in cardiac image processing (Osman et al., 2000; Osman and Prince, 2000; Liu et al., 2004; Pan et al., 2005; Venkatesh et al., 2010).

In section 4.1, we introduced an enhanced HARP method which extends conventional HARP for large motion tracking. Results were illustrated on both agar gel phantoms and human lower leg. In section 4.2, an accurate and fast method, adaptive windowed harmonic phase (AWHARP), is developed for strain calculation of tagged MR images. Improved strain calculation contributes to accurate reconstruction of soft tissue elasticity. Tagged MR images of hearts with hypertrophic cardiomyopathy were processed and compared with that of normal hearts. We demonstrated that AWHARP can help clinicians to detect left ventricle (LV) dysfunctions and myocardial diseases by producing accurate strain images.

4.1 Enhanced Harmonic Phase

4.1.1 Large Motion Tracking

Spatial modulation of magnetization (SPAMM) sequence modulates the longitudinal magnetization in a sinusoidal manner, which produces an array of spectral peaks (harmonic peaks) in the Fourier domain (k-space). A circular band-pass filter is often used to extract the off-center harmonic peaks. Harmonic phase image can be calculated by applying the inverse Fourier transform of a harmonic peak. Since the harmonic image is complex, it has both magnitude and phase at each pixel. The magnitude image reflects the anatomy of the lower leg and is used for segmentation of the leg. The harmonic phase angle of the leg can be used to infer the tissue material property and remains invariant through the image sequences (Zhang et al., 1996). Displacement distribution and strain maps are calculated from these harmonic phase images.

The phase of the image at time t is given by

$$\emptyset(y,t) = w^T x(y,t) \tag{4.1}$$

where $\emptyset(y,t)$ is the phase, w is the frequency vector of a harmonic spectral peak, x is the spatial position, y is the image coordinate. At time *t*, the phase shift can be calculated as

$$\emptyset(y,t) - \emptyset(y,0) = w^T\big(x(y,t) - x(y,0)\big) = w^T u(y) \tag{4.2}$$

where $u(y)$ is the displacement vector. Since the phase $\emptyset(y,t)$ differs from the harmonic phase angle $a(y,t)$ by a multiple of *2π*,

$$\Delta a = wrap\big(a(y,t) - a(y,0)\big) = wrap\big(w^T u(y)\big) \tag{4.3}$$

where the nonlinear wrapping function is given by

$$wrap(\emptyset) = mod(\emptyset + \pi, 2\pi) - \pi. \tag{4.4}$$

If $|w^T u(y)| < \pi$, $u(y)$ can be calculated by

$$u(y) = (w^T)^{-1}\Delta a. \tag{4.5}$$

If $|w^T u(y)| > \pi$, Δa is always wrapped. For soft tissue indentation, it is reasonable to assume that the displacement varies smoothly within the soft tissue. Given this assumption, $w^T u(y)$can be calculated by unwrapping Δa starting from a pixel where $|w^T u(y)| < \pi$ is satisfied. In this study, a quality guided phase unwrapping method is used.

Figure 4-1 shows the tagged MR image to be processed. Bones of the lower leg were segmented and excluded from the strain map computation. We processed only soft tissue of the leg. A circular band-pass filter with radius of 1.56mm was used to extract the off-center harmonic peak. The calculated harmonic phase image of one direction is shown in Figure 4-2(a). We observed from Figure 4-2(b) that the tag lines corresponded well with the wrapped harmonic phase lines. Since the lower leg was indented from the top and around the middle region of the leg, the left and right

regions of the lower leg were expectedly having negative and positive displacement values respectively in the x direction (Figure 4-3(a)). In the y direction, area located near the indenter has larger displacement (Figure 4-3(b)).

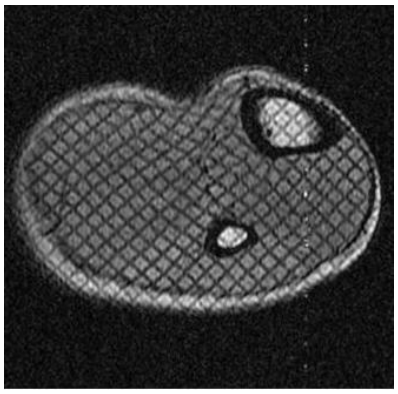

Figure 4-1. Frame 7 of tagged MR image of human lower leg

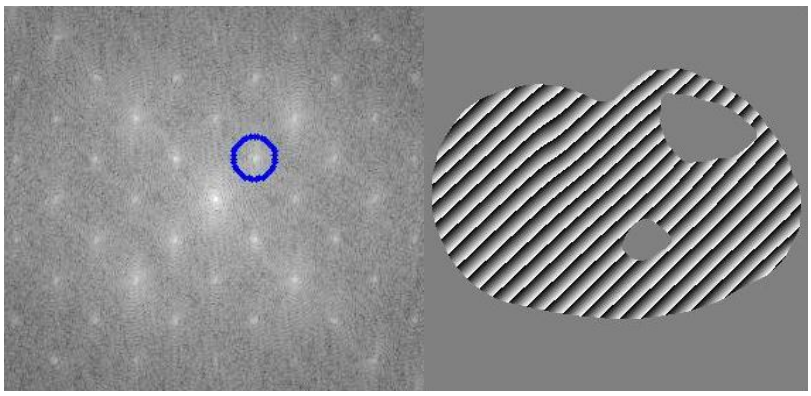

(a) (b)

Figure 4-2. Phase image calculation. (a) Band-pass filter in Fourier domain, (b) wrapped harmonic phase image in one direction

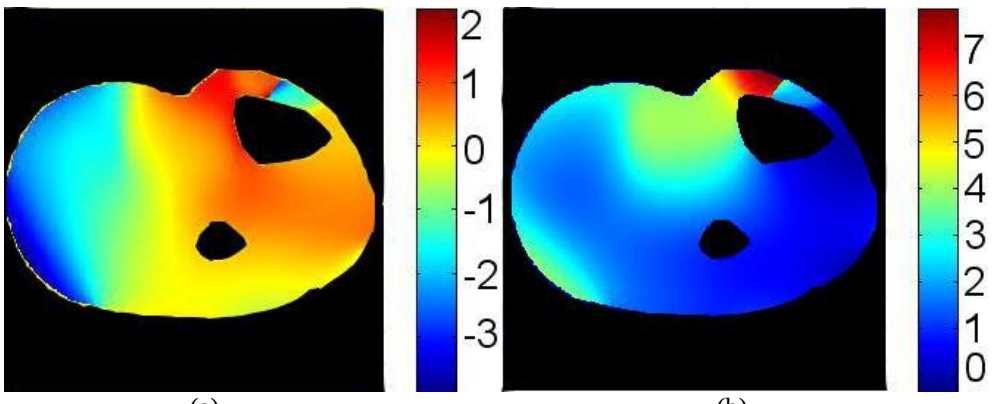

(a) (b)

Figure 4-3. Displacement field. (a) Displacement in the $\boldsymbol{x}$ direction (unit: mm), (b) displacement in the $\boldsymbol{y}$ direction (unit: mm)

4.1.2 Strain Image Computation

Once the displacement field $u(y)$ is calculated, the deformation gradient tensor of the lower leg is given by

$$F = \nabla_{\mathrm{y}} u(y) + I. \tag{4.6}$$

Therefore the 2D Lagrangian strain tensor can be calculated as

$$E = \frac{1}{2}(F^T F - I). \tag{4.7}$$

However, this method does not perform well in the presence of noise since the phase unwrapping procedure is needed to calculate $u(y)$. The strain map is calculated using

$$E(y) = \frac{1}{2}\left(H^T w \left(\frac{\partial \emptyset}{\partial y}\right)^{-T} \cdot \left(\frac{\partial \emptyset}{\partial y}\right)^{-1} w^{\mathrm{T}} H - I\right) \tag{4.8}$$

where $E(y)$ is the 2D Lagrangian strain, H matrices related with the tagging and imaging plane.

4.1.2.1 Validation using Simulated Tagged Images

Simulated tagged images were used to validate the strain calculation. The simulated tagged images were constructed by applying sinusoidal modulation to a digital circular image. A circular band-pass filter was used to extract the off-center harmonic peak. The radius of the filter was chosen at one third of the tagging frequency. Stretch strains ranging from 0.1 to 0.4 and shear strains ranging from 0.05 to 0.2 were constructed and processed (Figure 4-4(a-e)). 100% Gaussian white noise was added to test the sensitivity of the algorithm to noise. The calculated strains showed good agreement with the true values. The error of E_{xx} was calculated to be within ±8.07% and ±7.21% for images with and without noise respectively. The error of E_{xy} was

within ±14.95% and ±13.65% for images with and without noise respectively. The strain calculation is accurate even in the presence of noise (Figure 4-5(a-d)).

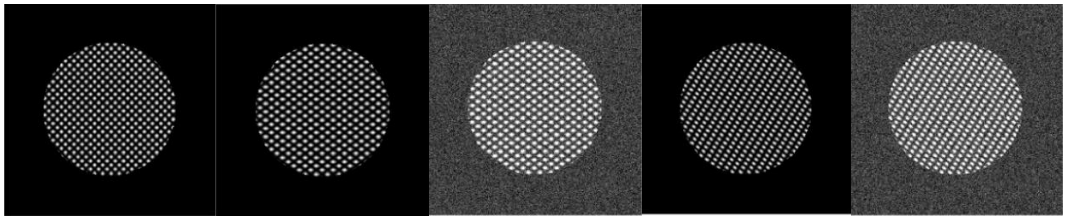

(a) (b) (c) (d) (e)

Figure 4-4. Simulated images. (a) Reference image, (b) deformed image of $\boldsymbol{E_{xx} = 0.4}$ without noise, (c) deformed image of $\boldsymbol{E_{xx} = 0.4}$ with noise, (d) deformed image of $\boldsymbol{E_{xy} = 0.2}$ without noise, (e) deformed image of $\boldsymbol{E_{xy} = 0.2}$ with noise

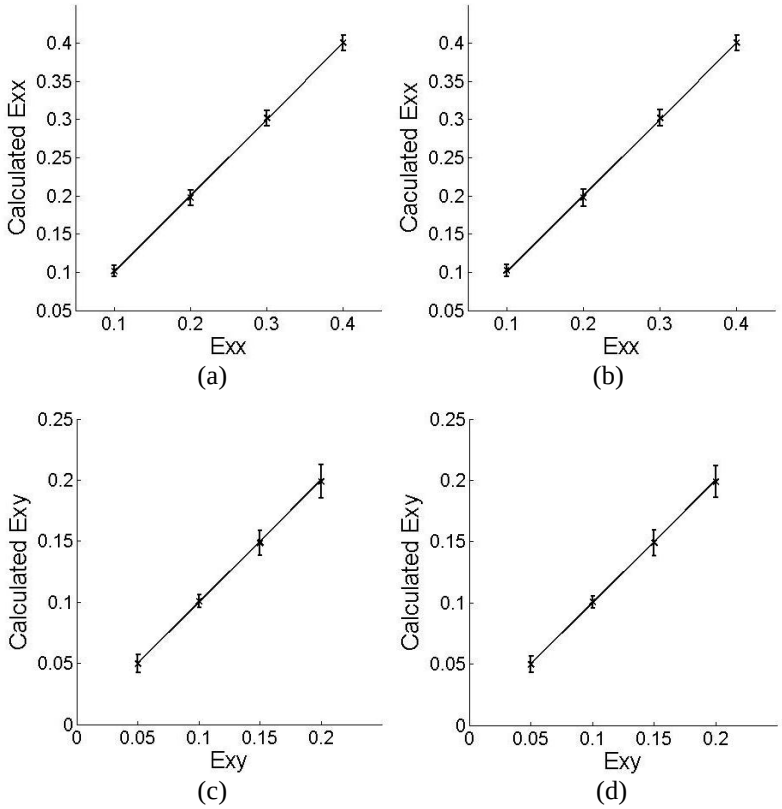

(a) (b) (c) (d)

Figure 4-5. Strain calculation with simulated images. (a) Calculated strain of $\boldsymbol{E_{xx}}$ without noise, (b) calculated strain of $\boldsymbol{E_{xx}}$ with noise, (c) calculated strain of $\boldsymbol{E_{xy}}$ without noise, (d) calculated strain of $\boldsymbol{E_{xy}}$ with noise

4.1.2.2 Human Lower Leg Indentation

Figure 4-1 shows the tagged MR image to be processed. Since the lower leg was compressed, negative strain values were expected to dominate in both directions. In y direction, smaller strain values were shown in areas away from the indenter and behind the bones (Figure 4-6(b)). Due to the presence of noise, strain variation was observed in the bottom left and top right regions.

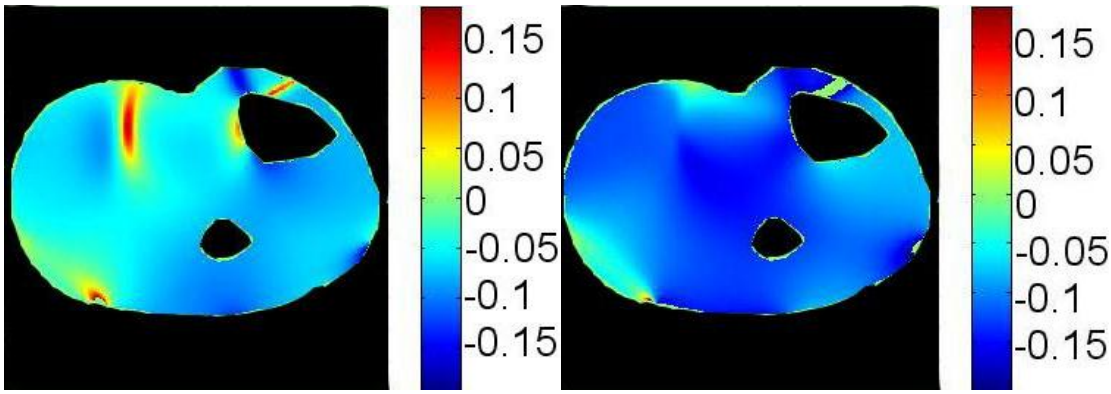

(a) (b)

Figure 4-6. Lagrangian strain images. (a) Strain in the $\boldsymbol{x}$ direction, (b) strain in the $\boldsymbol{y}$ direction

4.1.2.3 Agar Phantom Compression

Figure 4-7 shows the tagged MR images of the deformed agar gel phantom. Resultant strain images are shown in Figure 4-8. The concentration of the phantom was 1% for the outer layer and 0.5% for the soft inclusion. Bigger strain values were observed at regions where the soft inclusions were located (indicated by dotted lines).

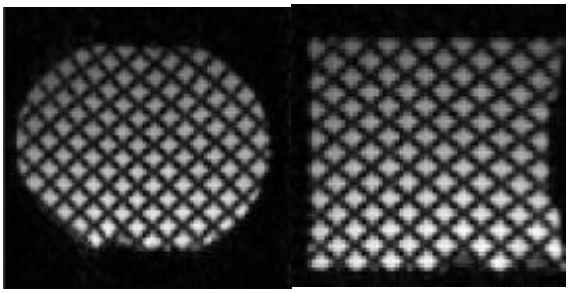

(a) (b)

Figure 4-7. Deformed tagged MR images of agar gel phantom. (a) The ninth frame of axial tagged images, (b) the ninth frame of sagittal tagged images

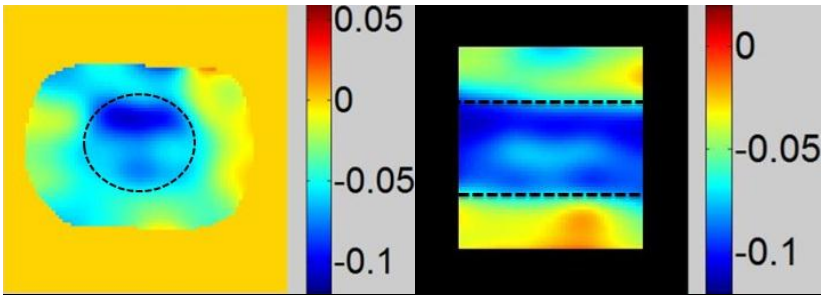

Figure 4-8. Strain maps obtained with tagged phantom images. (a) Axial image, (b) sagittal image

4.2 Analysis of Myocardial Tagged MR images

Tagged MR imaging allows comprehensive and noninvasive assessment of regional myocardial contractile performance. It provides reliable quantification and visualization of cardiac motion and strains. Generally, two families of methods have been proposed to analyze tagged cardiac MR images. One family is the feature tracking method including template matching active geometry and optical flow. These methods compute cardiac motion by tag line detection and interpolation. A finite element model of the heart was also used in the active geometry approach (Young et al., 1994). The other family is the spectrum based method such as HARP, SinMod (Arts et al., 2010). HARP extracts the phase of the complex tagged image by filtering the harmonic spectral peaks which correspond to the magnetization modulation. The advantage of the first family is that it provides motion tracking and strain images with smoothness and continuity due to their intrinsic interpolation. However, these

methods are usually computationally expensive. The main advantage of the second family is that it allows the recovery of a dense displacement field by making use of the underlying phase information. However, it is difficult to design proper filters that produce strain images with both high smoothness and high strain resolution. Recently, methods that combine the advantages of the two families have been proposed (Chen et al., 2010; Wang and Amini, 2010). Apparently, all these spectrum based methods would benefit from a more precise extraction of the local phase images of the tagged MR images.

In the HARP method, a band pass filter is used to extract the harmonic spectral peaks. Band pass filters with different shapes and sizes were designed to optimize the extraction of the phase images (Osman and Prince, 2000; Barajas et al., 2005; Marinelli et al., 2008). However, HARP method is limited by the use of a common filter for all spatial positions, although tag pattern of the MR image changes its spacing and orientation. Gabor filter banks have been used to improve the phase extraction process (Chen et al., 2010; Barajas et al., 2005), but this method depends on a heuristic combination of the Gabor filter outputs, and may result in unsmooth phase images (Chen et al., 2010). A windowed Fourier based method was introduced to improve the accuracy of the phase images (Cordero-Grande et al., 2011). Nevertheless, the width of the window is fixed for the whole image and no criterion is given for the choice of the window width. Due to the local changes of tag spacing and orientation, a fixed window width may not provide an optimal representation of local spectra. In this section, an Adaptive Windowed Harmonic Phase (AWHARP) method is proposed using Adaptive Windowed Fourier Transform (AWFT) and 2D Gabor Wavelet Transform (2D-GWT). Local spatial frequencies are first calculated using

2D-GWT. The widths of the adaptive windows are determined according to the instantaneous local spatial frequencies. Global first harmonic spectral peaks are obtained by summing up the first harmonic peaks of each windowed tagged image. Phase images are calculated by performing inverse Fourier transform on the global first harmonic spectral peaks.

4.2.1 Cardiac Tag Simulator

4.2.1.1 Analytical Motion Field

Grid-tagged SPAMM and CSPAMM images were simulated in this study. The displacement of the LV is defined by an analytical expression. Simulation enables the calculated strain images to be compared with the corresponding true strain images. The LV displacement field was modeled as a deformable and incompressible cylinder. Displacement field has been presented in cylindrical coordinates by (Kuijer et al., 2001):

$$\begin{pmatrix} r \\ \theta \\ z \end{pmatrix} = \begin{pmatrix} r(R) \\ \varphi R + \Theta + \varepsilon \\ \lambda Z \end{pmatrix} \tag{4.9}$$

where (R, Θ, Z) and (r, θ, z) are related to the myocardial point position of the undeformed and deformed state respectively. The function $r(R)$is given by:

$$r(R) = \sqrt{r_i^2 + \frac{1}{\lambda}\left(R^2 - R_i^2\right)} \tag{4.10}$$

where R_i and r_i are the inner radius of the cylinder before and after deformation respectively. The deformation parameters in the end-systolic state were chosen to be $R_i = 25\,\text{mm}$, $r_i = 15\,\text{mm}$, initial outer radius 35mm, rigid body rotation $\varepsilon = 3^\circ$, $R - \Theta$

shear $\phi = 0.1^{\circ}$/ mm and longitudinal contraction $\lambda = 0.8$. The gradient deformation tensor of the analytical displacement field is given by (Douglas et al., 1990):

$$F = \begin{bmatrix} \partial r/\partial R & 0 & 0 \\ r\phi & r/R & 0 \\ 0 & 0 & \lambda \end{bmatrix}. \tag{4.11}$$

4.2.1.2 Tag Generation

The magnitude I(x, y, t) of a 1-1 SPAMM tag pattern acquired after application of a tag profile was described by (Aletras et al., 2004):

$$\begin{aligned} I(x,y,t) &= I_{FID}(x,y,t) + I_{SINE}(x,y,t) \\ &= A(x,y)\left[1 + \left(\cos^2\phi - 1\right)\exp\left(-t/T_1\right) + \sin^2\phi\cos\Phi(x,y)\exp\left(-t/T_1\right)\right] \end{aligned} \tag{4.12}$$

where (x, y) is the spatial point; t is the time from tag application to image acquisition; $I_{FID}(x,y,t)$ and $I_{SINE}(x,y,t)$ are the unmodulated and spatially modulated magnetization at time t respectively; $A(x,y)$ represents the non-tagged MR image; $\Phi(x,y)$ is the phase at the spatial point (x,y), φ and T_1 are the tagging flip angle of the RF pulses and the relaxation time constant respectively. A CSPAMM image is a subtraction of two 1-1 SPAMM images, one of which has the tag lines inverted, and hence, a CSPAMM image is:

$$I(x,y,t) = 2A(x,y)\left(\sin^2\varphi\cos\Phi(x,y)\exp\left(-t/T_1\right)\right). \tag{4.13}$$

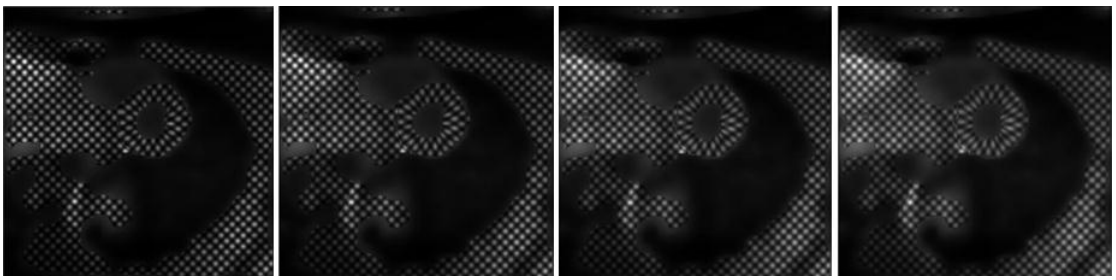

(a) (b) (c) (d)

Figure 4-9. Simulated images. (a)-(d) Frame 4, 6, 8 and 10 of the simulated images

A simple ring with uniform image intensity is usually used to represent the LV in synthetic tagged images (Chen et al., 2010; Wang and Amini, 2010; Cordero-Grande et al., 2011). However, this does not provide good simulation of a real MR tagged image since it ignores $A(x,y)$ and increases the image discontinuity. In order to have realistic simulated tagged images, the $A(x,y)$ was obtained using a cardiac MR image. The simulated imaging parameters were: $\varphi = 40^\circ$, $T_1 = 850$ ms. Tag spacing was 7.6 pixels on the 256 x 256 pixels image. Twenty images were simulated during one cardiac cycle. The displacement field during the cardiac contraction was modeled as a linear function of time t. Frames 4, 6, 8 and 10 of the simulated images are shown in Figure 4-9.

4.2.2 Adaptive Windowed Harmonic Phase

4.2.2.1 Instantaneous Frequency Detection

The 2D-GWT (Weng et al., 2009) is defined as follows:

$$W(s,\omega,a,b) = \int_{-\infty}^{\infty}\int_{-\infty}^{\infty} I(x,y)\Psi^*_{s,\omega}(x,y,a,b)dxdy \quad (4.14)$$

,

$$\Psi(x,y) = \frac{1}{\sqrt[4]{\pi}}\sqrt{\frac{2\pi}{\gamma}}\exp\left[-\frac{(2\pi/\gamma)^2(x^2+y^2)}{2} + j2\pi(x+y)\right] \quad (4.15)$$

where $\psi_{s,\theta}(x,y)$ is a two dimensional Gabor mother wavelet, $*$ indicates the complex conjugate, $\gamma = \pi\sqrt{2/In2}$ $\gamma = \pi\sqrt{2/\mathrm{In}2}$ and j is the imaginary unit. A series of analyzing wavelets, namely the 'daughter wavelets' are built up by shifting, scaling and rotating the mother wavelet as follows:

$$\Psi_{s,\omega}(x,y,a,b) = \frac{1}{\sqrt[4]{\pi}}\sqrt{\frac{2\pi}{\gamma}}\exp\left\{-\frac{(2\pi/\gamma)^2\left[(x-a)^2+(y-b)^2\right]}{2s^2}\right\}\exp\left\{j2\pi\frac{(x-a)\cos\omega+(y-b)\sin\omega}{s}\right\}$$

(4.16)

where s and θ are the tag spacing and the angle modulations respectively, (a,b) is the shifting parameter related to the position. The sand $\omega\theta$were chosen to be

$$s \in [0.5,1.5] \cdot s_T, \quad \omega \in [\omega_T - \pi/12, \omega_T + \pi/12] \tag{4.17}$$

where s_T and ω_T are the tag spacing and tag orientation of the undeformed tagged MR images respectively.

The result of 2D-GWT is a four dimensional array related to two position parameters a and b, tag spacing s and tag angle ω. At position (a,b), the modulus $|W(s,\omega,a,b)|$ reaches its maximum at $s = T$ and $\omega = \alpha$, where T represents local tag spacing and α represents local tag orientation. The peak of the 2D-GWT is defined as the location where the modulus $|W(s,\omega,a,b)|$ reaches its local maximum along both the scale direction s and rotation direction ω. After peak of the 2D-GWT is detected, the corresponding tag spacing and angle related to the instantaneous frequency are obtained. The instantaneous tag spatial period T_x and T_y are calculated as:

$$\begin{pmatrix} T_x \\ T_y \end{pmatrix} = \begin{pmatrix} \dfrac{T}{\cos\alpha} \\ \dfrac{T}{\sin\alpha} \end{pmatrix}. \tag{4.18}$$

4.2.2.2 Adaptive Windowed Fourier Transform

According to Heisenberg uncertainty theory, the spatial resolution Δx and the frequency resolution Δf satisfy the following equation:

$$\Delta x \Delta f \geq 1/4\pi \tag{4.19}$$

where $\Delta x \Delta f$ is called the Heisenberg box. An increase in the spatial resolution will cause a decline in the frequency resolution. By using adaptive Gaussian window according to the local signals, we can achieve an appropriate resolution in both spatial and frequency domains. AWFT is an extension of the conventional windowed Fourier transform. It is advantageous for analyzing non-stationary spatial or time signals by varying the window widths. 2D-AWFT is defined as follows:

$$S(\mu,\nu,\xi,\eta)=\int_{-\infty}^{\infty}\int_{-\infty}^{\infty} I(x,y)\exp(-j\xi x)\exp(-j\eta y)g\delta(x,y)dxdy, \tag{4.20}$$

$$g\delta(x,y)=\left|\delta_x\delta_y\right|^{-1} g\left(\frac{x-\mu}{\delta_x},\frac{y-\nu}{\delta_y}\right),\delta_x,\delta_y>0, \tag{4.21}$$

$$g(x,y)=\frac{1}{2\pi}\exp\left(-\frac{x^2+y^2}{2}\right) \tag{4.22}$$

where $g\delta(x,y)$ is a two dimensional multi-scale Gaussian function with dilation factors δ_x,δ_y corresponding to the widths of the Gaussian window, and shift factors μ,ν corresponding to the center of the Gaussian window, $g(x,y)$ is a two dimensional Gaussian function, $S(\mu,\nu,\xi,\eta)$ can be considered as a two-dimensional Fourier transform of a section of the tag pattern selected by the Gaussian window.

4.2.2.3 Widths of the Gaussian Window

The length of the local area in which the signal remains stationary is called the local stationary length of the signal (Zhong and Zeng, 2007). In order to get a complete extraction of the first harmonic of the cardiac tag pattern and avoid adjacent harmonic overlap, the Gaussian window widths should be matched with the local stationary length of the tag pattern. Local frequencies of tag pattern are altered due to the cardiac

motion in MR images. The window widths are determined according to the instantaneous frequencies of the non-stationary tag pattern. The widths of the Gaussian window δ_x, δ_y are defined as the full widths at half maximum as follows:

$$\begin{pmatrix} \delta_x \\ \delta_y \end{pmatrix} = \begin{pmatrix} \frac{T_x}{2\sqrt{2In2}} \\ \frac{T_y}{2\sqrt{2In2}} \end{pmatrix}. \tag{4.23}$$

4.2.2.4 Phase Extraction

Two dimensional Fourier transform of an image $I(x,y)$ can be expressed as:

$$I(\xi,\eta) = \int_{-\infty}^{\infty}\int_{-\infty}^{\infty} I(x,y)\exp(-j\xi x)\exp(-j\eta y)dxdy. \tag{4.24}$$

The relationship between the AWFT and Fourier transform can be obtained as:

$$\begin{aligned} \int_{-\infty}^{\infty}\int_{-\infty}^{\infty} S(\mu,\nu,\xi,\eta)d\mu d\nu &= \int_{-\infty}^{\infty}\int_{-\infty}^{\infty}\int_{-\infty}^{\infty}\int_{-\infty}^{\infty} I(x,y)\exp(-j\xi x)\exp(-j\eta y)g\delta^{\mu,\nu}(x,y)dxdyd\mu d\nu \\ &= \int_{-\infty}^{\infty}\int_{-\infty}^{\infty} I(x,y)\exp(-j\xi x)\exp(-j\eta y)\left\{\int_{-\infty}^{\infty}\int_{-\infty}^{\infty} g\delta^{\mu,\nu}(x,y)d\mu d\nu\right\}dxdy. \\ &= I(\xi,\eta) \end{aligned} \tag{4.25}$$

It means that the sum of the spectra obtained by 2D-AWFT is equal to the spectra obtained by the Fourier transform. The global first harmonic can be obtained by summing up the first harmonics of each local tag pattern:

$$I(\xi_0,\eta_0) = \int_{-\infty}^{\infty}\int_{-\infty}^{\infty} S(\mu,\nu,\xi_0,\eta_0)d\mu d\nu \tag{4.26}$$

where the subscript 0 in (ξ_0,η_0) represents the first harmonic peak of each local tag pattern. The phase images can be calculated by performing inverse Fourier transform on $I(\xi_0,\eta_0)$.

4.2.2.5 Performance Evaluation of AWHARP

Figure 4-10 shows the calculated instantaneous tag spatial period T_x and T_y for the left ventricle (LV) of the simulated images (frame 10).

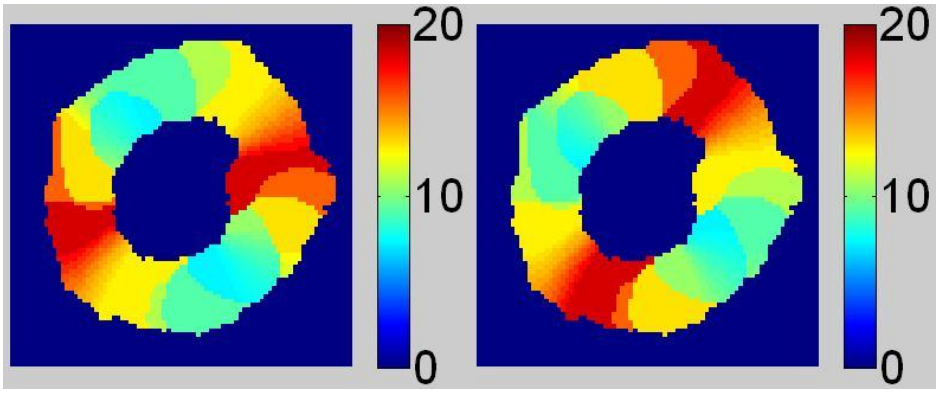

(a) (b)

Figure 4-10. Instantaneous tag spatial period. (a) In the x direction, (b) in the y direction. Unit: pixel

Since CSPAMM image is a subtraction of two SPAMM images, one of which has the tag lines inverted, I_{FID} in Equation 4.12 is absent for CSPAMM image (Fischer et al., 1993). Hence, spectral energy of CSPAMM image is concentrated around its first harmonic peaks. Low magnitude spectra surrounding the harmonic peaks of each Gaussian window can be filtered by thresholding. Since the magnitude of these noisy spectra is sufficiently smaller than that of the first harmonic peaks, the threshold value can be easily determined by inspection. For SPAMM images, the term I_{FID} in Equation 4.12 generates a central spectral peak in each local spectral domain, which interferes with the first harmonic peaks. I_{FID} can be estimated by averaging the image intensity over the Gaussian window since the sinusoidally modulated tag profile has zero mean intensity. I_{FID} can then be subtracted from the image to reduce the spectral interference due to the central spectral peak.

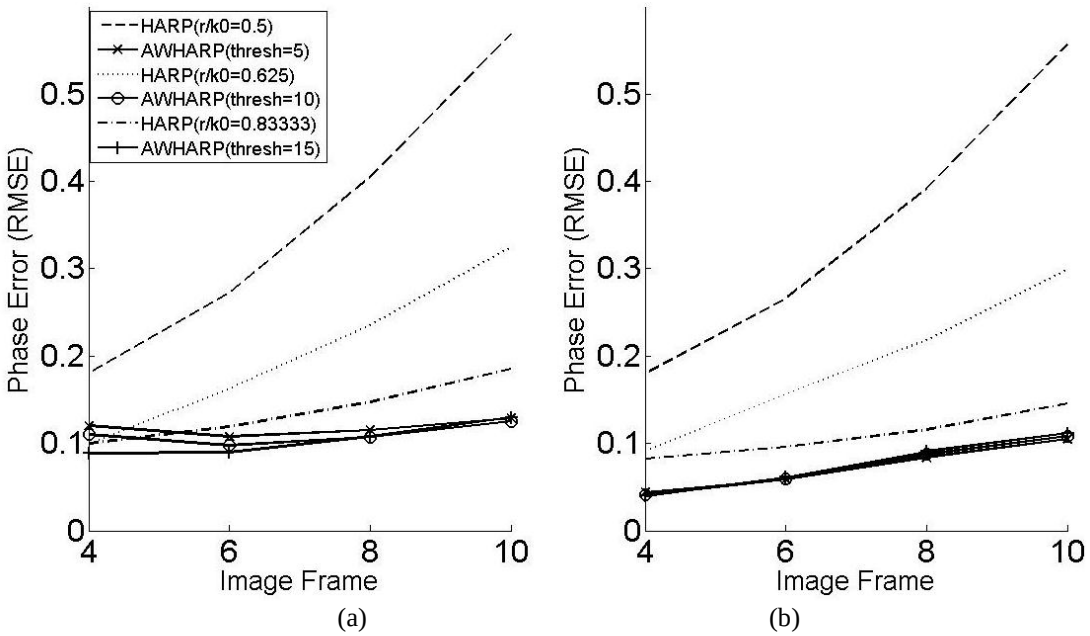

Figure 4-11. RMSE of phase images. (a) SPAMM, (b) CSPAMM

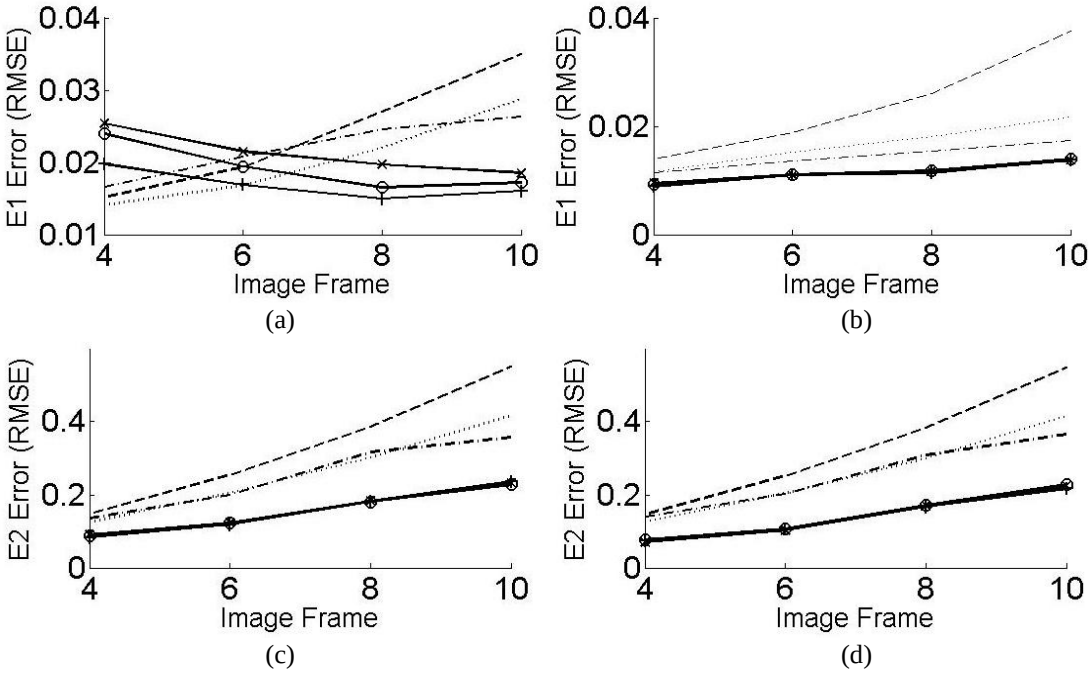

Figure 4-12. RMSE of strain images. (a) Minimum principle strain E1 of SPAMM images, (b) minimum principle strain E1 of CSPAMM images, (c) maximum principle strain E2 of SPAMM images, (d) maximum principle strain E2 of CSPAMM images

The HARP method was implemented for comparison. This implementation has been verified in our previous paper (Fu et al., 2011). Let r be the filter radius and k_0 be the tagging frequency, different values of r/k_0 have been used to extract the harmonic peaks in HARP. For comparison, different threshold values were used in AWHARP.

Minimum principle strain (E1) and maximum principle strain (E2) were calculated and analyzed. Root mean square errors (RMSE) of the phase and strain images were plotted in Figure 4-11 and Figure 4-12 respectively. The true strain and calculated strain images for frame 10 using both methods are shown in Figure 4-13.

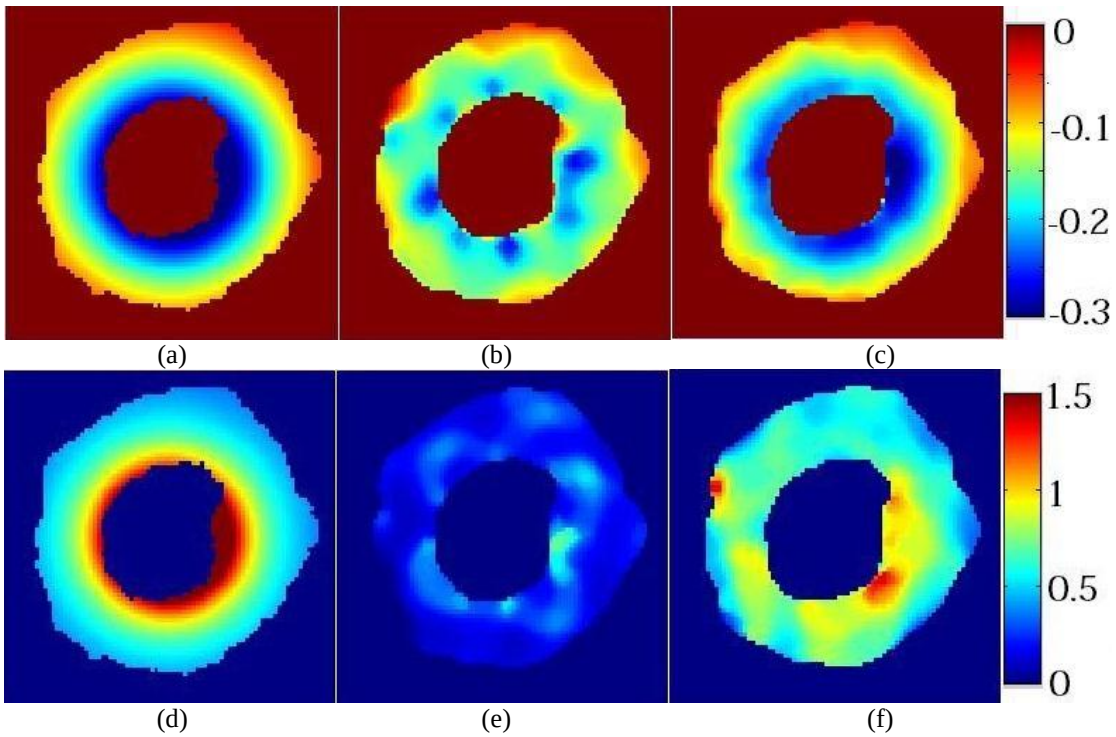

Figure 4-13. Strain images. (a) Ground truth of E1, (b) calculated E1 using HARP, (c) calculated E1 using AWHARP, (d) ground truth of E2, (e) calculated E2 using HARP, (f) calculated E2 using AWHARP

Tagged MR images are often contaminated with noise due to issues such as magnetic field inhomogeneity of the MR systems. Different levels of noise were added to simulated images to evaluate the performance of our method against noise. Phase error images using simulated images with SNR equal to 20dB and 10 dB are shown in Figure 4-14. The phase error calculated using AWHARP is smaller than that calculated using HARP especially at endocardium where the tag line deformation is large. Phase reconstruction RMSE is shown in Table 4-1.

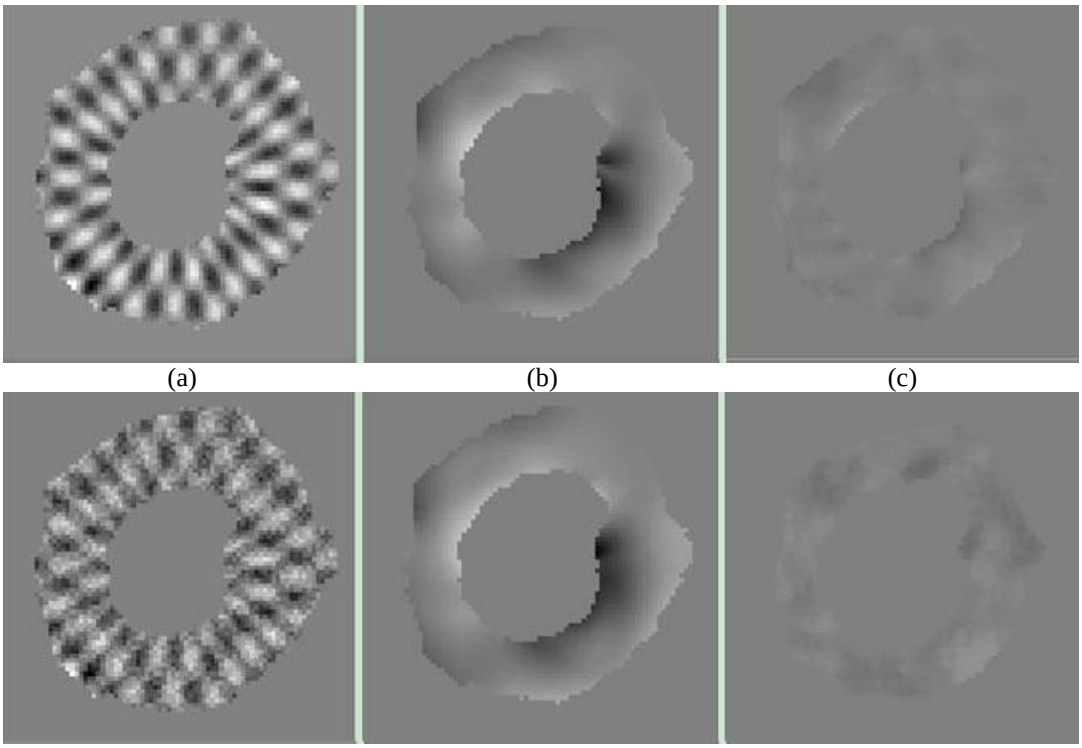

(a) (b) (c)

(d) (e) (f)

Figure 4-14. Phase error images. (a) Simulated tagged image with SNR of 20dB, (b) phase error image calculated using HARP with SNR of 20dB, (c) phase error image calculated using AWHARP with SNR of 20dB, (d) simulated tagged image with SNR of 10dB, (e) phase error image calculated using HARP with SNR of 10dB, (f) phase error image calculated using AWHARP with SNR of 10dB

Table 4-1. Phase reconstruction RSME

SNR(dB)	Infinite	20	10
HARP	0.55	0.55	0.57
AWHARP	0.12	0.13	0.21

4.2.3 Analysis of Hypertrophic Cardiomyopathy Patient Data

Hypertrophic Cardiomyopathy (HCM) is a heart disease where the heart muscle thickens abnormally. This thickening can occur in different parts of the heart, but usually occurs in the LV which is the main pumping chamber of the heart. CSPAMM images were acquired on a 1.5-T SIEMENS Avanto scanner for three normal hearts and three hearts with HCM. The imaging parameters were: flip angle, 20°; tag orientation, 45°; tagging spacing, 6mm; TE, 1.27msec; TR, 36.2msec; slice thickness, 7mm; FOV, 30×30 cm. Twenty eight tagged images were obtained for a whole

cardiac cycle. The tagged MR images of a normal heart and a heart with HCM are shown in Figure 4-15. The tag line deformation of heart with HCM is smaller than that of normal heart which is apparent from Figure 4-15.

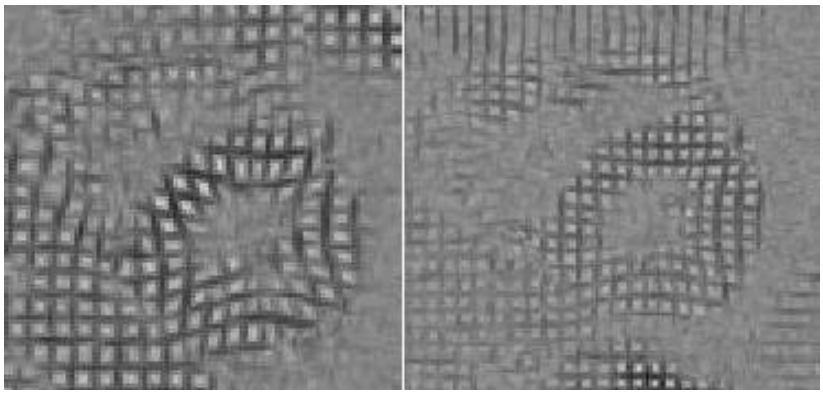

(a) (b)

Figure 4-15. MR tagged images of heart. (a) Normal heart, (b) heart with HCM

4.2.3.1 Tag Line Tracking

A series of MR images was acquired on a 1.5-T SIEMENS Avanto scanner. Twenty eight tagged images were obtained within a single breath hold. The imaging parameters were: flip angle, 15°; tag orientation, 45°; tag spacing, 7mm; TE, 1.49msec; TR, 28.9msec; slice thickness, 8mm; FOV, 24×24 cm. The publicly available datasets were downloaded from http://www.creatis.insa-lyon.fr/inTag/index.html. Image frame 10 was processed and tag line tracking differences using the two methods are shown in Figure 4-16. Visually, it is difficult to tell which one is more accurate in tracking the tag lines. Since tag lines are defined to be the dark lines which represent the sinusoidal wave trough of the sinusoidally modulated magnetization, pixel intensity of the tag lines should be smaller than that of their surrounding pixels. The mean image intensities of the tracked tag lines were calculated as 101 and 107 using AWHARP and HARP respectively. Hence, AWHARP method is more accurate in tracking the tag lines than the HARP method.

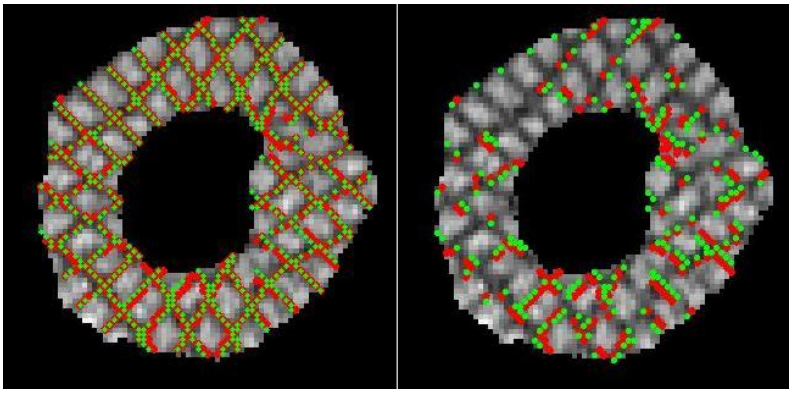

(a) (b)

Figure 4-16. Tag line tracking. (a) Tracking using both methods, (b) tracking differences between the two methods (green: AWHARP, red: HARP)

4.2.3.2 Strain Analysis

Cardiac strains are quantified to analyze the local myocardial function using HARP and AWHARP. The filter radius for the HARP method was chosen to be half the tag frequency. Figure 4-17 shows the calculated LV strain curves for a normal heart and a heart with HCM. In early systolic state (frame 1-4) and end diastolic state (frame 14-20), similar strain values were calculated using HARP and AWHARP. However, in the end systolic state (frame 4-13), where the heart deformation was large, different strain values were calculated using the two methods. AWHARP produced bigger strain values due to its good ability with large tag line deformations. Radial strain calculated using AWHARP revealed the decrease of strain values in pathological heart, which could not be detected using HARP. Similarly, circumferential strain differences between the normal heart and the pathological heart were more obvious with AWHARP than HARP. For illustration, strain images of frames 4, 6, 8, 10, 12 of a normal heart are shown in Figure 4-18. Strain differences using the two methods were highlighted using rectangles and arrows.

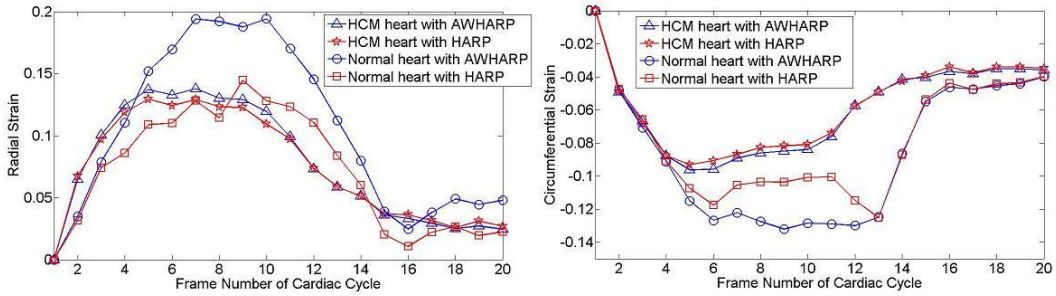

(a) (b)

Figure 4-17. Strain values of a normal heart and a heart with HCM. (a) Radial strain, (b) circumferential strain

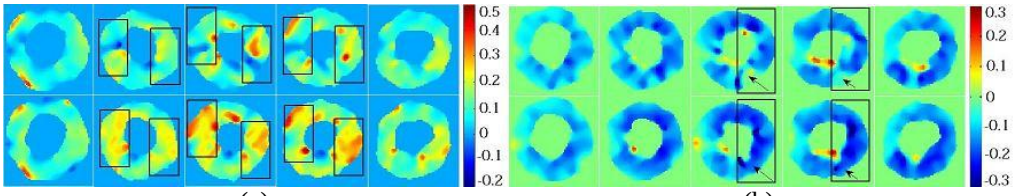

(a) (b)

Figure 4-18. Strain images of frames 4, 6, 8, 10, 12 of a normal heart. (a) Radial strain, top: HARP, bottom: AWHARP, (b) circumferential strain, top: HARP, bottom: AWHARP

Regional cardiac strains were analyzed within four ventricular segments, defined in Figure 4-19. The septal segment was defined as any septal myocardium lying between the anterior and inferior insertions of the right ventricle onto the LV. The anterior, lateral and inferior segments were defined clockwise as the first one-third, second one-third, and last one-third of the remaining myocardial wall.

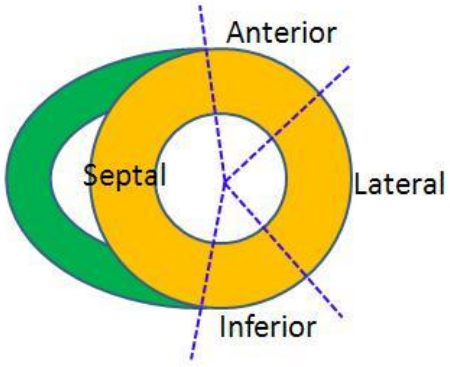

Figure 4-19. Septal, Anterior, Lateral, Inferior segments of the LV. Yellow part is the LV, green part is the right ventricle

Table 4-2. Decomposition of LV Strains in the end-systolic state. Left values correspond to HARP, whereas right values correspond to AWHARP

	Circumferential Strain (%)		Radial Strain(%)	
	Normal (N=3)	HCM (N=3)	Normal (N=3)	HCM (N=3)
Septal	-11.3±3.5/-10.6±3.9	-5.6±2.7/-5.6±3.0	9.9±4.8/17.7±7.5	7.5±3.9/7.6±3.2
Anterior	-13.2±5.2/-14.5±5.3	-9.1±4.7/-10.0±4.2	15.7±6.0/23.8±5.1	10.9±6.3/11.4±6.5
Lateral	-12.2±4.9/-17.6±3.9	-11.2±4.9/-11.5±5.0	14.0±8.0/29.5±5.4	16.4±8.0/19.1±7.1
Inferior	-11.6±3.6/-11.9±3.8	-7.2±3.1/-6.9±3.9	13.5±5.0/15.4±6.6	11.6±3.8/12.1±3.9

Averaged strains in the end-systolic state within the four segments are shown in Table 4-2 for three normal hearts and three hearts with HCM using HARP and AWHARP. The strains of anterior, lateral and inferior wall segments were slightly bigger than that of septal wall segment, which agreed well with Ennis DB et al's paper (Ennis et al., 2003). Compared with normal hearts, the average strain values of pathological hearts calculated using AWHARP decreased by 37.7% and 41.8% for circumferential strain and radial strain respectively, while the average strain values of pathological hearts calculated using HARP decreased only by 21.7% and 12.6% for circumferential strain and radial strain respectively.

4.3 Discussions and Conclusion

The enhanced HARP image processing method performs motion tracking by measuring the phase shift of soft tissue during indentation. One limitation of the enhanced HARP motion tracking method is that it only applies to situation where smooth deformation presents. Validation of the HARP strain calculation is performed on a series of simulated tagged images. Strong agreement between the calculated and true strains is observed. The good noise reduction performance is due to the band-pass filter which also serves as a noise filter. The radius of the band-pass filter is important.

Large radius may introduce unnecessary noise while small radius may suppress the actual deformation signal. Optimal radius selection is proposed in Arts et al. (2010).

Cardiac strain quantification can provide information about LV dysfunctions and myocardial diseases. Cardiac strain values of HCM patients are reduced significantly in the end systolic state compared with that of healthy subjects. AWHARP can help clinicians to detect left ventricle (LV) abnormalities with accurate cardiac strain analysis. Since the deformed tag spacing and orientation vary spatially, a local representation of the image spectra could facilitate the generation of more accurate harmonic phase images. We introduced a criterion for the choice of adaptive Gaussian window widths. Local spatial frequencies of the tag image were calculated using 2D-GWT. The Gaussian window widths were then determined according to the local spatial period that matches the local stationary length of the signal. The global harmonic peaks were obtained by summing up the first harmonic peaks in each Gaussian-windowed tagged image. Results from our experiments with simulated tagged images and MR images show that there is an improvement in performance with our method over the HARP method. AWHARP can also be applied to other spectrum based methods (Chen et al., 2010; Wang and Amini, 2010) since AWHARP improves the accuracy of the underlying harmonic phase image.

In HARP method, the choice of the circular filter radius exhibits well-known tradeoffs between strain resolution and artifacts due to the use of a common filter for all spatial positions. The significant variation of phase and strain errors for different r/k_0 values in HARP is shown in Figure 4-11 and Figure 4-12. It is therefore difficult to choose an optimal filter radius for the HARP method. However, the performance of the

AWHARP method is less sensitive to the filtering threshold value which is apparent from Figure 4-11 and Figure 4-12. Due to the central spectral interference in SPAMM images, the performance of AWHARP on SPAMM images is slightly worse than that on CSPAMM images. Both AWHARP and HARP perform well against noise since the band-pass filters used to extract the harmonic phase also serve as noise filters. The phase and strain error calculated using AWHARP is smaller than that calculated using HARP (Figure 4-11 and Figure 4-12).

AWHARP can optimally extract the harmonic peaks due to the following reasons. Firstly, harmonic peaks extraction is achieved by summing up the filtered harmonic peaks in each local Fourier domain rather than using a common filter for all spatial positions. Secondly, with windowing, the local spectrum is not influenced by unrelated pixels that are outside the window. Thirdly, by setting the window widths according to local spatial period, the local spectra are concentrated and have few spectral smears over the frequency domain.

By using adaptive window length that matches the local tag pattern, the AWHARP method can provide optimal local spectrum representation and phase extraction. Our experimental results showed that the AWHARP method outperforms the HARP method especially for large tag deformations. In the early systolic state (frame 1-4) and the end diastolic state (frame 14-20), similar strain values were calculated using HARP and AWHARP (Figure 4-17). However, in the end systolic state (frame 4-13), when the heart deformation was large, the calculated strain values were different. AWHARP produced bigger strain values due to its good ability with large tag line deformations. Because heart muscles of HCM patients thicken abnormally, tag line

deformation of HCM patients is smaller than that of normal hearts. The average strain values of the patients with HCM calculated using HARP are 2.6% and 7.5% smaller than those calculated using AWHARP for circumferential strain and radial strain respectively, while the average strain values of healthy subjects calculated using HARP are 11.5% and 38.4% smaller than those calculated using AWHARP for circumferential strain and radial strain respectively (Table 4-2). Since AWHARP is advantageous for large tag line deformation, the strain value differences between HARP and AWHARP are larger for normal hearts than those of pathological hearts.

AWHARP is an accurate and efficient method for cardiac strain estimation from MR images. This new algorithm can help clinicians to detect LV dysfunctions and myocardial diseases with accurate cardiac strain analysis. Our simulated tagged images which are realistic could aid the development of new image processing algorithms for tagged MR imaging.

CHAPTER 5 ELASTICITY RECONSTRUCTION OF SOFT TISSUE

In MRE, the step beyond strain imaging is elasticity imaging which involves solving an inverse problem with the measured strain to determine the elasticity distribution of soft tissue. In Chapter 4, tagged MR images are processed to generate displacement field and strain images of deformed soft tissue. In this chapter, we focus on determining elasticity distribution of the soft tissue from the measured displacement field or strain images.

Various inverse methods (Barbone and Gokhale, 2004; Barbone and Oberai, 2007; Sette et al., 2011) have been proposed to estimate soft tissue elasticity distribution from measured displacement/strain images. A widely used inverse method is the optimization method (Moulton et al., 1995; Kauer et al., 2002; Erdemir et al., 2006; Kim et al., 2008; Liu et al., 2009). Finite element (FE) method is used to simulate soft tissue deformation. The residual between the simulated displacement field and the measured displacement field is minimized using the optimization method. This method approaches the solution through an iterative process. A uniform initial guess of the element stiffness is often used in the first iteration. Finite difference approximation is usually used to calculate the entries of the Jacobian matrix J (Schnur and Zabaras, 1992; Chen and Bicanic, 2000;). The entries of J are obtained by slightly perturbing the stiffness of each element separately, and then solving the forward FE analysis for each perturbation. Since the finite difference approximation method needs to perform forward FE analysis repeatedly, this method is

computationally expensive, particularly for FE model that has a large number of elements.

Another commonly used method is a FE-based direct inverse method (Zhu et al., 2003; Guo et al., 2008). In this method, the solution is obtained by minimizing an objective function defined as the sum of the square of the force residual norms at all nodes. Measured nodal displacement vector is directly applied to equilibrium equations at the element level. After global assembly in FE method, material stiffness vector can be expressed explicitly and calculated directly. This method is efficient since no forward FE analysis is needed. However, this method is sensitive to noise and is only applicable to linear elastic material. Soft biological tissue is a highly incompressible hyperelastic material (Chui et al., 2004; 2007; Nava et al., 2008). Mechanical behavior of hyperelastic material differs significantly from that of linear elastic material. It is important to develop a computationally efficient method which is applicable to hyperelastic material models.

In this chapter, we proposed a novel material parameter reconstruction method for hyperelastic material models. This method combines the advantages of the FE-based direct inverse method and the nonlinear optimization algorithm. In the optimization method, initial guess is important since a poor guess may result in much iteration for convergence or even non-convergence. The widely used uniform initial guess may not be the optimal initial guess. In our method, an estimation of the true material stiffness distribution is first determined using the FE-based direct inverse method. This estimation is then input to the Levenberg-Marquardt (LM) optimization algorithm as the initial guess. Final solution is obtained after the optimization process. In the

optimization method, a new algorithm is proposed for the calculation of Jacobian matrix. The repeated forward FE analysis is avoided using this algorithm. Neo-Hookean hyperelastic model is used to represent the biological soft tissue. Forward FE analysis is performed using Abaqus (ABAQUS Inc.). The execution of Abaqus in our implementation is controlled via customized Python scripts.

Section 5.1 describes the proposed inverse algorithm. In Section 5.2, the proposed algorithm is implemented, and verified with applications to solve 2D plane strain compression problems. In Section 5.3, the proposed method is used to determine the elasticity distribution of a human lower leg. This chapter concludes with a discussion on the efficiency of the proposed algorithm and its contributions in Section 5.4.

5.1 A Combined Inverse Algorithm

A novel elasticity imaging method is proposed by combining FE-based direct inverse method and nonlinear optimization algorithm. Instead of using a uniform material stiffness distribution as an initial guess, an estimation of the true material stiffness distribution calculated by FE-based direct inverse method is used. Since the initial guess is estimated and is relatively closer to the true material stiffness distribution, smaller number of iterations is required for convergence. Instead of relying on finite difference method for Jacobian calculation, direct calculation of Jacobian matrix is introduced to improve the computational efficiency.

5.1.1 Neo-Hookean Hyperelastic Model

Isotropic hyperelastic model is used to represent the nearly incompressible biological soft tissue. Hyperelastic materials may be described in terms of 'strain energy potential' which defines the strain energy stored in the material per unit of reference volume as a function of the strain at that point in the material. Deformation gradient is defined by

$$\mathrm{F} = \frac{\partial x}{\partial X} = I + \frac{\partial u}{\partial X}, \tag{5.1}$$

where X is a material point in the reference configuration, x is the current position of the point, and u is the displacement. Both x and u are a function of time. The implementation of Neo-Hookean model in Abaqus is given by

$$\mathrm{U} = C(\overline{I}_1 - 3) + \frac{1}{D}(J-1)^2, \tag{5.2}$$

where U is the strain energy per unit of reference volume, C and D are material parameters. $\overline{I}_1$ and J are the strain invariants of the deviatoric left Cauchy-Green deformation tensor which is defined by

$$\overline{B} = \overline{F} \cdot \overline{F}^T, \tag{5.3}$$

where $\overline{F} = J^{-\frac{1}{3}}F$. The material Jacobian is given by

$$\begin{aligned} E_{ijkl} = {} & \frac{2}{J}C\left(\frac{1}{2}(\delta_{ik}\overline{B}_{jl} + \overline{B}_{ik}\delta_{jl} + \delta_{il}\overline{B}_{jk} + \overline{B}_{il}\delta_{jk}) - \frac{2}{3}\delta_{ij}\overline{B}_{kl} - \frac{2}{3}\overline{B}_{ij}\delta_{kl}\right. \\ & \left. + \frac{2}{9}\delta_{ij}\delta_{kl}\overline{B}_{mm}\right) + \frac{2}{D}(2J-1)\delta_{ij}\delta_{kl}. \end{aligned} \tag{5.4}$$

5.1.2 Material Stiffness Estimation

The continuum is first discretized into a number of elements and each material parameter is an unknown variable. The displacement within an element can be approximated by

$$\{u(x)\} = [N(x)]\{u^e\}, \tag{5.5}$$

where $\{u^e\}$ is the element nodal displacement vector, $N(x)$ is the shape function matrix. Strain tensor is calculated using

$$\varepsilon(x) = [L]\cdot[N(x)]\{u^e\} = [B]\{u^e\}, \tag{5.6}$$

where $[L]$ is a differential operation matrix; $[B]$ is the strain matrix. D represents the soft tissue compressibility and is assumed to be constant over the entire domain for simplification. The left Cauchy-Green deformation tensor is a function of strain, therefore, the material tangential elasticity matrix can be written as

$$[E_T] = C[f_1(\varepsilon)] + \frac{1}{D}[f_2(\varepsilon)]. \tag{5.7}$$

The element tangential stiffness matrix can be expressed as

$$\begin{aligned}[\mathrm{K}_{\mathrm{T}}^{\mathrm{e}}(C^e)] &= \int_{\Omega^e}[B]^T[E_T][B]d\Omega^e \\ &= C^e\int_{\Omega^e}[B]^T[f_1(\varepsilon)][B]d\Omega^e + \frac{1}{D}\int_{\Omega^e}[B]^T[f_2(\varepsilon)][B]d\Omega^e, \\ &= C^e[\overline{K_1^e}] + \frac{1}{D}[\overline{K_2^e}]\end{aligned} \tag{5.8}$$

where $\overline{K_1^e}$ and $\overline{K_2^e}$ are the respective reference element tangential stiffness matrices associated with a unit material parameters. C^e is the material parameter of the element. The element internal force vector is

$$\{\mathrm{f}^{\mathrm{e}}(e)\} \approx C^e[\overline{K_1^e}]\{u^e\} + \frac{1}{D}[\overline{K_2^e}]\{u^e\} = C^e\{\overline{f_1^e}\} + \frac{1}{D}\{\overline{f_2^e}\}, \tag{5.9}$$

where $\{\overline{f_1^e}\}$ and $\{\overline{f_2^e}\}$ are the respective reference element internal force vectors associated with a unit material parameters.

Reduced Gauss integration and isoparametric coordinates mapping are used to calculate the integrations and element shape functions. The global force vector is obtained through an assembling process over the entire domain. Boundary conditions need to be incorporated during this assembling process. Similar to forward FE analysis, 'fixed' boundary degree of freedoms (DOF) are removed from the system equations. By defining an element assembly matrix $[H^e]$, the 'fixed' boundary DOFs can be eliminated in the inverse problem. Each DOF is assigned an index i, $i = 1,2...n_d$, where n_d is the total system DOF. For each element e, an $n_d * n_d^e$ element assembly matrix $[H^e]$ is defined, where n_d^e is the DOF of a single element. The entries of $[H^e]$ is $H_{ij}^e = 1$, if the *jth* DOF of the element is assigned the *ith* system DOF and not a 'fixed' boundary DOF. Otherwise, $H_{ij}^e = 0$. When constructing the global internal force vector, a material parameter selective vector $\{G^e\}$ needs to be defined. For the *ith* element, $\{G^{e_i}\}$ is defined as $G_j^{e_i} = \delta_{ij}$. After the DOFs corresponding to the 'fixed' displacement boundary are removed, the global internal force vector can be expressed as

$$\{\mathrm{F}\} = \sum_{all}[H^e]\{\overline{f_1}^e\}\{G^e\}\{C\} + \sum_{all}[\mathrm{H}^e]\{\overline{f_2}^e\}\{G^e\}\{\frac{1}{D}\} = \{\overline{F_1}\}\{C\} + \{\overline{F_2}\}\{\frac{1}{D}\}, \quad (5.10)$$

where $[H^e]$ is an element assembly mapping matrix, $\{G^e\}$ is a material parameter selective matrix, and $\{\overline{F_1}\}$ and $\{\overline{F_2}\}$ are global reference internal force vector associated with unit material parameters respectively. After assembling, the global equilibrium equation reads

$$[\overline{F_1}]\{C\}+[\overline{F_2}]\{\frac{1}{D}\}=\{P\}, \tag{5.11}$$

where $\{P\}$ is external force vector.

The dimension of vector $[\overline{F_1}]$ and $[\overline{F_2}]$ is $n_d \times n_e$. The dimensions of $\{C\}$ and $\{P\}$ are $n_e \times 1$ and $n_d \times 1$ respectively. In other words, there are n_d equations and n_e unknowns in the system. If $n_d < n_e$, there is not enough spatial information for material parameter reconstruction problem. In this situation, the solution is generally not unique. Extra displacement tracking points or a prior known material parameter is required to derive a unique solution. If $n_d = n_e$, which rarely happens, $\{C\}$ can be obtained directly by

$$\{C\}=[\overline{F_1}]^{-1}(\{P\}-\{\overline{F_2}\}\{\frac{1}{D}\}), \tag{5.12}$$

when $[\overline{F_1}]$ is non-singular. In most cases, $n_d > n_e$, by minimizing the global force residue, the solution can be given by

$$\{C\}=\{[\overline{F_1}]^T[\overline{F_1}]\}^{-1}[\overline{F_1}]^T(\{P\}-\{\overline{F_2}\}\{\frac{1}{D}\}), \tag{5.13}$$

when $[\overline{F_1}]^T[\overline{F_1}]$ is non-singular. If the matrix $[\overline{F_1}]^T[\overline{F_1}]$ is singular, the solution will not be unique. New displacement tracking points or remeshing of the FE model is required to solve this problem.

5.1.3 LM Optimization

In FE analysis, hyperelastic nonlinear problem is usually solved through an iterative procedure. Traction boundary condition is applied using an incremental method. The material tangential elasticity matrix varies in every incremental step due to the strain

dependency property of the hyperelastic model. Since the stiffness matrix in (8) is used to estimate the incrementally changing tangential stiffness matrix, the material parameter calculated by (13) is only an estimation of the true material stiffness distribution. This estimation then serves as the initial guess of the LM optimization algorithm to calculate the material stiffness distribution.

Unknown Neo-Hookean material parameters are determined by minimizing the least-square difference between the simulated nodal displacement field and the measured displacement field. The objective function can be expressed as

$$\mathrm{R}(C) = \sum_{j}^{n}((u_{1j} - \hat{u}_{1j})^2 + (u_{2j} - \hat{u}_{2j})^2), \tag{5.14}$$

Where C is the material parameter to be optimized, u_{1j} , u_{2j} are the measured displacement vectors in x and y direction respectively, $\hat{u}_{1j}$, $\hat{u}_{2j}$ are the simulated displacement vectors, and n is the total number of nodes in the system.

Finite difference approximation is usually used to calculate the Jacobian matrix J . The forward FE analysis has to be solved repeatedly by slightly perturbing one material parameter in each forward FE analysis. If there are N elements in the FE model, the forward FE analysis has to be solved N times to obtain the Jacobian matrix J . In order to improve the computational efficiency of the algorithm, we introduce a new algorithm to calculate the Jacobian matrix directly. Consider a FE model with linear material, the FE equilibrium equation reads

$$Ku = f \text{ , and thus } u = K^{-1} f \text{ .} \tag{5.15}$$

Taking the first derivatives of u with respect to C , we have

$$\{J_i\} = \{\frac{\partial u}{\partial C_i}\} = [\frac{\partial K^{-1}}{\partial C_i}]\{f\}$$
$$= -[K]^{-1}[\frac{\partial K}{\partial C_i}][K]^{-1}\{f\} \quad , \tag{5.16}$$
$$\approx -[K]^{-1}[H^e][\overline{K_1^i}][H^e]^T[K]^{-1}\{f\}$$

where i =1,2…N is the element number, C_i is the material parameter of ith element, K is the global stiffness matrix, f is the global nodal force vector, $[\overline{K_1^i}]$ is the derivative of element stiffness matrix with respect to the ith elemental material parameter, and $[H^e]$ is the element assembly mapping matrix.

$$[J] = [J_1, J_2, \cdots J_N]. \tag{5.17}$$

The Jacobian matrix J can be estimated directly by substituting the stiffness matrix K with tangential stiffness matrix K_T. Computational efficiency of the algorithm is greatly improved with this method.

5.2 Performance Evaluation

In order to evaluate the performance of the proposed algorithm, two experiments with different strain levels and inclusion geometries were performed with example models as shown in Figure 5-1 and Figure 5-4. Different levels of noise were added to the input displacement field to test the noise sensitivity of our method. Plain strain condition was assumed in both FE models.

5.2.1 Rectangular Inclusion under Small Strain Level

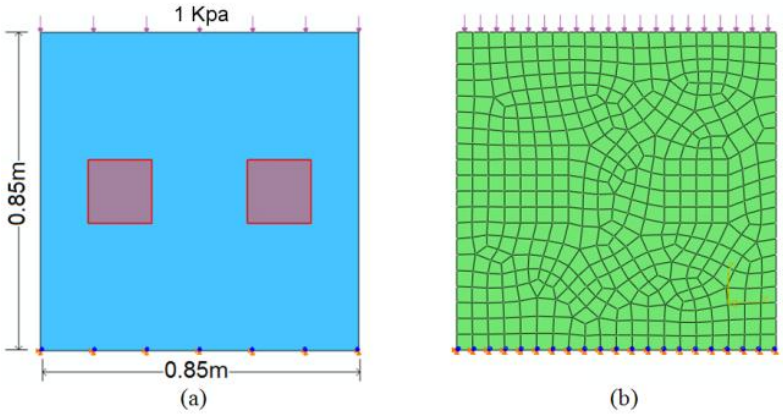

Figure 5-1. FE model. (a) Geometry and boundary conditions, (b) FE mesh

The two shadowed regions in the model represented the hard inclusions embedded within the softer homogeneous background. Neo-Hookean model was used in the analysis. In the forward FE analysis, material parameter D was set to 2E-7Pa^{-1} while material parameter C of the hard inclusions and soft background were set to 7E5Pa and 5E5Pa respectively. Uniform pressure load of 1kPa was applied onto the top surface. Both horizontal and vertical DOF of bottom surface were constrained. Each hard inclusion was divided into 16 elements and the entire domain was divided into 446 elements with 487 nodes. Quadrilateral element type CPE4R was used throughout the domain. Both material nonlinearity and geometric nonlinearity were considered in a static step.

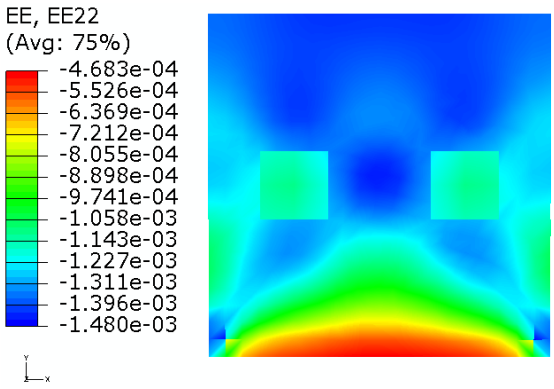

Figure 5-2. Contours of the normal strain in the vertical direction

In order to examine the numerical consistency of the proposed algorithm, the nodal displacement field calculated in the forward FE analysis was used for elasticity reconstruction. Simulation was performed under small strain level. Figure 5-2 shows the contour of the vertical normal strain without mesh on the deformed shape.

An estimation of the material stiffness distribution was first calculated using the method described in section 5.2. Final solution was obtained after LM optimization with this estimation as the initial guess. Results including 3D and side elevations of the material stiffness distribution are shown in Figure 5-3.

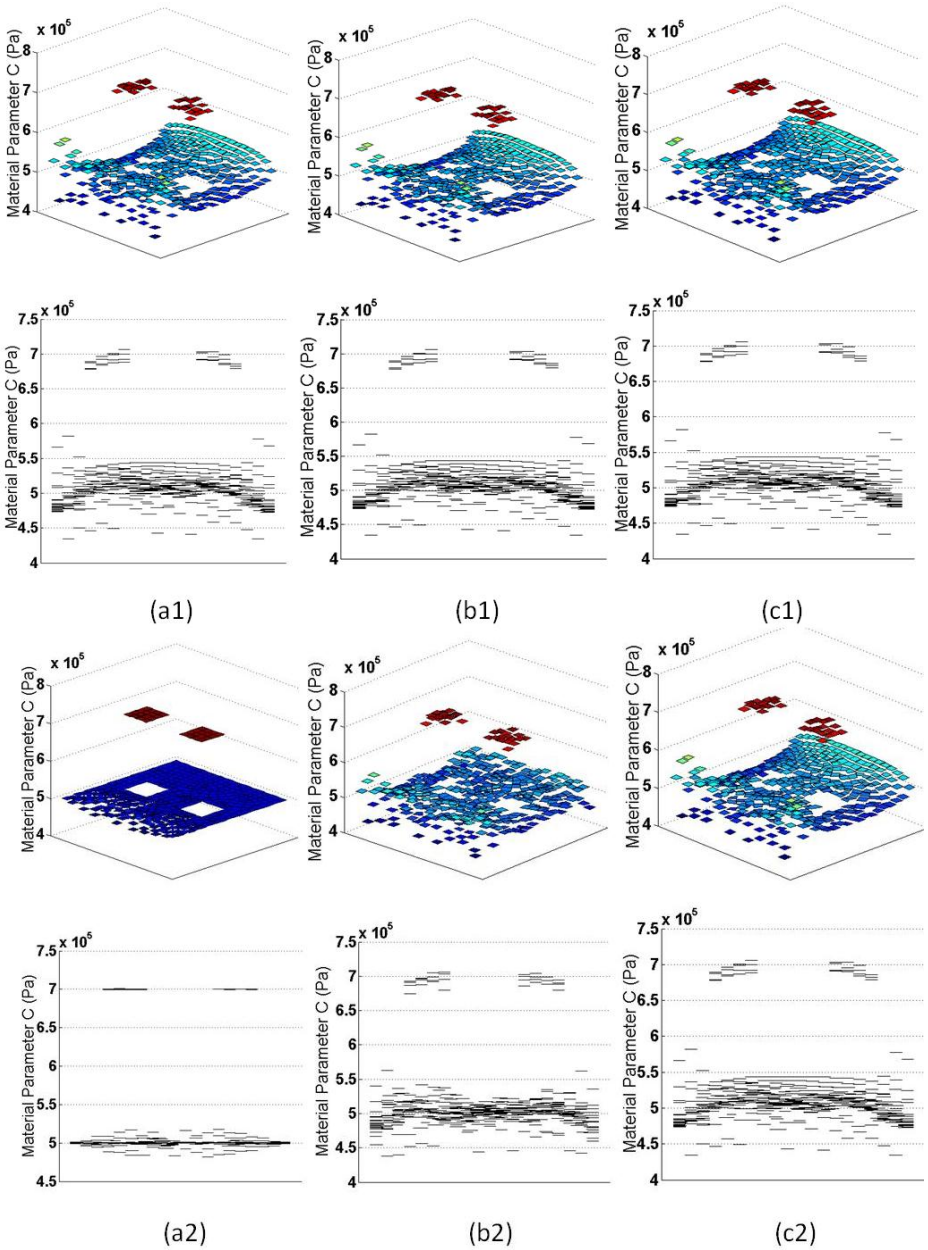

Figure 5-3. Reconstruction results. (a1) Estimated parameters (initial guess) with exact displacement data, (a2) final parameters with exact displacement data, (b1) estimated parameters (initial guess) with $\pm 1\%$ noise added to exact displacement data, (b2) final parameters (initial guess) with $\pm 1\%$ noise added to exact displacement data, (c1) estimated parameters (initial guess) with $\pm 3\%$ noise added to exact displacement data, (c2) final parameters with $\pm 3\%$ noise added to exact displacement data

The proposed algorithm recovered the exact material stiffness distribution using the exact displacement field. The error in the final solution will eventually become negligible with a harsher convergence condition. In practice, the available displacement field data always suffers from a certain level of noise. In order to evaluate the noise sensitivity of the algorithm, random noise was added to all the

component of the exact displacement field. The noise was defined as $(u_{input}/u_{exact} - 1)$, where u_{input} was the noise-impaired data. Displacement field with random noise of level $\pm 1\%$ and $\pm 3\%$ were tested and convergence occurs within an average error of 2.32% and 3.26% of the known parameters respectively. Objective cost and relative error of the reconstructed material parameters are shown in Table 5-1. Compared to the initial estimation, better material reconstruction was obtained after the LM optimization. For reconstruction using data with $\pm 3\%$ noise, the final solution was the same as that of the initial guess. In this case, the optimization procedure did not improve upon the initial guess due to the noise.

Table 5-1. Sensitivity study result when different level of noise is added

Condition	Initial guess				Final convergence			
	Objective Cost (R)	Relative error in stiffness (%)			Objective Cost (R)	Relative error in stiffness (%)		
		Min	Mean	Max		Min	Mean	Max
Exact data with no noise	5.07e-6	7.21e-3	3.26	16.42	1.37e-11	2.43e-5	0.29	3.60
Exact data with ±1% noise	8.52e-6	7.21e-3	3.26	16.42	3.40e-6	0.01	2.32	12.56
Exact data with ±3% noise	3.49e-5	7.21e-3	3.26	16.42	3.49e-5	7.21e-3	3.26	16.42

5.2.2 Circular Inclusion under Large Strain Level

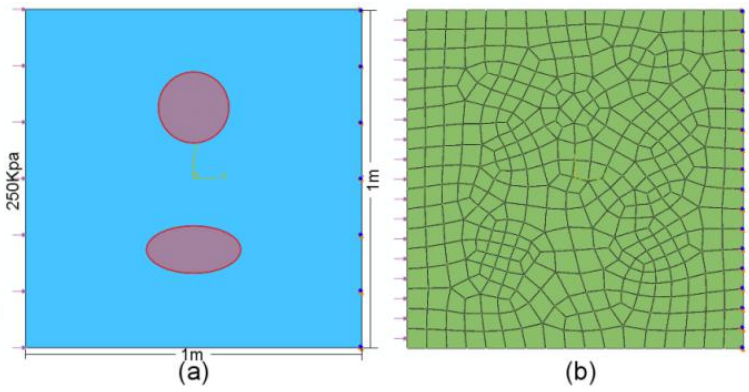

Figure 5-4. FE model. (a) Geometry and boundary conditions, (b) FE mesh

A circular and ellipsoidal inclusion was modeled with material parameter C set to be 7E5Pa and 5E5Pa respectively. Material parameter C of the soft background was 3E5Pa. Material parameter D was chosen to be 2E-7Pa^{-1} Uniform pressure load of 200kPa was applied onto the left surface. Both horizontal and vertical DOF of the right surface were constrained. The entire domain was divided into 388 elements with 423 nodes. Quadrilateral element type CPE4R was used throughout the domain. Both material nonlinearity and geometric nonlinearity were considered in a static step. The model reached a maximum normal strain level of 12%. Figure 5-5 shows the contour of the strain in the horizontal direction on the deformed shape.

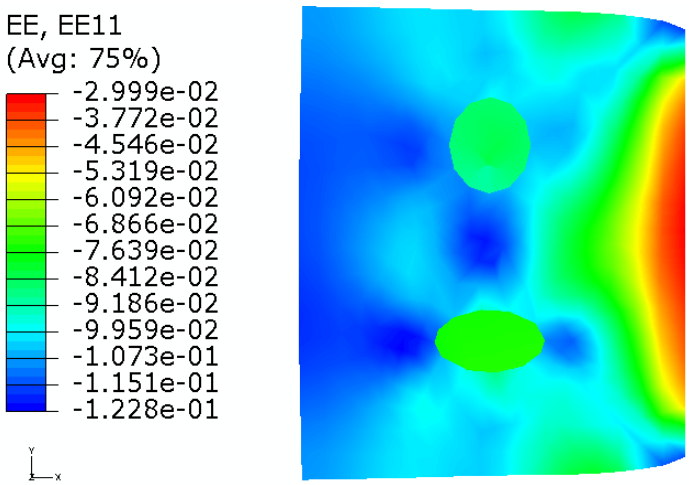

Figure 5-5. Contour of the normal strain in the horizontal direction

The proposed algorithm recovered the exact material stiffness distribution using the exact displacement field. Displacement data with random noise of $\pm 0.5\%$ was tested. Final stiffness distribution was obtained after the LM optimization. Results including 3D and side elevations of the material stiffness distribution are shown in Figure 5-6. Objective cost and relative error of the reconstructed material parameters are shown in Table 5-2. The result showed that the proposed algorithm performed well in large strain level.

Table 5-2. Sensitivity study result when different level of noise is added

Condition	Initial guess				Final convergence			
	Objective Cost (R)	Relative error in stiffness (%)			Objective Cost (R)	Relative error in stiffness (%)		
		Min	Mean	Max		Min	Mean	Max
Exact data with no noise	1.74e-2	4.76e-2	26.35	108.13	5.29e-13	6.78e-6	2.95e-3	2.03e-2
Exact data with $\pm 0.5\%$ noise	2.92e-2	0.91	31.57	144.91	0.56e-5	0.14e-2	9.19	48.66

5.2.3 Computational Time

The proposed algorithm was implemented using Matlab while the FE problem was solved using Abaqus based on customized Python scripts. The code was run on a workstation with a 2.4GHz dual core Intel CPU and 2GB of main memory. For comparison, the two models in section 5.2.1 and 5.2.2 were performed using a pure optimization method with a uniform initial guess of 6E5Pa. Execution time of our method was compared to that of the pure optimization method under the same convergence condition. The result is shown in Table 5-3.

Table 5-3. Computational time, Method 1: Proposed method. Method 2: Pure Optimization method (uniform initial guess, finite difference to calculated Jacobian matrix)

Methods	Model in section 5.2.1		Model in section 5.2.2	
	Iteration Number	Execution time	Iteration Number	Execution time
Method 1	8	5min	6	3min
Method 2	16	>6 hours	10	>6 hours

The proposed method converged faster than that of the pure optimization method. This is because an estimated initial guess from our method is closer to the true solution than the uniform initial guess. Since Jacobian matrix is calculated directly, the execution time has been greatly reduced.

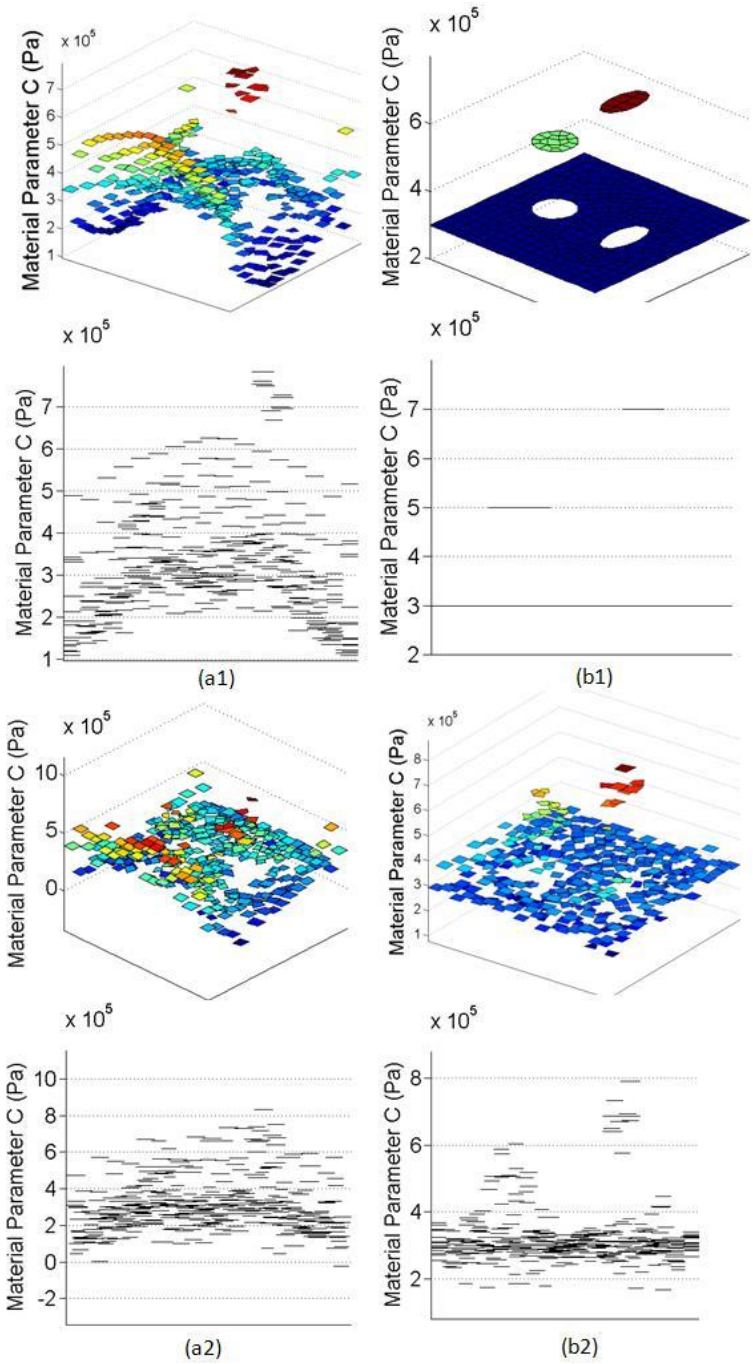

Figure 5-6. Reconstruction results. (a1) Estimated parameters (initial guess) with exact displacement data, (b1) final parameters with exact displacement data, (a2) estimated parameters (initial guess) with $\pm 0.5\%$ noise added to exact displacement data, (b2) final parameters with $\pm 0.5\%$ noise added to exact displacement data

5.3 Application on Human Lower Leg

The proposed method was tested using measured displacement field from MR tagged images. In the experiments, MR compatible actuator was designed to deform soft

tissue (Fu et al., 2011). A volunteer's lower leg was indented using a MR compatible actuator while the indentation force was recorded by a force sensor. A tagged MR image of human lower leg under indentation and boundary conditions for FE analysis are shown in Figure 5-7(a) and Figure 5-7(b) respectively. Displacement field was calculated from tagged MR image as illustrated in Figure 5-8(a) and Figure 5-8(b). The bones were modeled as rigid body. The entire domain was divided into 865 elements with 898 nodes. Triangular element type CPE3 and Quadrilateral element type CPE4R were used in the domain. Some nodal displacements were not considered in the optimization process since these nodal displacements were poorly measured. Only nodal displacements that were measured with high fidelity were the input of the proposed algorithm.

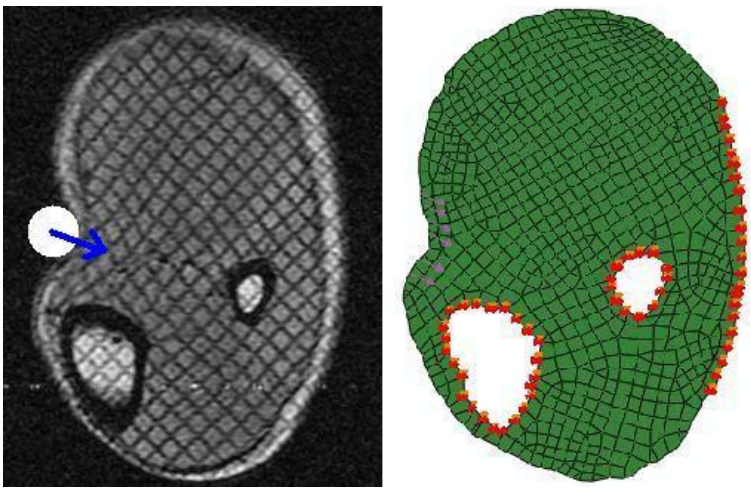

(a) (b)

Figure 5-7. Images of human lower leg. (a) MR image, white circle represents the indenter, blue arrow represents the indentation direction, (b) FE boundary conditions

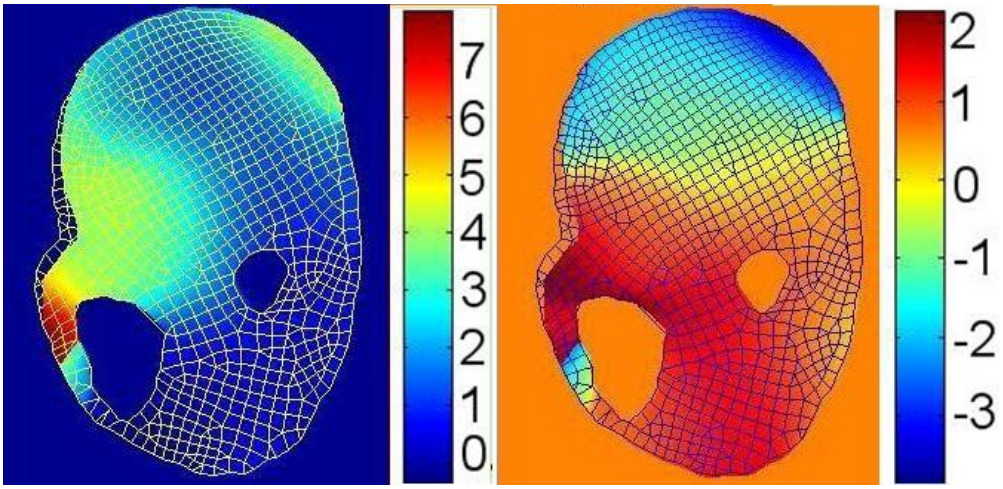

(a) (b)

Figure 5-8. Measured displacement field with FE mesh.(a) Horizontal displacement, (b) vertical displacement. Unit: mm

Figure 5-9 shows the elasticity distribution of the human lower leg at rest computed using our method. The elasticity was uniformly distributed over the leg domain except for the region indicated by rectangle. Since the deformation in the rectangle is hindered by the bone, the signal to noise ratio (SNR) of the measured displacement in this region is low. The large elasticity variation in this region is due to the low SNR. The average shear modulus of the leg muscle was 5.53kPa which was comparable to the results reported by Bensamoun SF et al (2006).

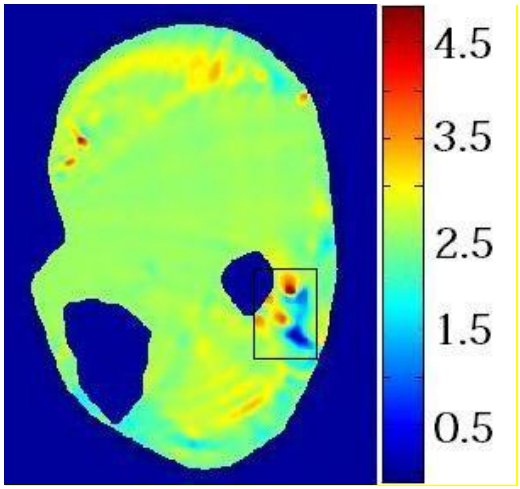

Figure 5-9. Elastography of human lower leg (Material Parameter: C, unit: kPa)

5.4 Discussions and Conclusion

In this chapter, a new material parameter reconstruction method is proposed for hyperelastic material models by combining the FE-based direct inverse method and nonlinear optimization method. The FE-based direct inverse method provides an estimation of the true material parameter distribution. This estimation serves as the initial guess of LM optimization algorithm. Direct calculation of Jacobian matrix is proposed to improve the computational efficiency of the LM optimization algorithm. Both numerical consistency and noise sensitivity of the proposed method are tested in its application to solve 2D plain strain problems. The proposed method was also verified using different inclusion shapes under different strain levels. Computer simulation results show that our method is computationally efficient, and is accurate for determining the material parameter distribution. The improved computational efficiency can be attributed to both estimated initial guess that is close to the true material parameter distribution and direct calculation of the Jacobian matrix.

If the exact displacement field obtained by forward FE analysis is used, material stiffness can be recovered totally after the optimization process. When the data were contaminated with random noise, exact solution to material parameter $\{C\}$ may not exist. For nonlinear material property, the system tangential matrix is strain-dependent. Since the calculation of strain involves differentiation of the measured displacement field, the differentiation may magnify the effect of the noise. The solution may diverge from the known solution due to the noise. It is important to introduce additional constraints to regularize the optimization process. Prior knowledge of the applied force is required to accurately compute the absolute elasticity distribution.

Although Neo-Hookean model has been used to model biological soft tissue in this algorithm, other polynomial hyperelastic models such as Mooney-Rivlin model can also be used. In this study, an example of pure compression is applied and plane strain condition is assumed for material reconstruction. Reduced integration is adopted. Since reduced integration may sometimes give poor results, full integration can be implemented if necessary. Although quadrilateral element is used throughout the FE model in this study, mixed element type meshing can be used in the proposed algorithm. Higher order elements can be used within the field of interest to improve the accuracy of FE model (Pathmanathan et al., 2009). For different element type, different number of integration points should be used accordingly. This algorithm can be readily extended to 3D by using 3D formulations of the system equilibrium equations.

Our experimental results on a human lower leg demonstrated that the proposed method is clinically viable. The material reconstruction algorithm was implemented using Matlab and Abaqus. There is a tight coupling between the Matlab codes and customized Abaqus subroutines written in Python scripts. The Matlab codes could be easily replaced with a more efficient programming language such as C or C++. The direct computation of the Jacobian matrix should be implemented in an efficient manner especially for FE models with a large number of elements. The Python scripting language is a convenient way of controlling the FE solution process in Abaqus. Nevertheless, FE solvers other than Abaqus could also be used.

CHAPTER 6 MODELING OF PORCINE LIVER TISSUE INDENTATION

Accurate modeling of biological tissue characteristics is important for medical simulation. High fidelity models are required in surgical simulators to accurately simulate realistic tool-tissue interactions incorporating haptic feedback and soft tissue deformation during surgery. Mechanical characterization of soft biological tissue such as liver tissue is highly beneficial in the management of liver diseases (Hawkes et al., 2003).

In order to measure the quantitative responses of soft tissues, numerous techniques including compression (Sakuma et al., 2003; Hu and Desai et al., 2004; Chui et al., 2004; Rosen et al., 2008), indentation (Carter et al., 2001; Tay et al., 2006; Samur et al., 2007) and aspiration (Mazza et al., 2006; 2007; Nava et al., 2003; 2008) have been explored. Hu and Desai (2004) performed compression experiments on samples of porcine livers. Chui et al. (2004) performed cycle of compression and elongation of porcine liver samples and propose a combined logarithmic and polynomial constitutive equation for liver tissue modeling. Samur et al. (2003) developed a robotic indenter to measure soft tissue property with indentation up to 8mm. A hand-held instrument for aspiration experiments is developed by Vuskovic (2001) to measure the mechanical responses of a human uterine cervix and liver.

In soft tissue deformation, the tissue is subjected to compression, tension and shear. Liver tissue behavior in one deformation mode is considerately different from that of other modes (Gao et al., 2010). It is reported that soft tissue indentation is affected by

both its compressive and tensile characteristics of the soft tissue. However, indentation is usually simulated using material parameters derived from either sample compression or elongation test. This method is inaccurate since only compressive or tensile characteristic is considered. Even though material parameters determined from indentation tests (Delalleau et al., 2006; Liu et al., 2008; Namani and Simha, 2009) incorporate both behaviors, they are prone to variation according to different indenter shapes, indentation depth and experimental conditions (Ahn and Kim, 2010; Liu et al., 2004; Gao et al., 2010) calibrated liver tissue property by performing pure shear, unconfined compression and uniaxial tension tests. Nevertheless, the results were not verified through actual 3D deformation tests.

An objective of our study is to realistically simulate the deformation of liver tissue under large indentation. Rigid flat-ended cylindrical indenter was used in this study. *In vitro* indentation was modeled using an axisymmetric FE model with tissue material represented by a 5-constants Mooney-Rivlin hyperelastic model. Abaqus which is commercially available FE software is used in the study. Material parameters were derived from uniaxial stress-strain data of compressions, elongations, and cycle of compression and then elongation of porcine liver samples respectively using inverse FE method. *In vitro* indentation tests were performed to validate the FE simulation. Stress-strain data from the simulation with material parameters derived from cycle of compression and then elongation match the experimental data best. We demonstrated that more accurate simulation result can be achieved by using a hyperelastic model with material parameters determined from combined compression and elongation stress-strain curve.

6.1 Soft Tissue Loading Experiments

6.1.1 Compression and Tensile Test

Uniaxial stress-strain data were obtained from *in vitro* experiments on 20 porcine livers for compressions, elongations and cycle of compression and then elongation. There were about 70 cylindrical samples, with diameter 7 mm and varying height (4-11 mm). Force and displacement were measured during the loading test by an Eztest precision instrument. This instrument had a resolution of ±1% and could support loading rates ranged from 0.5 to 1000 mm per minute. We used a load cell that was capable of measuring a force up to 20 N. Details of this experiment can be found in Chui et al. (2004).

6.1.2 Indentation Test

An indentation test similar to that of compression and tensile test in Section 2.1 was performed to validate FE simulation of indentation. A snap shot the indentation experiment was shown in Figure 6-1. Porcine liver tissue sample was harvested from fresh porcine liver. The sample was contained in a cylindrical glass container during experimentation. The volume and weight of liver sample were 120 ml and 136 g respectively. A probe of with diameter of 5mm was used in the indentation test. The standard test rate was 10 mm/min - the same as that of our compression and elongation experiments reported in Chui et al. (2004).

Figure 6-1. Snap shot of indentation experiment

6.2 Hyperelastic Models

A well-known approach for studying hyperelastic constitutive relationships of bodies capable of finite deformation is to postulate that elasticity has the form of an elastic potential energy, or strain energy functionW. The strain energy for an elastic body is a function of the state of deformation. Various hyperelastic strain energy functions were developed in both conventional mechanical engineering and biomechanical engineering communities.

Soft tissue is assumed to be fully incompressible in this study. The simplest isotropic energy model is Neo-Hooken model:

$$W = C_1(I_1 - 3) \tag{6.1}$$

A commonly used model is the 2-constants Mooney-Rivlin model:

$$W = C_1(I_1 - 3) + C_2(I_2 - 3) \tag{6.2}$$

However, simple hyperelastic models, e.g. the Neo-Hookean and the 2-constants Mooney-Rivlin, cannot provide acceptable curve fitting during soft tissue modeling at

large strains. The Neo-Hookean model is only accurate for strains less than 20% (Gent, 2000). This study uses a 5-constants Mooney-Rivlin model:

$$W = C_1(I_1 - 3) + C_2(I_2 - 3) + C_3(I_1 - 3)^2 + C_4(I_1 - 3)(I_2 - 3) + C_5(I_2 - 3)^2 \quad (6.3)$$

6.3 Material Parameters Estimation

Material parameters are often calculated by fitting the theoretical-derived stress-strain curves with experimental curves. However, material parameter calculated by this method may be inaccurate since this method does not represent the actual experimental conditions. For example, if uniaxial stress-strain data is provided, stress and strain are only considered in one direction. Inverse FE method incorporating the realistic experimental conditions is used to calculate the material parameters in this study.

6.3.1 FE Simulation of Porcine Liver Sample Testing

An axisymmetric FE model was built to simulate the porcine liver sample testing experiment. The FE model was divided into 559 nodes and 510 axisymmetric elements (CAX4RH). Since the tissue sample was glued to attachment at both ends in the experiment, the bottom of the FE model was fixed in both X and Y directions. Abaqus curve fitting tool can estimate material parameters by curve fitting the theoretical stress with experimental data. Three sets of hyperelastic parameters were first calibrated by Abaqus curve fitting tool using uniaxial stress-strain data of compressions, elongations, and cycle of compression and then elongation respectively. Forward FE analysis was then performed using these three sets of material parameters.

The model was first compressed to a maximum strain of 0.7 and then elongated to a maximum strain of 1.4. For illustration, contours of the von Mises stress are shown for compression and elongation (Figure 6-2).

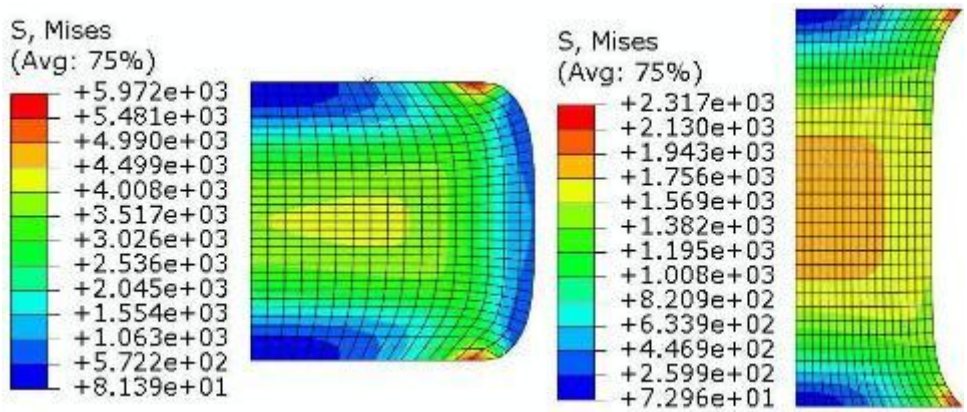

(a) (b)

Figure 6-2. Contours of von Mises stress of liver sample testing. (a) Compression, (b) elongation

6.3.2 Inverse FE Characterization

Using the material parameters calibrated by Abaqus curve fitting tool, simulated stress-strain curves were obtained for compressions, elongations and cycle of compression and then elongation respectively. We can observe that the simulated stress-strain curve does not correspond well with the experimental data (Figure 6-4, Figure 6-5 and Figure 6-6). A LM optimization procedure was performed to minimize the error between the simulated stress data and the experimental stress data. The objective function was defined by

$$\mathrm{R}(x) = \sum_{1}^{n} (s_{true} - s_{simu})^2 \tag{6.4}$$

where the s_{true}, s_{simu} and n are experimental stress, simulated stress and number of data points respectively. The flow chart of the inverse algorithm is shown (Figure 6-3).

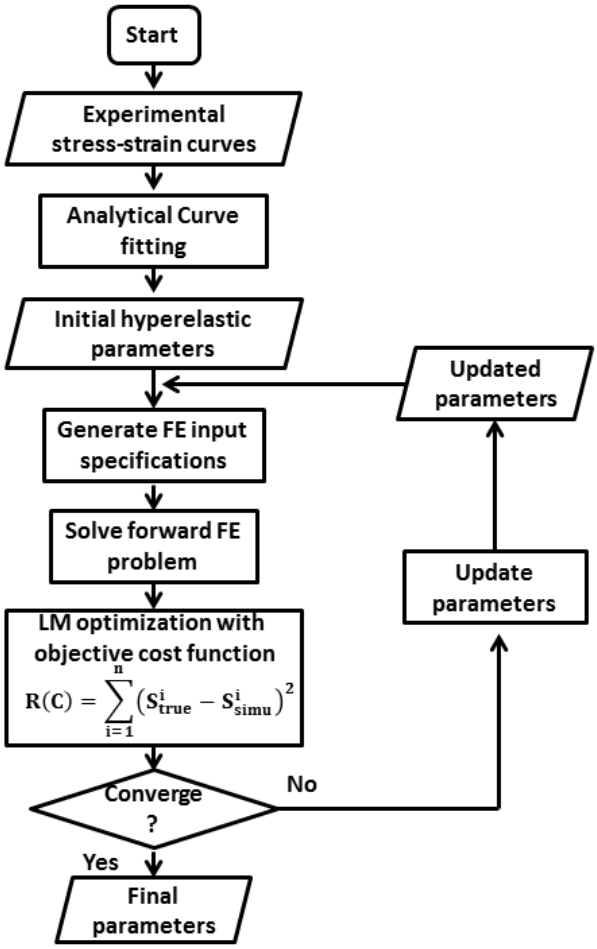

Figure 6-3. Flow chart of the inverse FE optimization algorithm

Another three sets of material parameters were obtained after optimization for compressions, elongations, and cycle of compression and then elongation respectively. Simulated stress-strain curves were plotted together with experimental stress-strain curves. Better correspondence can be observed with material parameters calculated by the inverse FE method than that of material parameters calculated using Abaqus curve fitting tool. Standard error was the RMSE due to the difference between simulated stress and experimental stress. Calculated material parameters and RMSE are shown in Table 6-1. The RMSE with parameters derived by inverse FE method is on average 17.22 times smaller than that of Abaqus curve fitting tool.

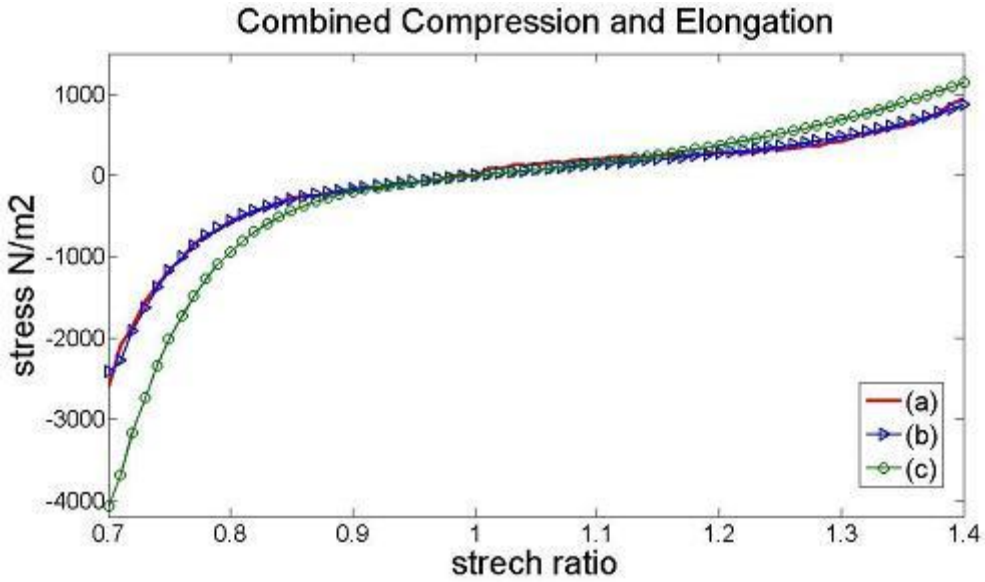

Figure 6-4. Stress-strain curves of combined sample compression and elongation. (a) Experimental data, (b) simulation with material parameters derived by inverse FE method, (c) simulation with material parameters derived by Abaqus curve fitting tool

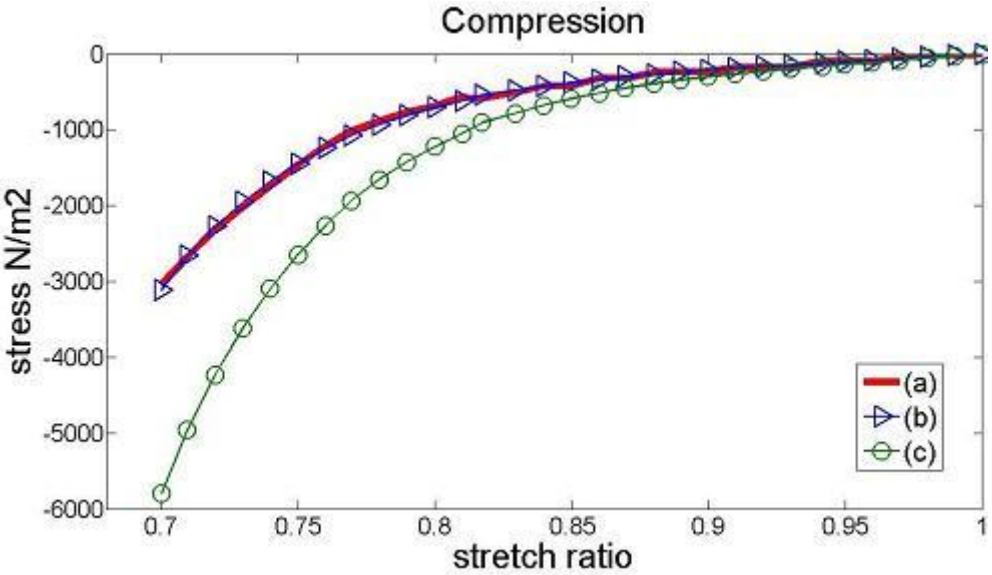

Figure 6-5. Stress-strain curves of sample compression. (a) Experimental data, (b) simulation with material parameters derived by inverse FE method, (c) simulation with material parameters derived by Abaqus curve fitting tool

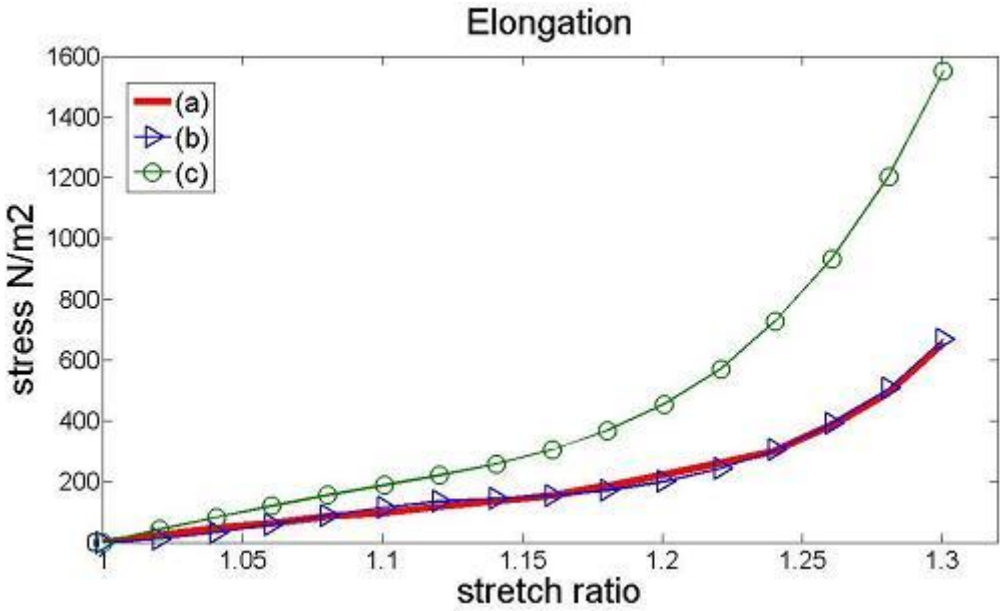

Figure 6-6. Stress-strain curves of sample elongation. (a) Experimental data, (b) simulation with material parameters derived by inverse FE method, (c) simulation with material parameters derived by Abaqus curve fitting tool

6.4 Simulation of Liver Tissue Indentation

In vitro porcine liver indentation was simulated using an axisymmetric FE model (Figure 6-7(a)). Axisymmetric elements CAX4RH and CAX3H were used in the modeling. The indenter was modeled as an analytical rigid body with a flat-ended cylindrical shape 5mm in diameter. A 'contact pair' was used to model the contact between indenter and soft tissue. The indenter is modeled as 'master' surface while the soft tissue is modeled as 'slave'. An indentation depth of 1cm is applied. A tangential friction coefficient of 0.8 was used to simulate the contact friction between the soft tissue and the indenter. The bottom was constrained in the y direction while the edge was constrained in the x direction. Enhanced hourglass control was used to prevent zero-energy mode in simulation. For illustration, the deformed contour is shown in Figure 6-7(b). We observe that neither serious penetration nor zero-energy mode happens in the simulation.

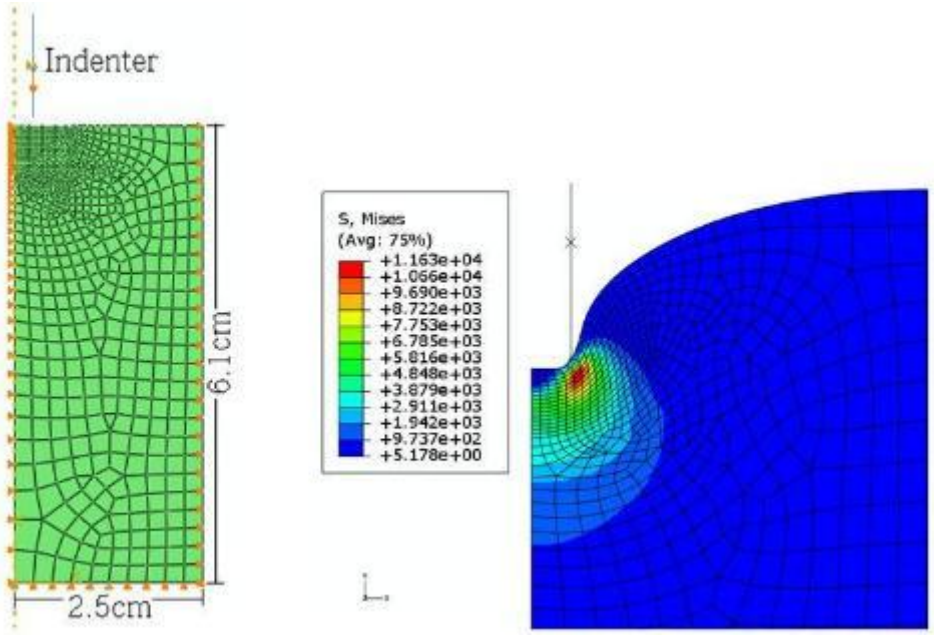

(a) (b)

Figure 6-7. FE model. (a) FE mesh and model size, (b) stress contour on deformed mesh

Simulation was performed using the six sets of parameters obtained in the previous section. Simulated indentation stress-strain curves were compared with the experimental stress-strain curves (Figure 6-8). Figure 6-8 was zoomed to show the result more clearly (Figure 6-9). RMSE was calculated for all six sets of material parameters (Table 6-1). Stress-strain data from the simulation with material parameters derived from cycle of compression and then elongation match the experimental data best.

The RMSE from indentation with parameters derived from combined compression and elongation cycle is 15.81 times smaller than that of elongation and 1.53 times smaller than that of compression. Indentation is subject to both components of tissue compression and elongation and is dominated by the component of tissue compression. This agrees well with the fact that the reduction of RMSE on compression (1.53 times) is much less than that of the elongation (15.81 times).

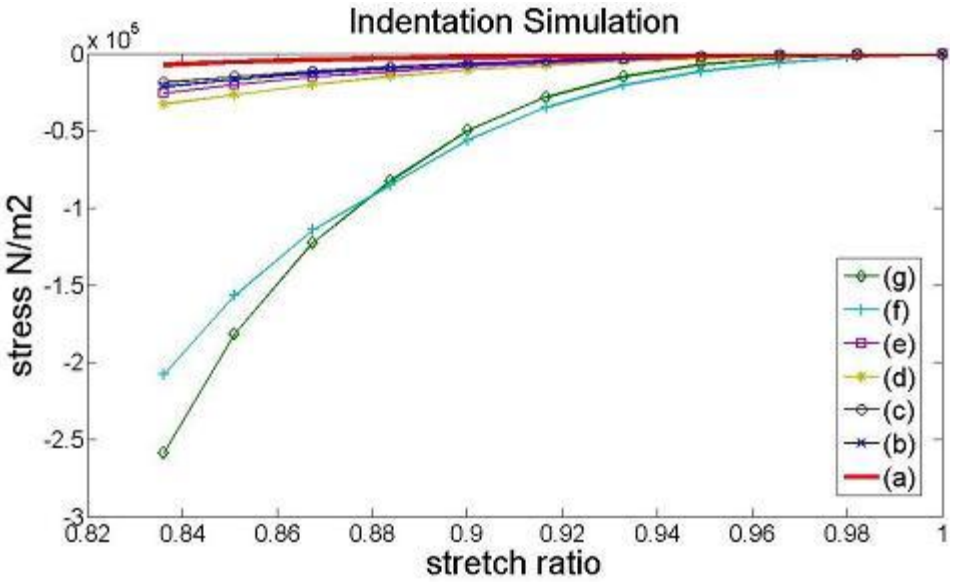

Figure 6-8. Stress-strain curves of indentation. (a) Experimental data, (b) simulation with material parameters derived from combined sample compression and elongation data using Abaqus curve fitting tool, (c) simulation with material parameters derived from combined sample compression and elongation data using inverse FE method, (d) simulation with material parameters derived from sample compression data using Abaqus curve fitting tool, (e) simulation with material parameters derived from sample compression data using inverse FE method, (f) simulation with material parameters derived from sample elongation data using Abaqus curve fitting tool, (g) simulation with material parameters derived from sample elongation data using inverse FE method

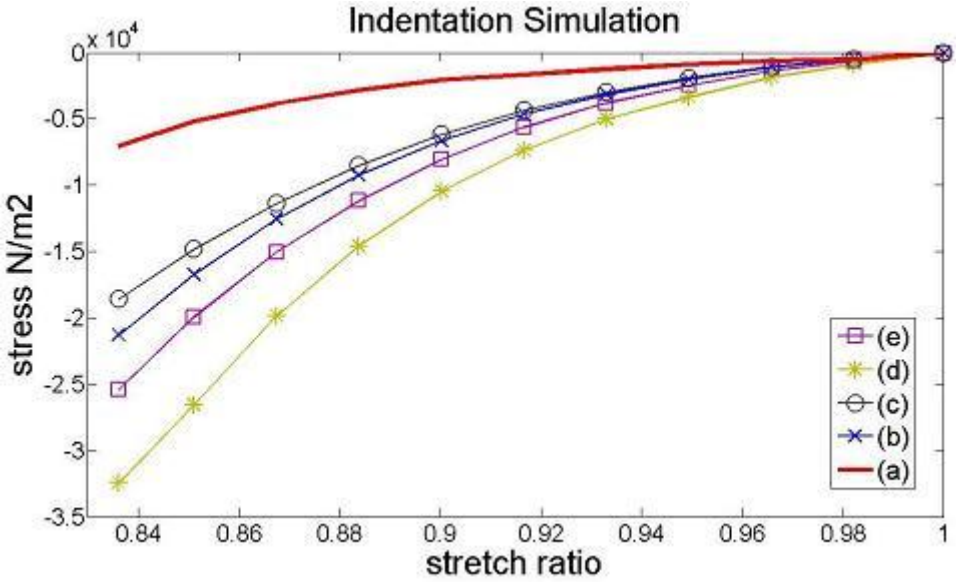

Figure 6-9. Stress-strain curves of indentation. (a) Experimental data, (b) simulation with material parameters derived from combined sample compression and elongation data using Abaqus curve fitting tool, (c) simulation with material parameters derived from combined sample compression and elongation data using inverse FE method, (d) simulation with material parameters derived from sample compression data using Abaqus curve fitting tool, (e) simulation with material parameters derived from sample compression data using inverse FE method

Table 6-1. Parameters of Mooney-Rivlin (five constants) and RMSEs for liver tissue sample testing and indentation

Uniaxial deformation type		Compression		Elongation		Compression and elongation	
		Abaqus curve fitting	Inverse FE	Abaqus curve fitting	Inverse FE	Abaqus curve fitting	Inverse FE
Mooney-Rivlin 5 Constants (Pa)	C_1	1217.6	863.5	-397.6	1103.2	286.9	242.3
	C_2	-854.7	-584.6	607.7	-1135.6	-96.8	-53.4
	C_3	5029.8	3228.7	77387.0	75227.0	1926.0	4140.1
	C_4	-9476.4	-6228.9	-176837.8	-178940.0	-4164.4	-8583.5
	C_5	5204.8	3328.6	101733.5	106010.0	2649.1	4419.6
RMSE of Sample testing (Pa)		931.4	35.7	356.8	12.8	419.8	50.7
RMSE of Indentation (Pa)		12156.3	8608.6	88672.0	103492.7	6667.3	5609.5

6.5 Discussions and Conclusion

Most medical simulation systems are based on material parameters derived from either pure sample compression or pure sample elongation. However, soft tissue deformation is subject to both compression and tension. Liver tissue behavior in one deformation mode is considerately different from that of other modes. We verify that a combined compression and elongation stress-strain data can be used to obtain better simulation results through an indentation simulation test.

An objective of our study is to realistically simulate the deformation of liver tissue under large indentation. Liver tissue indentation was modeled using an axisymmetric FE model. A 5-constants Mooney-Rivlin hyperelastic model is used to represent the mechanical properties of porcine liver tissue. The material parameters were derived from uniaxial stress-strain data of compressions, elongations, and cycle of compression and then elongation of porcine liver samples using inverse FE method. In vitro indentation tests were performed to validate the FE simulation. Simulation results show that the material parameters determined from cycle of compression and

then elongation give the best simulation result in modeling porcine liver tissue indentation.

The demonstration of this hypothesis that the application of experimental data from uniaxial compression and then elongation is adequate for simulating the 3D deformation of soft tissue is important. Biaxial loading experiment is difficult to be performed. The properties of soft tissue sample could be affected by its preparation for loading test. However, there are obvious limitations on application of uniaxial loading data for 3D deformation. Finite element method and combined cycle of compression and elongation is a viable approach for realistic simulation of soft tissue deformation.

We attempted to further minimize the error between experiment and simulation result by using other incompressible hyperelastic models. Despite the additional simulations, it was difficult to obtain better results. However, accuracy of the simulation can be further improved by considering soft tissue anisotropy, compressibility or FE model refinement. Although linear element is used in this study, higher order elements can be used within the field of interest to improve the accuracy of FE model. Despite the limitations, the proposed simulation method provides two basic uses in medical simulators. First, accurate deformations and tool-tissue interaction forces can be computed. Second, the soft tissue characterization method proposed here could be used as a reference to evaluate the accuracy of soft tissue characterization methods under different deformation modes (e.g. confined/unconfined equibiaxial compression and tension, planar compression and tension).

CHAPTER 7 PROBABILISTIC MODELING OF PORCINE LIVER TISSUE FOR DEFORMATION STUDIES

Understanding mechanical property of liver is important for tumor diagnosis, surgery planning and medical simulation. In order to quantitatively measure the responses of soft tissues, numerous techniques, including sample compression (Chui et al., 2004; 2007; Hu and Desai, 2004; Rosen et al., 2008), indentation (Carter et al., 2001; Tay et al., 2006; Samur et al., 2007) and aspiration (Nava et al., 2003; 2008; Mazza et al., 2006; 2007;) have been explored. Chui et al. performed compression and elongation of porcine liver samples and proposed a combined logarithmic and polynomial constitutive equation for liver tissue modeling (Chui et al., 2004). Samur et al. developed a robotic indenter to measure soft tissue property with indentation up to 8mm (Samur et al., 2007). A hand-held instrument for aspiration experiments is developed by Vuskovic to measure the mechanical responses of a human uterine cervix and liver (Vuskovic, 2001). Though various techniques have been explored to estimate liver tissue property, it remains challenging to accurately determine material parameters for practical liver tissue deformation simulation.

A number of diverting stress-strain curves are usually measured from loading tests of many liver tissue samples. There are two main reasons for the diverting measurements of liver tissue stress-strain data. Firstly, different liver tissue samples are subjected to inherent stiffness variations due to their different anatomic microstructures. Secondly, there are noises during experiments which may lead to inconsistent measurements of stress and strain data. Soft tissue material parameters are often derived from the average stress-strain curve. However, it is important to incorporate the inherent

stiffness variations of liver tissue in the constitutive model for accurate simulation of liver tissue deformation.

Probabilistic uncertainty analysis which quantifies the effect of input random variables on model outputs is hypothesized to be a plausible approach to model the inherent stiffness variations of liver tissue. Probabilistic uncertainty analysis is increasingly applied in biomechanics and orthopedics to account for variability and uncertainty in material properties, geometry and dynamics of biological hard tissue (Laz and Browne, 2009). To our best knowledge, there is no report on the application of probabilistic analysis in soft tissue characterization and deformation simulation.

In this chapter, we propose a nondeterministic approach to model the inhomogeneity, specifically the stiffness variations of porcine liver tissue under compression. Uniaxial stress-strain data were obtained from *in vitro* loading experiments of 70 porcine liver tissue samples. The biological tissue is highly inhomogeneous with diverting stress-strain curves. Experimental strain values at a specific stress were assumed to vary according to a normal distribution, and Mooney-Rivlin hyperelastic constitutive equation was used to represent the average stress-strain relationship of porcine liver tissue. The material parameters of the constitutive equation were expressed as a statistical function with normal distribution. Mean and standard deviation of these material parameters were determined using inverse FE method and inverse mean-value first-order second-moment (IMVFOSM) method respectively. Computer simulation based on direct Monte-Carlo (MC) method was used to verify the nondeterministic approach. Simulated cumulative distribution function (CDF) corresponded well with that of the experimental stress-strain data. The statistical

material parameters were able to model the stress-strain curves from separate liver tissue compression tests. Stress-strain data from these new tests are within three standard deviations from mean $(\boldsymbol{\mu}_\varepsilon - 3\sigma_\varepsilon, \boldsymbol{\mu}_\varepsilon + 3\sigma_\varepsilon)$ predicted using the nondeterministic material parameters.

7.1 Nondeterministic Material Parameter Estimation

Consider a structural problem where uncertain parameters are characterized by a random variable vector $\boldsymbol{X} = [X_1, X_2 \cdots X_n]^{\mathrm{T}}$. Assume that the performance function is $Y = g(\boldsymbol{X})$. The CDF of can be calculated by a multi-dimensional integral,

$$F(y) = P\{Y \le y\} = \int_{g(X) \le y} f_{\boldsymbol{X}}(\boldsymbol{X}), \tag{7.1}$$

where is the joint probability density function of random variables . Various probabilistic uncertainty analysis techniques have been proposed to obtain the solution to this integration in the last decades (Hasofer and Lind, 1974; Zhao et al., 2003; Huang and Du, 2008).

Deformation of liver tissue sample is regarded as a structural problem that can be studied using a nondeterministic method. Forward FE analysis was utilized as the performance function,

$$\varepsilon = g_{FE}(\boldsymbol{C}), \tag{7.2}$$

where ε is the strain, $\boldsymbol{C} = [C_1, C_2 \cdots C_5]^{\mathrm{T}}$ is the hyperelastic material parameter vector. Outputs of the performance function, mean μ_ε and standard deviation σ_ε of the experimental strain values, are known while input variables of the performance function,

the hyperelastic material parameter vector $\boldsymbol{C}$, are unknown. In order to determine the material parameter vector $\boldsymbol{C}$ from the experimental strain ε, we are solving an inverse problem of conventional probabilistic uncertainty analysis which quantifies the effect of input random variables on model outputs.

This section introduces a nondeterministic approach to determine material parameters from the diverting stress-strain curves. Mean values of the material parameters were determined using inverse FE method. The standard deviations of the material parameters were estimated using an IMVFOSM method.

7.1.1 Liver Tissue Sample Loading Tests

Uniaxial stress-strain data of compression were obtained from in vitro experiments on 70 cylindrical samples from 20 porcine livers. Force and displacement were measured during the loading test by an Eztest precision instrument. This instrument had a resolution of ±1% and could support loading rates ranged from 0.5 to 1000 mm per minute. A load cell that was capable of measuring a force up to 20 N has been used. In this study, we refer to stress and strain in the Lagrangian sense. The stress is the load divided by the cross-sectional area of the sample at zero-stress state. The compression ratio is the ratio of the length or height of the sample compressed under the load divided by the initial length at the zero-stress state. Details of this experiment can be found in (Chui et al., 2004).

Experimental strain under a certain stress is assumed to vary according to normal distribution. Mean and standard deviation of strain is calculated as

$$\mu_\varepsilon = \frac{1}{N}\sum_{i=1}^{N}\varepsilon_i,\ \sigma_\varepsilon = \sqrt{\frac{1}{N}\sum_{i=1}^{N}\left(\varepsilon_i - \mu\right)^2}, \tag{7.3}$$

where is the experimental strain value and is the number of experimental strain values. Figure 7-1 shows the minimum, mean and maximum experimental stress-strain curves from uniaxial compression of porcine liver tissue samples. Probability density functions (PDF) of the strain values have been plotted at certain stress values to illustrate the normal distribution of strain values.

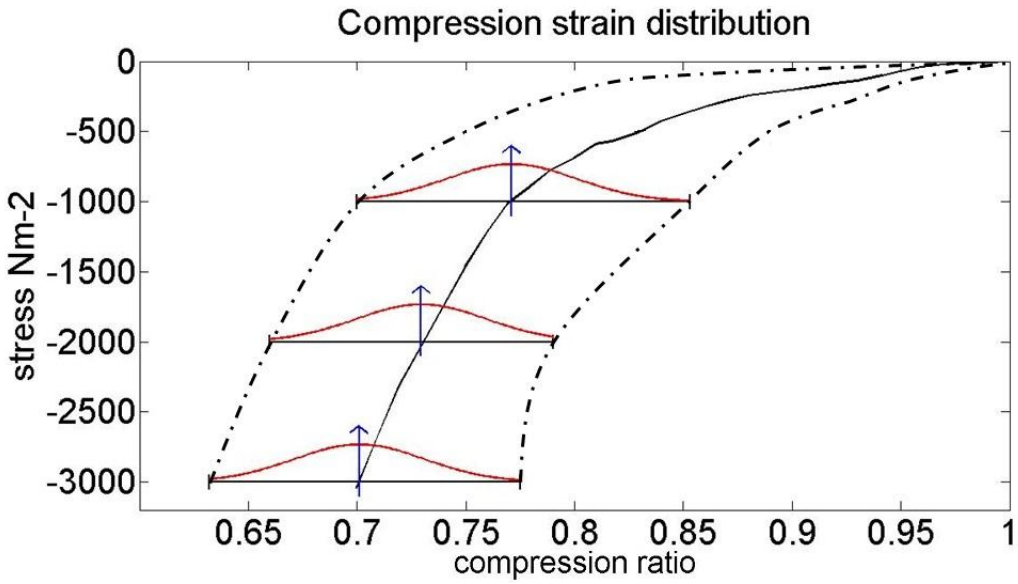

Figure 7-1. Stress-strain curves from uniaxial compression measurements with porcine liver tissue. (—) Mean, (-.) maximum and minimum values of strain. Normal distribution of strain values is indicated along horizontal bars

7.1.2 Forward FE Analysis of Porcine Liver Sample Compression

Soft tissue was assumed to be fully incompressible and was represented using a 5-constant Mooney-Rivlin model:

$$W = C_1\left(I_1 - 3\right) + C_2\left(I_2 - 3\right) + C_3\left(I_1 - 3\right)^2 + C_4\left(I_1 - 3\right)\left(I_2 - 3\right) + C_5\left(I_2 - 3\right)^2 \tag{7.4}$$

where W is the strain energy function, $C_1 \cdots C_5$ are the material parameters, I_1 and I_2 are strain invariants.

Abaqus, a commercial solver, has been used to solve the forward FE problems to determine the simulated stress-strain relationship of live tissue compression. An axisymmetric FE model was constructed to simulate the cylindrical porcine liver sample compression experiments. The FE model has a total number of 559 nodes and 510 axisymmetric (CAX4RH) elements. Since the tissue sample was glued to attachment at both ends in the experiments, the bottom surface was fixed in both x and y directions and the top surface was fixed in x direction. The sample was compressed to a maximum strain of 0.7. FE model and its boundary conditions are shown in Figure 7-2(a), and contours of the von Mises stress are shown in Figure 7-2(b).

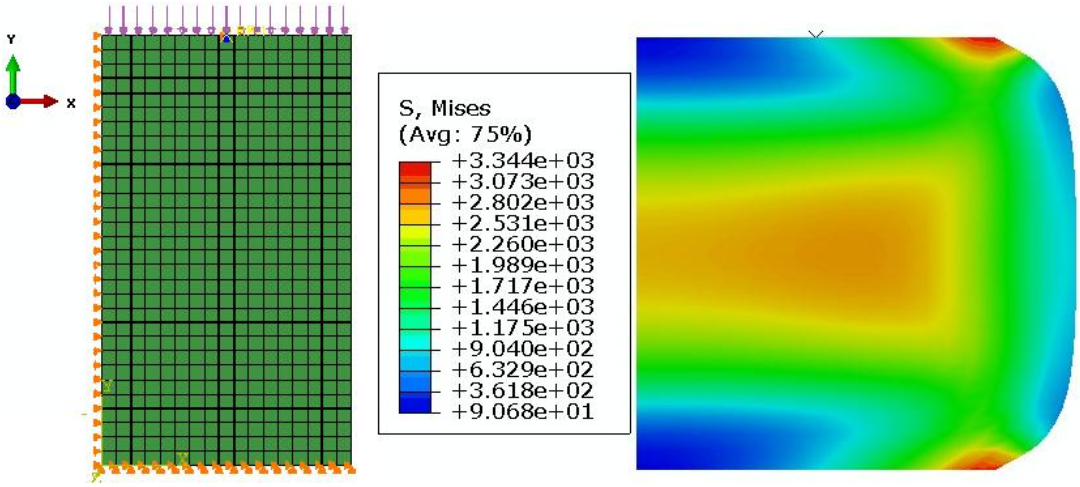

(a) (b)

Figure 7-2. Liver sample compression simulation. (a) FE model and boundary conditions, (b) von Mises stress contour

7.1.3 Mean of Material Parameters

Initial material parameters were first estimated using Abaqus curve fitting tool which fits analytical stress-strain curve of the hyperelastic model to the average experimental stress-strain curve. LM optimization algorithm was implemented to minimize the error between simulated stress values and corresponding experimental stress values. Material

parameters were updated in each optimization step. Objective function of the optimization algorithm was defined by

$$R(\boldsymbol{C}) = \sum_{i=1}^{n} \left(S_{true}^{i} - S_{simu}^{i} \right)^2 \tag{7.5}$$

where $\boldsymbol{C}$ is the material parameter vector, S_{true}^{i}, S_{simu}^{i} and n are experimental stress, simulated stress and number of sampled stress values respectively.

Flow chart of this inverse FE characterization method is shown in Figure 6-3. Mean value of material parameters were obtained after convergence of LM optimization. Forward FE analyses of liver tissue sample compression were performed with material parameters determined using Abaqus curve fitting tool and inverse FE characterization respectively. Simulated stress-strain curves were plotted together with experimental stress-strain curve in Figure 7-3. Simulated stress-strain curve with material parameters determined using inverse FE characterization better fits the experimental stress-strain curve than that of the material parameters determined using Abaqus curve fitting tool. Table 7-1 presents the material parameters and RMSE between the simulated stress and the corresponding experimental stress at specific strains. The RMSE with material parameters derived using inverse FE characterization is 26 times smaller than that of the material parameters derived using Abaqus curve fitting tool.

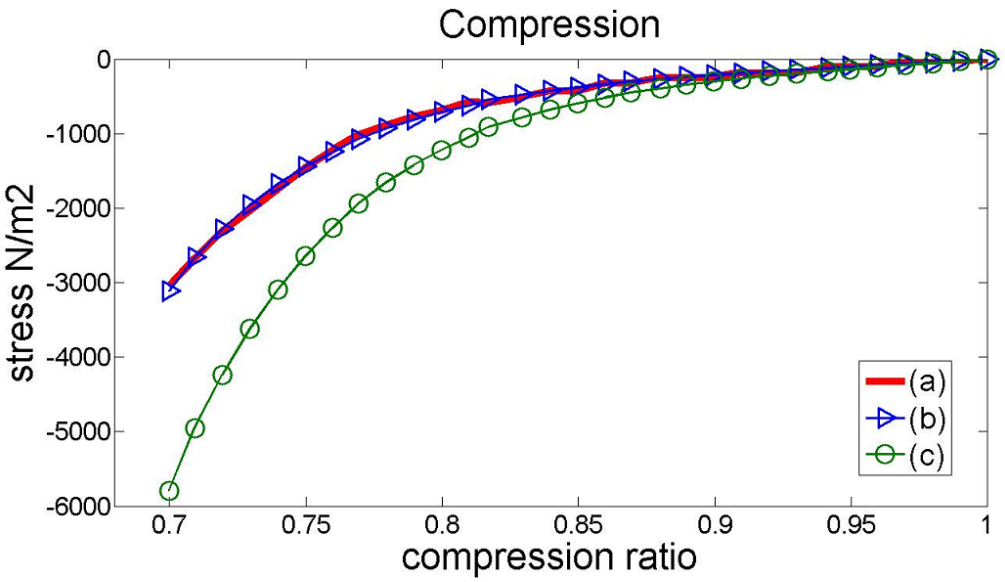

Figure 7-3. Stress-stain curves of liver sample compression. (a) Mean curve of experimental data, (b) Simulated curve with material parameters derived using inverse FE optimization, (c) Simulated curve with material parameters derived using abaqus curve fitting tool

Table 7-1. Estimated mean values of material parameters

Uniaxial deformation type		Compression	
Characterization method		Abaqus curve fitting	Inverse FE optimization
Material parameters mean values (Pa)	C_1	1217.6	863.5
	C_2	-854.7	-584.6
	C_3	5029.8	3228.7
	C_4	-9476.4	-6228.9
	C_5	5204.8	3328.6
RMSE of sample testing (Pa)		931.4	35.7

7.1.4 Standard Deviation of Material Parameters

Using Taylor expansion, the performance function of Equation 7.2 is linearized at the mean values of material parameters:

$$\varepsilon \cong g\left(\boldsymbol{\mu}_{\boldsymbol{C}}\right)+\sum_{i=1}^{n}\left.\frac{\partial g_{FE}}{\partial C_i}\right|_{\boldsymbol{\mu}_{\boldsymbol{C}}}\left(C_i-\mu_{C_i}\right), \tag{7.6}$$

where $\boldsymbol{\mu}_{\boldsymbol{C}}=\left[\mu_{C_1},\mu_{C_2}\cdots\mu_{C_5}\right]^{\mathrm{T}}$ is the mean values of $\boldsymbol{C}=\left[C_1,C_2\cdots C_5\right]^{\mathrm{T}}$. Mean and standard deviation of simulated ε can be estimated respectively by

$$\mu_{\varepsilon}\cong g(\boldsymbol{\mu}_{\boldsymbol{C}}), \tag{7.7}$$

and

$$\sigma_{\varepsilon} \cong \sqrt{\sum_{i=1}^{n} \left(\left. \frac{\partial g_{FE}}{\partial C_i} \right|_{\boldsymbol{\mu_C}} \sigma_{C_i} \right)^2} \,, \tag{7.8}$$

where σ_{C_i} is the standard deviation of material parameter C_i. The partial derivative $\partial g_{FE} / \partial C_i$ in this equation is numerically calculated using finite different method.

With standard deviation σ_{ε} of the experimental strain values known, and $\partial g_{FE} / \partial C_i$ determined above, we are solving an inverse problem of conventional probabilistic uncertainty analysis to determine σ_{C_i}. Inverse mean-value first-order second-moment (IMVFOSM) method refers to this solution process.

LM optimization method can be used to find σ_{C_i} that best meets Equation 7.8 along the stress-strain curve. The parameter estimation process can be simplified by evaluating Equation 7.8 at five different stress values: -1000 Nm^{-2}, -1500 Nm^{-2}, -2000 Nm^{-2}, -2500 Nm^{-2} and -3000 Nm^{-2}. The numerical solution process may cause matrix singularity, which causes the solution of C_i not exist or not unique. This may be overcome by assuming that the standard deviations of some of the parameters are zero. Table 7-2 shows an example set of nondeterministic material parameters. Alternatively, the problem of matrix singularity maybe reduced by evaluating Equation 7.8 at many instantaneous stress values.

Table 7-2. Estimated nondeterministic material parameters of liver tissue

Material parameters	$\boldsymbol{C}_1$	$\boldsymbol{C}_2$	$\boldsymbol{C}_3$	$\boldsymbol{C}_4$	$\boldsymbol{C}_5$
Mean $\boldsymbol{\mu_{C_i}}$ (Pa)	863.5	-584.6	3228.7	-6228.9	3328.6
Standard deviation $\boldsymbol{\sigma_{C_i}}$ (Pa)	80.8	0	0	0	230.5

7.2 Verification using Monte Carlo Simulation

MC method is one of the commonly used sampling based methods (Mckay et al., 1979; Dey and Mahadevan, 1998; Ding et al., 1998; Moarefzadeh and Melchers, 1999; Helton and Davis, 2003). The MC methods belong to a class of computational algorithms which rely on repeated random sampling to compute their results. They are often used in computer simulation of physical and mathematical systems when it is infeasible to compute an exact result with a deterministic algorithm (Anderson, 1986). Result with high confidence could be obtained from sufficient number of simulations. Despite its computational inefficiency, MC simulation is frequently used to verify newly proposed probabilistic analysis methods.

To verify the correctness of the nondeterministic material parameters estimation method, forward FE analyses described in section 7.1.2 were performed for 500 times with the material parameters displayed in Table 7-2. Strain CDFs obtained from MC simulations at stress values of $-500Nm^{-2}$, $-1000Nm^{-2}$, $-1500Nm^{-2}$, $-2000Nm^{-2}$, $-2500Nm^{-2}$ and $-3000Nm^{-2}$ were plotted together with the experimental CDFs in Figure 7-4. Within the interval [0.2, 0.8] of CDFs, the simulated strain CDFs correspond well with that of the experimental strain CDFs. There are some discrepancies between the simulated strain CDFs and the experimental strain CDFs within the interval [0, 0.2] and [0.8, 1]. This is because the proposed IMVFOSM approach only uses the first two moments of the material parameters instead of the complete distribution information (Huang and Du, 2008).

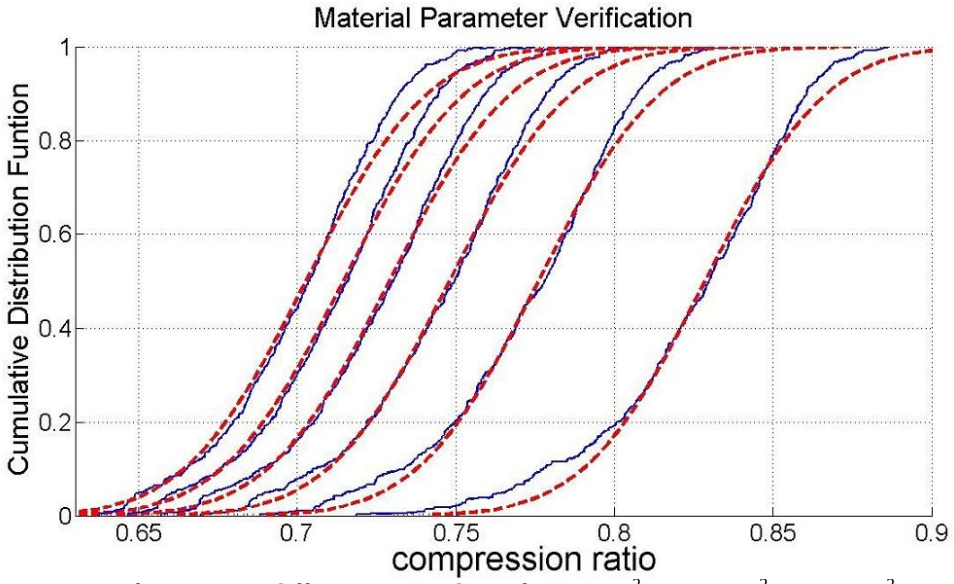

Figure 7-4. CDFs of strain at six different stress values of -500 Nm^{-2}, -1000Nm^{-2}, -1500Nm^{-2}, -2000Nm^{-2}, -2500Nm^{-2} and -3000Nm^{-2} from right to left. (--) Experimental CDFs, (—) CDFs from 500 FE evaluations with calculated nondeterministic material parameters

7.3 Experiments

Empirical rule or 3-sigma rule states that about 68% of values drawn from a normal distribution are within one standard deviation away from the mean; about 95% of the values lie within two standard deviations; and about 99.7% are within three standard deviations. The empirical rule is widely used in industrial products quality control. To determine soft tissue parameters, researchers need to deal with large amount of data from soft tissue loading tests. It is important to select useful data and delete inaccurate measurements from the dataset. In this study, the empirical rule is applied to evaluate the proposed method.

New compression tests were performed on porcine liver tissue samples with height of 10 mm and diameter of 14mm. There were a total of twenty stress-strain curves from the experiments. FE analysis was same as that described in section 7.1.2 with nondeterministic material parameters listed in Table 7-2. The model size was changed

in accordance to the sample size in the new tests. Simulated stress-strain curves were obtained and plotted together with the experimental mean stress-strain curves as shown in Figure 7-5. FE simulation results showed that experimental stress-strain curves of these new tests fall into the three standard deviation from the mean of the simulated strain. The results demonstrated that stress-strain data could be predicted using the nondeterministic material parameters.

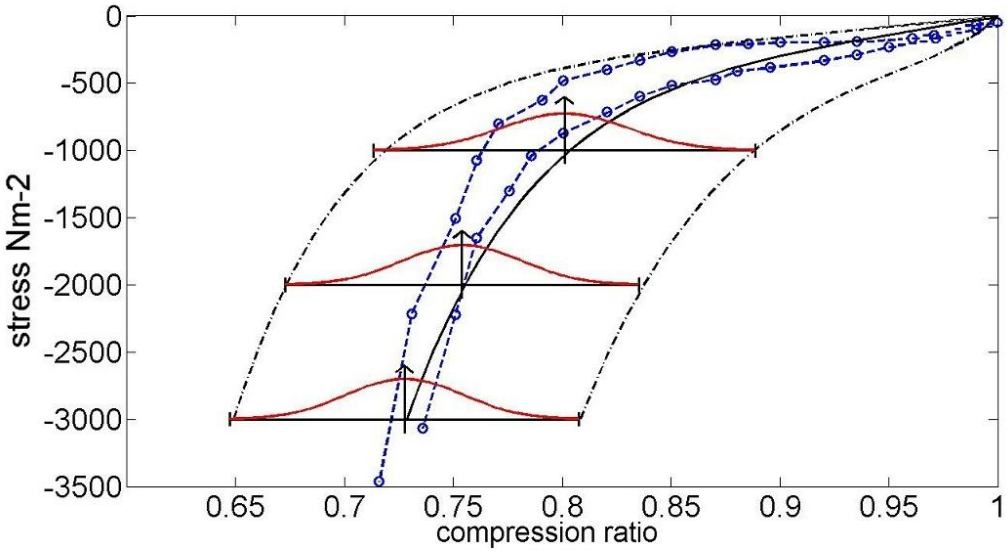

Figure 7-5. Stress-strain graphs. (—) Mean, (-.) maximum and minimum values of probabilistic FE simulation, (-◦) two average curves from separate liver tissue compression tests. Normal distribution of strain values is indicated along horizontal bars

Mean and standard deviation of simulated strain estimated using Equation 7.8 at stress value of -500Nm^{-2}, -1000Nm^{-2}, -1500Nm^{-2}, -2000Nm^{-2}, -2500Nm^{-2} and -3000Nm^{-2} with material parameters in Table 7-2 are displayed in Table 7-3.

Table 7-3. Simulated strain of normal distribution

Stress(Nm^{-2})	500	1000	1500	2000	2500	3000
Mean of strain μ_ε	0.8547	0.8011	0.7732	0.7541	0.7395	0.7277
Standard deviation of strain σ_ε	0.0287	0.0292	0.0284	0.0271	0.0274	0.0267

7.4 Discussions and Conclusion

Uncertainties, including variations of soft tissue stiffness, loading conditions and boundary conditions present in the field of medical simulation. Probabilistic analysis can provide quantitative characterization of how an output measure is affected by these uncertainties of input variables. In addition, probabilistic analysis can provide valuable insight into the robustness of medical device designs and the associated range of possible outcomes. With better medical hardware and improving computational resources, it is expected that application of probabilistic analysis in medical field will continue to grow.

Probabilistic uncertainty analysis has been used to investigate ultra-structural properties of bone which is modeled by mineral-collagen composite (Dong, 2009). Easley et al. performed probabilistic FE analysis for orthopedic applications (Easley, 2007). Probabilistic FE analysis is also used to evaluate knee replacement mechanics of knee wear simulator (Laz et al., 2006). Nevertheless, little work has been done on the probabilistic uncertainty analysis for liver tissue deformation simulation. The reason may be twofold. Firstly, for liver deformation simulation, it is very difficult to define proper boundary and loading conditions due to the complex interaction with surrounding anatomies in the abdomen. Secondly, there is a need for an accurate method of modeling the liver tissue, or biological soft tissue inhomogeneity. Probabilistic soft tissue characterization which provides systematic derivation of nondeterministic soft tissue parameters may be a feasible solution for modeling tissue inhomogeneity. We propose a nondeterministic approach to model liver tissue inhomogeneity, and investigate its feasibility.

In probabilistic uncertainty analysis, it is difficult to obtain an analytical solution to the integration in Equation 7.1 due to both its nonlinear integration boundary and high dimensionality. Various probabilistic analysis techniques have been proposed to obtain the solution to this integration in the last decades. These techniques can roughly be categorized into three types: (1) sampling based methods, (2) moment matching methods, and (3) most probable point based methods (Huang and Du, 2008). The moment matching methods which only consider the first few moments of the variables distribution are often employed to simplify the problem. One commonly used method is the mean-value first order second moment (MVFOSM) approach, which employs the first order Taylor expansion at the mean values of random variables (Huang and Du, 2008). Inspired by the MVFOSM approach, the nondeterministic material characterization approach was proposed using inverse FE method and IMVFOSM method. The correctness of our nondeterministic approach was verified through direct MC simulations. The calculated material parameters were validated using data from new compression tests of liver samples.

We used a second order hyperelastic model, 5-constant Mooney-Rivlin model, to represent liver tissue because the second order polynomial equation is sufficient in modeling the diverting experimental stress-strain curves. Although incompressible 5-constant Mooney-Rivlin hyperelastic model is used throughout this study, the proposed method can be readily applied to other material models such as other constitutive models (Chui et al., 2004) and viscoelastic models (Yang et al., 2011). At a specific stress, experimental strains are assumed to vary according to normal distribution. We are now trying to extend our method from representing the strain variation from normal

distribution to beta distribution. The beta distribution may better represent the experimental strain values distribution compared to that of normal distribution.

Precise biomechanical measurement experiment of biological tissue was difficult to achieve. Minor inconsistencies in handling of the tissue samples will introduce significant errors to the experimental results. The environmental and instrumental noises cannot be prevented completely during experiments. The nondeterministic approach proposed may highlight the experimental data that are significantly different from the established norms, or the outliers.

In conclusion, the proposed method is an effective and efficient method to systematically estimate nondeterministic material parameters from diverting stress-strain data of liver tissue under compression. Our probabilistic uncertainty approach allows the inherent stiffness variations of biological soft tissue to be represented in a statistical model for accurate medical simulation.

CHAPTER 8 CONCLUSIONS AND FUTURE WORK

Despite over twenty years of research and development in MRE, there are many challenging scientific problems to be resolved. We have proposed a framework of quasi-static MRE to solve some of these problems. The framework is shown in Figure 8-1.

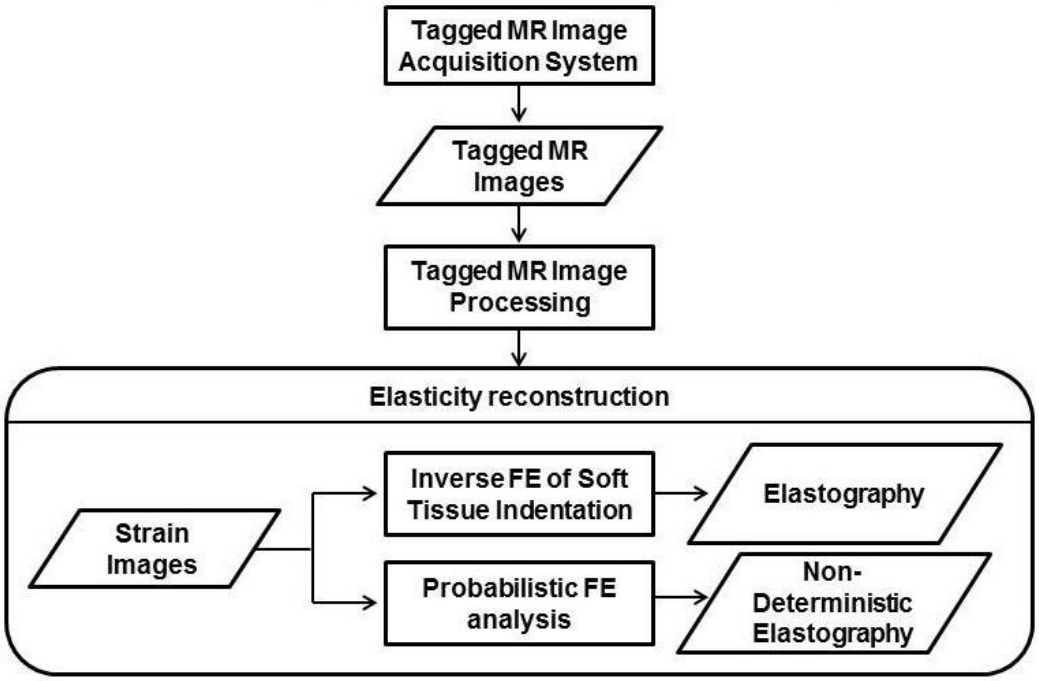

Figure 8-1. Framework of quasi-static MRE

1. Tagged MR Image Acquisition for Quasi-Static MRE

A new imaging method for internal deformation tracking of soft tissue was presented in Chapter 3. Using a MR compatible actuator, we extend the use of tagged MRI sequence from myocardial tissue to other soft tissue. The actuator was synchronized with SPAMM imaging sequence using simulated ECG signal and motor controlling software. This imaging method is effective and efficient to image soft tissue

deformation since the SPAMM imaging sequence is available in almost every clinical MR scanner and there is no need to detect imaging gradient from MR gradient cabinet. Our experimental results demonstrated the feasibility of this image acquisition system for soft tissue motion tracking and strain imaging.

2. Tagged MR Image Analysis

In Chapter 4, we presented new tagged MR images processing techniques for quasi-static MRE, myocardial diseases detections and cardiac function evaluations. Internal displacement field of soft tissue during deformation is required for the calculation of soft tissue elasticity distribution. Conventional harmonic phase (HARP) image processing technique is extended for large motion tracking during indentation using our image acquisition system. AWHARP which makes use of a local representation of the image spectra was proposed to help clinicians to detect LV abnormalities. AWHARP can determine displacement/strain images from tagged MR images accurately and efficiently. Results from our experiments with simulated tagged images and clinical MR images show that there is an improvement in performance with our method over the conventional HARP method.

3. Inverse Elasticity Problems

In Chapter 5, a new material parameter reconstruction method was proposed for hyperelastic material models by combining the FE-based direct inverse method and nonlinear optimization method. The FE-based direct inverse method provides an estimation of the true material parameter distribution. This estimation serves as the

initial guess of LM optimization algorithm. Direct calculation of Jacobian matrix was proposed to improve the computational efficiency of the LM optimization algorithm.

Both numerical consistency and noise sensitivity of the proposed method were tested in its application to solve 2D plain strain problems. The proposed method was also verified using different inclusion shapes under different strain levels. Computer simulation results show that our method is computationally efficient, and is accurate for determining the material parameter distribution. The improved computational efficiency can be attributed to both estimated initial guess that is close to the true material parameter distribution and direct calculation of the Jacobian matrix.

4. Modeling of Liver Tissue Indentation

In Chapter 6, a new soft tissue characterization method was introduced for liver tissue indentation simulation. Many medical simulation systems model tissue mechanical properties using constitutive equation with material parameters derived from either pure sample compression or pure sample elongation. However, soft tissue deformation is subject to both compression and tension. Liver tissue behavior in one deformation mode is considerately different from that of other modes. We demonstrated in this thesis that a combined compression and elongation stress-strain data can be used to obtain better simulation results through an indentation simulation test. Material parameters were derived from uniaxial stress-strain data of compressions, elongations, and cycle of compression and then elongation of porcine liver samples using inverse FE method. In vitro indentation tests were performed to

validate the FE simulation. Simulation results show that the material parameters determined from cycle of compression and then elongation give the best simulation result in modeling porcine liver tissue indentation. Experimental data from uniaxial compression and then elongation may be adequate for simulating 3D deformation of soft tissue.

5. Probabilistic FE Modeling of Liver Tissue

In Chapter 7, a nondeterministic approach is proposed to model the inhomogeneity, specifically the stiffness variations of porcine liver tissue under compression. The biological tissue is highly inhomogeneous with diverting stress-strain curves. Material parameters of hyperelastic constitutive equation were expressed as a statistical function with normal distribution. Mean and standard deviation of these material parameters were determined using inverse FE method and IMVFOSM method respectively. Computer simulation based on direct MC method was used to verify the nondeterministic approach. Simulated CDFs corresponded well with that of the experimental stress-strain data. This method is an effective and efficient method to estimate nondeterministic material parameters from diverting stress-strain data of liver tissue under compression.

With better imaging hardware and faster computers, quantitative elasticity imaging which relies on quantitative tissue characterization for routine clinical investigation is becoming a reality. However, to create a truly patient specific organ model for medical simulation with precise tissue mechanical properties derived from quantitative elasticity imaging remains a challenge. Unlike engineering materials, soft

tissue is highly nonlinear, anisotropic and non-homogeneous. A precise mathematical representation of tissue mechanical properties has yet to be found.

BIBLIOGRAPHY

Agarwal HK, Prince JL, Abd-Elmoniem KZ (2010) Total removal of unwanted harmonic peaks (TruHARP) MRI for single breath-hold high-resolution myocardial motion and strain quantification. Magn Reson Med 64(2):574-585

Ahn B, Kim J (2010) Measurement and characterization of soft tissue behavior with surface deformation and force response under large deformations. Med Image Anal 14(2):138-148

Aletras AH, Freidlin RZ, Navon G, Arai AE (2004) AIR-SPAMM: alternative inversion recovery spatial modulation of magnetization for myocardial tagging. J Magn Reson 166(2):236-245

Amini AA, Chen Y, Curwen RW, Mani V, Sun J (1998) Coupled Bsnake grids and constrained thin-plate splines for analysis of 2-D tissue deformations from tagged MRI. IEEE Trans Med Imag 17(3):344-356

Anderson HL (1986) Metropolis, Monte Carlo and the MANIAC. Los Alamos Science 14:96-108

Arts T, Prinzen FW, Delhaas T, Milles JR, Rossi AC, Clarysse P (2010) Mapping displacement and deformation of the heart with local sine-wave modeling. IEEE Trans Med Imag 29(5):1114-1123

Atalar E, McVeigh E (1994) Optimization of tag thickness for measuring position with magnetic resonance imaging. IEEE Trans Med Imag 13(1):152-160

Atay SM, Kroenke C, Sabet A, Bayly PV (2008) Measurement of the dynamic shear modulus of mouse brain tissue in vivo by magnetic resonance elastography. J Biomech Eng 130(2):021013

Axel L, Dougherty L (1989) MR imaging of motion with spatial modulation of magnetization for MR imaging. Radiology 171(3):841-845

Axel L, Montillo A, Kim D (2005) Tagged magnetic resonance imaging of the heart: a survey. Med Image Anal 9(4):376-393

Barajas J, Barnes JG, Carreras F, Pujadas S, Radeva P (2005) Angle images using Gabor filters in cardiac tagged MRI. Proc conf AI R&D:560-566

Barbone PE, Bambe JC (2002) Quantitative elasticity imaging: what can and cannot be inferred from strain images. Phys Med Biol 47(12):2147-2164

Barbone PE, Gokhale NH (2004) Elastic modulus imaging: on the uniqueness and nonuniqueness of the elastography inverse problem in two dimensions. Inverse Prob 20(1):283-296

Barbone PE, Oberai AA (2007) Elastic modulus imaging: some exact solutions of the compressible elastography inverse problem. Phys Med Biol 52(6):1577-1593

Bensamoun SF, Ringleb SI, Littrell L, Chen QS, Brennan M, Ehman RL, An KN (2006) Determination of thigh muscle stiffness using magnetic resonance elastography. J Magn Reson Im 23(2):242-247

Bishop J, Samani A, Sciarretta J, Plewes DB (2000) Two-dimensional MR elastography with linear inversion reconstruction and noise analysis. Phys Med Biol 45(8):2081-2091

Braun J, Buntkowsky G, Bernarding J, Tolxdorff T, Sack I (2001) Simulation and analysis of magnetic resonance elastography wave images using coupled harmonic oscillators and Gaussian local frequency estimation. Magn Reson Imaging 19(5):703-713

Carter FJ, Frank TG, Davies PJ, Mclean D, Cuschieri A (2001) Measurements and modeling of the compliance of human and porcine organs. Med Image Anal 5(4):231-236

Carter TJ, Sermesant M, Cash DM, Barratt DC, Tanner C, Hawkes DJ (2005) Application of soft tissue modeling to image guided surgery. Med Eng Phys 27(10):893-909

Castera L, Vergniol J, Foucher J, Le BB, Chanteloup E, Haaser M, Darriet M, Couzigou P, De LV (2005) Prospective comparison of transient elastography, Fibrotest, APRI, and liver biopsy for the assessment of fibrosis in chronic hepatitis C. Gastroenterology 128(2):343-350

Chen HP, Bicanic N (2000) Assessment of damage in continuum structures based on incomplete modal information. Comput Struct 74(5):559-570

Chen T, Wang XX, Chung S, Metaxas D, Axel L (2010) Automated 3D motion tracking using Gabor filter bank, robust point matching and deformable models. IEEE Trans Med Imag 29(1):1-11

Chenevert TL, Skovoroda AR, O'Donnell M, Emelianov SY (1998) Elasticity reconstructive imaging by means of stimulated echo MRI. Magn Reson Med 39(3):482-490

Chinzei K, Miller K (2001) MRI guided surgical robot. Proc ARAA:50-55

Chui CK, Kobayashi E, Chen X, Hisada T, Sakuma I (2004) Combined compression and elongation experiments and non-linear modeling of liver tissue for surgical simulation. Med Biol Eng Comput 42(6):787-798

Chui CK, Kobayashi E, Chen X, Hisada T, Sakuma I (2007) Transversely isotropic properties of porcine liver tissue: experiments and constitutive modeling. Med Bio Eng Comput 45(1):99-106

Cordero-Grande L, Vegas-Sanchez-Ferrero G, Casaseca-de-la-Higuera P, Alberola-Lopez C (2011) Improving harmonic phase imaging by the windowed fourier transform. IEEE Biomed Imag:520-523

Croisille P, Moore CC, Judd RM (1999) Differentiation of viable and nonviable myocardium by the use of three dimensional tagged MRI in 2-day-old re-perfused canine infarcts. Circulation 99:284-291

Davis CA, Li J, Denny TS (2006) Analysis of spectral changes and filter design in tagged cardiac MRI. Biomedical Imaging: Nano to Macro, 3rd IEEE International Symposium, April:137-140

Delalleau A, Josse G, Lagarde JM, Zahouani H, Bergheau JM (2006) Characterization of the mechanical properties of skin by inverse analysis combined with the indentation test. J Biomech 39(9):1603-1610

Deng X, Thomas SD (2005) Combined tag tracking and strain reconstruction from tagged cardiac MR images without user-defined myocardial contours. J Magn Reson Imaging 21(1):12-22

Denney JT, Prince JL (1994) Optimal brightness functions for optical flow estimation of deformable motion. IEEE Trans Image Proc 3(2):178-191

Denney TS, McVeigh ER (1997) Model-free reconstruction of three-dimensional myocardial strain from planar tagged MR images. J MAGN RESON IMAGING 7(5):799-810

Dey A, Mahadevan S (1998) Ductile structural system reliability analysis using adaptive importance sampling. Struct Safety 20(2):137-154

Ding K, Zhou Z, Liu C (1998) Latin hypercube sampling used in the calculation of the fracture probability. Reliab Eng Syst Safety 59(2):239-242

Dong XN, Guda T, Millwater HR, Wang XD (2009) Probabilistic failure analysis of bone using a finite element model of mineral-collagen composites. J Biomech 42(3):202-209

Douglas AS, Hunter WC, Wiseman MD (1990) Inhomogeneous deformation as a source of error in strain measurements derived from implanted markers in the canine left ventricle. J Biomech 23(4):331-341

Easley SK, Pal S, Tomaszewski PR, Petrella AJ, Rullkoetter PJ, Laz PJ (2007) Finite element-based probabilistic analysis tool for orthopaedic applications. Comput Meth Prog Bio 85(1):32-34

Edvardsen R, Gerber BL, Garot J, Bluemke DA, Lima JAC, Smiseth OA (2002) Quantitative assessment of intrinsic regional myocardial deformation by doppler strain rate echocardiography in humans. Circulation 106(1):50-56

Ennis DB, Epstein FH, Kellman P, Fananapazir L, Mcveigh ER, Arai AE (2003) Assessment of regional systolic and diastolic dysfunction in familial hypertrophic cardiomyopathy using MR tagging. Magn Reson Med 50(3):638-642

Erdemir A, Viveiros ML, Ulbrecht JS, Cavanagh PR (2006) An inverse finite-element model of heel-pad indentation. J Biomech 39(7):1279-1286

Fischer SE, McKinnon GC, Maier SE, Boesiger P (1993) Improved myocardial tagging contrast. Magn Reson Med 30(2):191-200

Fu YB, Chui CK, Teo CL, Kobayashi E (2011) Motion tracking and strain map computation for quasi-static Magnetic Resonance Elastography. MICCAI, LNCS 6891:433-440

Gao Z, Lister K, Desai JP (2010) Constitutive modeling of liver tissue: experiment and theory. Ann Biomed Eng 38(2):505-516

Gassert R, Moser R, Burdet E, Bleuler H (2006) MRI/fMRI-compatible robotic system with force feedback for interaction with human motion. IEEE/ASME Trans Mechatronics 11(2):216-224

Gennert MA, Negahdaripour S (1987) Relaxing the brightness constancy assumption in computing optical flow. MIT Technical Report AI Memo 975

Gent AN (2000) Engineering with Rubber. Hanser Gardner

Gotte MJW, Rossum AC, Twisk JWR (2001) Quantification of regional contractile function after infarction: strain analysis superior to wall thickening analysis in discriminating infarct from remote myocardium. J Am Coll Cardiol 37(3):808-817

Guo ZY, You SH, Wan XP and Bicanic N (2008) A FEM-based direct method for material reconstruction inverse problem in soft tissue elastography. Comput Struct 88(23):1459-68

Gupta SN, Prince JL (1995) On variable brightness optical flow for tagged MRI. Proc Inf Process Med Imag :323-334

Guttman MA, Prince JL, McVeigh ER (1994) Tag and contour detection in tagged MR images of the left ventricle. IEEE Trans. Med. Imaging 13(1):74–88

Haber I, Kikinis R, Westin CF (2001) Phase-driven finite element model for spatio-temporal tracking in tagged cardiac MRI. In Proc MICCAI:1332-1335

Hamhaber U, Grieshaber FA, Nagel JH, Klose U (2003) Comparison of quantitative shear wave MR elastography with mechanical compression tests. Magn Reson Med 49(1):71-77

Hamhaber U, Sack I, Papazoglou S, Rump J, Klatt D, Braun J (2007) Three-dimensional analysis of shear wave propagation observed by in vivo magnetic resonance elastography of the brain. Acta Biomaterialia 3(1):127-137

Hasofer AM, Lind NC (1974) Exact and invariant second-moment code format. ASCE J Eng Mech Division 100(1):111-121

Hawkes DJ, Ewards RJ, Barratt D, Blackall JM, Penney GR, Tanner C (2003) Measuring and modeling soft tissue deformation for image guided interventions. Lect Notes Comput Sci 2673:1-14

Helton JC, Davis FJ (2003) Latin hypercube sampling and the propagation of uncertainty in analyses of complex systems. Reliab Eng Syst Safety 81:23–69

Hildreth EC (1984) Measurement of Visual Motion. MIT Press, Cambridge

Horn BKP, Schunck BG (1981) Determining optical flow. Artificial Intelligence 17:185-203

Hu T, Desai JP (2004) Characterization of soft-tissue material properties: large deformation analysis. Lect Notes Comput Sci 3078:28-37

Huang BQ, Du XP (2008) Probabilistic uncertainty analysis by mean-value first order saddlepoint approximation. Reliab Eng Syst Safe 93:325-336

Kallel F, Bertrand M (1996) Tissue elasticity reconstruction using linear perturbation method. IEEE Tran Med Imaging 15(3):229-313

Kauer M, Vuskovic V, Dual J, Szekely G, Bajka M (2002) Inverse finite element characterization of soft tissues. Med Image Anal 6(3):275-287

Kerwin WS, Osman NF, Prince JL (2009) Image processing and analysis in tagged cardiac MRI. Handbook Med Image Proc Anal:435-452

Kerwin WS, Prince JL (1999) Tracking MR tag surfaces using a spatiotemporal filter and interpolator. Int J Imag Sys Tech 10(2):128-142

Kim J, Ahn B, De S, Srinivasan MA (2008) An efficient soft tissue characterization algorithm from in vivo indentation experiments for medical simulation. Int J Med Robotics Comput Assist Surg 4(3):277-285

Kruse S, Rose G, Glaser K, Manduca A, Felmlee J, Jack JC, Ehman R (2008) Magnetic resonance elastography of the brain. NeuroImage 39(1):231-237

Kuijer JP, Jansen E, Marcus JT, Rossum AC, Heethaar RM (2001) Improved harmonic phase myocardial strain maps. Magn Reson Med 46(5):993-999

Kumar S, Goldgof D (1993) Automatic tracking of SPAMM grid and the estimation of deformation parameters from cardiac MR images. IEEE Trans Med Imag 13(1):122-132

Kwon OI, Park C, Nam HS, Woo EJ, Seo JK, Glaser KJ, Manduca A, Ehman RL (2009) Shear modulus decomposition algorithm in magnetic resonance elastography. IEEE Tran Med Imaging 28(10):1526-1533

Laz PJ, Pal S, Halloran JP, Petrella AJ, Rullkoetter PJ (2006) Probabilistic finite element prediction of knee wear simulator mechanics. J Biomech 39(12):2303-2310

Laz PJ, Browne M (2009) A review of probabilistic analysis in orthopaedic biomechanics. J Eng Med 224

Liu KF, VanLandingham MR, Ovaert TC (2009) Mechanical characterization of soft viscoelastic gels via indentation and optimization-based inverse finite element analysis. J Mech Behav Biomed Mater 2(4):355-363

Liu W, Chen JJ, Ji SB, Allen SJ, Bayly PV, Wickline SA, Yu X (2004) Harmonic phase MR tagging for direct quantification of Lagrangian strain in rat hearts after myocardial infarction. Magn Reson Med 52(6):1282-1290

Liu Y, Kerdok AE, Howe RD (2004) A nonlinear finite element model of soft tissue indentation. Lect Notes Comput Sci 3078:67-76

Manduca A, Dutt V, Borup DT, Muthupillai R, Ehman RL, Greenleaf JF (1998) Reconstruction of elasticity and attenuation maps in shear wave imaging: An inverse approach. Proc. MICCAI, LNCS 1496:606-613

Manduca A, Lake DS, Kruse SA, Ehman RL (2003) Spatio-temporal directional filtering for improved inversion of MR elastography images. Med Image Anal 7(4):465-473

Manduca A, Muthupillai R, Rossman PG, Greenleaf JF, Ehman RL(1996) Image processing for magnetic resonance elastography. SPIE Med Imag 2710:231-239

Manduca A, Oliphant TE, Dresner MA, Mahowald JL, Kruse SA, Amromin E (2001) Magnetic resonance elastography: noninvasive mapping of tissue elasticity. Med Image Anal 5(4):237-254

Marinelli M, Positano V, Osman NF, Recchia FA, Lombardi M, Landini L (2008) Automatic filter design in HARP analysis of tagged magnetic resoance images. IEEE on Biomed Imag:1429-1432

Mazza E, Nava A, Bauer M, Winter R, Bajka M, Holzapfel GA (2006) Mechanical properties of the human uterine cervix: an in vivo study. Med Image Anal 10(2):125-136

Mazza E, Nava A, Hahnloser D, Jochum W, Bajka M (2007) The mechanical response of human liver and its relation to histology: an in vivo study. Med Image Anal 11(6):663-672

Mckay MD, Conover WJ, Beckman RJ (1979) A comparison of three methods for selecting values of input variables in the analysis of output from a computer code. Technometrics 21:239-245

McVeigh ER (1996) MRI of myocardial function: motion tracking techniques. Magn Res Imag 14(2):137-150

McVeigh ER (1998) Regional myocardial function. Cardiology Clinics 16(2):189–206

McVeigh ER, Ozturk C (2001) Imaging myocardial function. IEEE Sig Proc Mag 18(6):44-56

McVeigh ER, Prinzen FW,Wyman BT, Tsitlik JE,Halperin HR, HunterWC (1998) Imaging asynchronous mechanical activation of the paced heart with tagged MRI. Magn Res Med 39(4):507-513

Moarefzadeh MR, Melchers RE (1999) Directional importance sampling for ill-proportioned spaces. Struct Safety 21(1):1-22

Moore CC, O'Dell WG, McVeigh ER, Zerhouni EA (1992) Calculation of three-dimensional left ventricular strains from biplanar tagged MR images. J Magn Reson Imaging 2(2):165-175

Morse OC, Singer JR (1970) Blood velocity measurements intact subjects. Science 170(3956):440-441

Moulton M, Creswell L, Actis R, Myers K, Vannier M, Szabo B, Pasque M (1995) An inverse approach to determining myocardial material properties. J Biomech 28(8):935-948

Muthupillai R, Lomas DJ, Rossman PJ, Greenleaf JF, Manduca A, Ehman RL (1995) Magnetic Resonance Elastography by direct Visualization of Propagating Acoustic Strain Waves. Science 269(5232):1854-1857

Namani R, Simha N (2009) Inverse finite element analysis of indentation tests to determine hyperelastic parameters of soft-tissue layers. J Strain Analysis 44(5):347-361

Nava A, Mazza E, Furrer M, Villiger P, Reinhart WH (2008) In vivo mechanical characterization of human liver. Med Image Anal 12(2):203-216

Nava A, Mazza E, Kleinermann F, Avis NJ, McClure J (2003) Determination of the mechanical properties of soft human tissues through aspiration experiments. Lect Notes Comput Sci 2878:222-229

Oberai AA, Gokhale NH, Feijoo GR (2003) Solution of inverse problems in elasticity imaging using the adjoint method. Inverse Prob 19(2):297-313

Oliphant TE, Manduca A, Ehman RL, Greenleaf JF (2001) Complex-valued stiffness reconstruction for magnetic resonance elastography. Magn Reson Med 45(2):299-310

Ophir J, Cespedes I, Ponnekanti H, Yazdi Y, Li X (1991) Elastography: a quantitative method for imaging the elasticity of biological tissues. Ultrasonic Imaging 13(2):111-134

Osman NF, Kerwin WS, McVeigh ER, Prince JL (1999) Cardiac motion tracking using cine harmonic phase (harp) magnetic resonance imaging. Magn Reson Med 42(6):1048-1060

Osman NF, McVeigh ER, Prince JL (2000) Imaging heart motion using harmonic phase MRI. IEEE Trans Med Imag 19(3):186-202

Osman NF, Prince JL (2000) On the design of the bandpass filters in harmonic phase MRI. Image Processing, International Conference, 1:625-628

Osman NF, Prince JL (2000) Visualizing myocardial function using HARP MRI. Phys Med Biol 45(6):1665-1682

Othman SF, Xu H, Royston TJ, Magin RL (2005) Microscopic magnetic resonance elastography (microMRE). Magn Reson Med 54(3):605-15

Othman SF, Zhou XJ, Xu H, Royston TJ, Magin RL (2007) Error propagation model for microscopic magnetic resonance elastography shear-wave images. Magn Reson Imaging 25(1):94-100

Pan L, Prince JL, Lima JA, Osman NF (2005) Fast tracking of cardiac motion using 3D-HARP. IEEE Trans Biomed Eng 52(8):1425-1435

Papazoglou S, Hamhaber U, Braun J, Sack I (2008) Algebraic Helmholtz inversion in planar magnetic resonance elastography. Phys Med Biol 53(12):3147-3158

Park J, Metaxas D, Axel L (1996) Analysis of left ventricular wall motion based on volumetric deformable models and MRI SPAMM. Med Image Anal 1(1):53-71

Pathmanathan P, Gavaghan D, Whiteley J (2009) A comparison of numerical methods used for finite element modeling of soft tissue deformation. J Strain Analysis 44:391-406

Prince JL, McVeigh ER (1992) Motion estimation from tagged MR image sequences. IEEE Trans Med Imag 11(2):238-249

Qian Z, Huang X, Metaxas D, Axel L (2005) Robust segmentation of 4D cardiac MRI-tagged images via spatio-temporal propagation. In Proc SPIE Med Imag:580-591

Rajendra M, Yamamoto A, Oda T, Kataoka H, Yokota H, Himeno R, Higuchi T (2008) Motion generation in MR environment using electrostatic film motor for motion-triggered Cine-MRI. IEEE/ASME Tran Mechatronics 13(3):278-285

Reeder SB, McVeigh ER (1994) Tag contrast in breath-hold CINE cardiac MRI. Magn Reson Med 31(5): 521-525

Richards MS, Barbone PE, Oberai AA (2009) Quantitative three-dimensional elasticity imaging from quasi-static deformation: a phantom study. Phys Med Biol 54(3):757-779

Rosen J, Brown JD, De S, Sinanan M, Hannaford B (2008) Biomechanical properties of abdominal organs in vivo and postmortem under compression loads. J Biomech Eng 130(2):1-17

Ryf S, Tsao J, Schwitter J, Stuessi A, Boesiger P (2004) Peak-combination HARP: A method to correct for phase errors in HARP. J Magn Reson Imaging 20(5):874-880

Sack I, Beierbach B, Hamhaber U, Klatt D, Braun J (2009) Non-invasive measurement of brain viscoelasticity using magnetic resonance elastography. NMR Biomed 21(3):265-271

Sakuma I, Nishimura Y, Chui C, Kobayashi E, Inada H, Chen X, Hisada T (2003) In vitro measurement of mechanical properties of liver tissue under compression and elongation using a new test piece holding method with surgical glue. Lect Notes Comput Sci 2673:284-292

Samur E, Sedef M, Basdogan C, Avtan L, Duzgun O (2007) A robotic indenter for minimally invasive measurement and characterization of soft tissue response. Med Image Anal 11(4):361-373

Schnur DS, Zabaras N (1992) An inverse method for determining elastic material properties and a material interface. Int J Numer Methods Eng 33(10):2039-2057

Sette MM, Goethals P, D'hooge J, Brussel HV, Sloten JV (2011) Algorithm for ultrasound elastography: a survey. Comput Method Biomec 14(3):283-292

Sinkus R, Tanter M, Xydeas T, Catheline S, Bercoff J, Fink M (2005) Viscoelastic shear properties of in vivo breast lesions measured by MR elastography. Magn Reson Imaging 23(2):159-165

Skovoroda AR, Emelianov SY, O'Donnell M (1995) Tissue elasticity reconstruction based on ultrasonic displacement and strain images. IEEE T Ultrason Ferr 42(4):747-765

Skovoroda AR, Lubinski MA, Emelianov SY, O'Donnell M (1999) Reconstructive elasticity imaging for large deformations. IEEE T Ultrason Ferr 46(3):523-535

Srinivasan S, Krouskop T, Ophir J (2004) A quantitative comparison of modulus images obtained using nano indentation with strain elastograms. Ultra Med Biol 30(7):899-918

Suga M, Obata T, Hirano M, Tanaka T, Ikehira H (2007) Magnetic resonance elastography to observe deep areas: comparison of external vibration systems. Conf Proc IEEE Eng Med Biol Soc:2599-2602

Sumi C, Matsuzawa H (2007) Shear modulus reconstruction by ultrasonically measured strain ratio. J Med Ultra 34(4):171-188

Sumi C, Nakayama K (1998) A robust numerical solution to reconstruct a globally relative shear modulus distribution from strain measurements. IEEE T Med Imaging 17(3):419-428

Sumi C, Suzuki A, Nakayama K (1995) Estimation of shear modulus distribution in soft tissue from strain distribution. IEEE Tran Biomed Eng 42(2):193-202

Takei Y, Kobayashi E, Numano T, Washio T, Mizuhara K, Suga M (2010) Development of a pneumatic vibrator evaluation device for MR elastography. Proc Euro Congress Radiology

Tay BK, Kim J, Srinivasan MA (2006) In vivo mechanical behavior of intra-abdominal organs. IEEE T BioMed Eng 53(11):2129-2138

Venkatesh BA, Gupta H, Lloyd SG, Italia LD, Denney TS (2010) 3D left ventricular strain from unwrapped harmonic phase measurements. J Magn Reson Imag 31(4):854-862

Venkatesh SK, Yin M, Glockner JF, Takahashi N, Araoz PA, Talwalkar JA, Ehman RL (2008) MR elastography of liver tumors: preliminary results. Am J Roentgenol 190(6):1534–1540

Vizzutti F, Arena U, Marra F, Pinzani M (2009) Elastography for the non-invasive assessment of liver disease: limitations and future developments. GUT 58(8):157-160

Vogan J, Wingert A, Plante JS, Dubowsky S, Hafez M, Kacher D, Jolesz F (2004) Manipulation in MRI devices using electrostrictive polymer actuators: with an application to reconfiguration imaging coils. Proc ICRA:2499-2504

Vuskovic V (2001) Device for in vivo measurement of mechanical properties of internal human soft tissues. Dissertation ETH No. 41222

Wang H, Amini AA (2010) Accurate 2-D cardiac motion tracking using scattered data fitting incorporating phase information from MRI. In Proc SPIE Med Imag 7626:520-523

Weng J, Zhong J, Hu C (2009) Phase reconstruction of digital holography with the peak of the two-dimensional Gabor wavelet transform. Appl Opt 48(18):3308-16

Xie H, Kim K, Aglyamov SR, Emelianov SY, O'Donnell M, Weitzel WF, Wrobleski SK, Myers DD, Wakefield TW, Rubin JM (2005) Correspondence of ultrasound elasticity imaging to eirect mechanical measurement in aging DVT rats. Ultra Med Biol 31(10):1351-1359

Yin M, Talwalkar J, Glaser K, Manduca A, Grimm R, Rossman P, Fidler J, Ehman R (2007) Assessment of hepatic fabrosis with magnetic resonance elastography. Clin Gastroenterol Hepatol 5(10):1207-1213

Young AA, Kraitchman DL, Axel L (1994) Deformable models for tagged MR images: reconstruction of two and three dimensional heart wall motion. Proc IEEE workshop on Biomed Imag Anal 19:317-323

Zerhouni EA, Parish DM, Rogers WJ, Yang A, Shapiro EP (1988) Human heart: tagging with MR imaging- a method for noninvasive assessment of myocardial motion. Radiology 169(1):59-63

Zhang S, Douglas M, Yaroslavsky L, Summers R, Dilsizen V, Fananapazir L, Bacharach S (1996) A Fourier based algorithm for tracking spamm tags in gated magnetic resonance cardiac images. Med Phys 23(8):1359-1369

Zhao YG, Alfredo HS, Ang HM (2003) System reliability assessment by method of moments. ASCE J Struct Eng 129(10):1341-1349

Zhi H, Ou B, Luo BM, Feng X, Wen YL, Yang HY (2007) Comparison of ultrasound elastography, mammography, and sonography in the diagnosis of solid breast lesions. J Ultrasound Med 26(6):807-815

Zhong JG, Zeng HP (2007) Multiscale windowed fourier transform for phase extraction of fringe patterns. Appl Opt 46(14):2670-75

Zhu YN, Hall TJ, Jiang JF (2003) A finite-element approach for Young's modulus reconstruction. IEEE T Med Imaging 22(7):890-900

Ziol M, Handra-Luca A, Kettaneh A, Christidis C, Mal F, Kazemi F, Ledinghen V, Marcellin P, Dhumeaux D, Trinchet JC, Beaugrand M (2005) Noninvasive assessment of liver fibrosis by measurement of stiffness in patients with chronic hepatitis. C. Hepatology 41(1):48-54

LIST OF PUBLICATIONS

Journal papers:

Fu YB, Chui CK, Teo CL (2012) Accurate two-dimensional cardiac strain calculation using adaptive windowed Fourier transform and Gabor wavelet transform. Int J Comput Assist Radiol Surg, DOI: 10.1007/s11548-012-0689-2

Fu YB, Chui CK, Teo CL, Kobayashi E (2012) Elasticity imaging of biological soft tissue using a combined finite element and nonlinear optimization method. Inverse Probl Sci En, submitted

Fu YB Chui CK, Teo CL (2012) Liver tissue characterization from uniaxial stress-strain data using probabilistic inverse finite element method. J Mech Behav Biomed, submitted

Conference papers:

Fu YB, Chui CK, Teo CL, Kobayashi E (2011) Motion tracking and strain map computation for quasi-static magnetic resonance elastography. MICCAI, LNCS, 6891:433-440

Fu YB, Chui CK, Teo CL (2010) A combined finite element and nonlinear optimization method for soft tissue material reconstruction. 6th ACCAS: 91:93

Fu YB, Chui CK, Teo CL, Kobayashi E, Chang S (2010) A new actuation system with simulated electrocardiogram signal for MR elastography. ASME J of Medical Devices Conference, 3866